NUMERICAL SOLUTION OF RADIATIVE TRANSFER EQUATION IN 2D COMPLEX GEOMETRIES USING BODY-FITTED COORDINATES

BY

MD ERSHADUL HAQUE

A Thesis Presented to the
DEANSHIP OF GRADUATE STUDIES

KING FAHD UNIVERSITY OF PETROLEUM & MINERALS

DHAHRAN, SAUDI ARABIA

In Partial Fulfillment of the
Requirements for the Degree of

MASTER OF SCIENCE

In

MECHANICAL ENGINEEERING

DECEMBER 2021

KING FAHD UNIVERSITY OF PETROLEUM & MINERALS

DHAHRAN- 31261, SAUDI ARABIA

DEANSHIP OF GRADUATE STUDIES

This thesis, written by **Md Ershadul Haque** under the direction of his thesis advisor and approved by his thesis committee, has been presented and accepted by the Dean of Graduate Studies, in partial fulfillment of the requirements for the degree of **MASTER OF SCIENCE IN MECHANICAL ENGINEERING.**

Dr. Saad Bin Mansoor
(Advisor)

Dr. Khaled Saleh Al-Athel
Department Chairman

Dr. Bekir Sami Yilbas
(Member)

Dr. Suliman Saleh Al-Homidan
Dean of Graduate Studies

Dr. Rached Ben-Mansour
(Member)

Date

Dedicated to my parents, wife, and rest of my family

ACKNOWLEDGMENTS

Alhamdullilah, all praise be to Allah for all the accomplishments I have until now and what is yet to come. It is only because of Allah's mercy, I was able to make it this far. He is the true protector, and what an excellent helper he is to support his helpless creations! May peace and blessing prevail in this blessed land of two sanctuaries which was the sole reason to choose KFUPM as my destination. May Allah make my achievements in KFUPM fruitful for the awaiting career and accept my times here as one of the means of salvation hereafter.

After that, I would like to remember my family for their constant support, because of whom I feel a constant urge to finish my responsibilities here and have a happy reuniting with them. Apart from my parents, wife, and rest of my family, whose lovely faces make me homesick while he is thousands of miles away.

I would like to thank my advisor, Dr. Saad Bin Mansoor, for his continuous efforts and kind help. Professor Dr. Bekir Sami Yilbas's appreciation of good works and kind advice were a real inspiration indeed. Special thanks to Dr. Rached Ben-Mansour for his prompt responses and instantaneous supports all through the way. Thanks to honorable department chairman Khaled Saleh Al-Athel for his kind support. Last but not least, gratitude to the Bangladeshi and International community here in KFUPM for their company, being together as brothers in my time in KFUPM.

TABLE OF CONTENTS

LIST OF TABLES

LIST OF FIGURES

LIST OF SYMBOLS

$\mathbf{e}_1, \mathbf{e}_2, \mathbf{e}_3$	:	Basis vectors in the Cartesian coordinate system
$\mathbf{E}_1, \mathbf{E}_2, \mathbf{E}_3$	:	Covariant basis vectors in an orthogonal coordinate system
f		Distortion Function
g^{ij}	:	Contravariant components of the metric tensor
g_{ij}	:	Covariant components of the metric tensor
h_1, h_2, h_3	:	Scale Factors
I	:	Radiative Intensity (W/sr)
I_b	:	Blackbody Radiative Intensity (W/sr)
T_g	:	Enclosure Temperature (K)
$\boldsymbol{q}''$	:	Radiative Heat Flux (W/m^2)
$\boldsymbol{r}$	:	Position Vector (m)
t	:	Time (s)
x, y, z	:	Cartesian coordinates (m)
x^1, x^2, x^3	:	Orthogonal, curvilinear coordinates (m)
Greek Letter		
λ	:	Wavelength (m)
β_o	:	Extinction Coefficient (m^{-1})

ω	:	Scattering Albedo
σ	:	Stefan–Boltzmann Constant ($Wm^{-2}K^{-4}$)
k	:	Absorption Coefficient (m^{-1})
σ_s	:	Scattering Coefficient (m^{-1})
δ	:	Scattering Phase Function
φ	:	Polar Angle (rad)
ψ	:	Azimuthal Angle (rad)
Ω	:	Solid Angle (sr)

LIST OF ABBREVIATIONS

BFC	:	Body-Fitted Coordinates
CDM	:	Collapsed Dimension Method
CSM	:	Collocation Spectral Method
DFEM	:	Discontinuous Finite Element Method
DFIM	:	Decentralized Fuzzy Inference Method
DG	:	Discontinuous Galerkin
DOM	:	Discrete Ordinate Method
FDM	:	Finite Difference Method
FEM	:	Finite Element Method
FVM	:	Finite Volume Method
LBM	:	Lattice Boltzmann Method
MAPE	:	Mean Absolute Parentage Error
MCM	:	Monte Carlo Method
NEM	:	Natural Element Method
PDE	:	Partial Differential Equation
RMSE	:	Root Mean Square Error
RTE	:	Radiative Transfer Equation
SEM	:	Spectral Element Method

ABSTRACT

Full Name : Md Ershadul Haque

Thesis Title : Numerical Solution of Radiative Transfer Equation in 2D Complex Geometries Using Body-Fitted Coordinates

Major Field : Mechanical Engineering

Date of Degree : December 2021

Radiative heat transfer has broad applications in combustions (such as boilers, furnaces, engines, rocket nozzles, etc.), nuclear reactions (such as in the sun, in a fusion reactor, or nuclear bombs), laser-material interactions, target detection, solar energy collection, and high-temperature fabrications. This thesis focuses on solving radiative transfer equation (RTE) through absorption, emission, and isotropic scattering participating media for complex geometries using the body-fitted coordinates. A modified RTE for the orthogonal curvilinear coordinate system in 2D complex geometries is formed and then transformed into body-fitted coordinates (BFC) and solved applying the discrete ordinate method (DOM). The geometries' walls are considered gray, diffuse, and opaque, with the boundary conditions of both radiative and non-radiative equilibriums. First, the temperature field is determined by an iterative method, and then the radiative heat flux at the walls is calculated. This study also analyzes the grid independence for non-dimensional radiative heat flux using root-mean-square error and mean-absolute-percentage error methods. The validation of numerical results showed a notable agreement with published literature for various complex geometries with different participating media. The proposed model is applied to

investigate the effect of geometry skewness for both rigid body rotation and constant area. The scope of this study can be extended to solving RTE for transient-orthogonal, steady-state-nonorthogonal, and transient-nonorthogonal coordinate systems in future investigations.

ملخص الرسالة

الاسم الكامل: محمد إرشاد الحق

عنوان الرسالة: التحليل العددي لمعادلة الانتقال الاشعاعي في الهندسة المعقدة – ثنائية الأبعاد باستخدام إحداثيات الملائمة للجسم

التخصص: الهندسة الميكانيكية

تاريخ الدرجة العلمية : جمادى الأول ١٤٤٣

انتقال الحرارة الإشعاعي له تطبيقات واسعة في عمليات الاحتراق (مثل الغلايات والأفران والمحركات وفوهات الصواريخ وما إلى ذلك)، والتفاعلات النووية (مثل تفاعلات نووية في الشمس وتفاعلات النووية في مفاعلات الاندماج والقنابل النووية) وتفاعلات المواد بالليزر وتحديد الهدف وفي الطاقة الشمسية وصناعات التي تتطلب درجة حرارة عالية. تركز هذه الاطروحة في حل معادلة الانتقال الاشعاعي من خلال الامتصاص والانبعاث وتشتت الخواص الوسائط المشاركة للهندسيات المعقدة باستخدام إحداثيات مناسبة للجسم. يثم تشكيل معادلة الانتقال الاشعاعي المعدلة لنظام الإحداثيات المتعامدة المنحنية في الاشكال المعقدة ثنائية الابعاد ثم يتم تحويلها إلى إحداثيات المناسبة للجسم ويتم حلها باستخدام طريقة التنسيق المنفصلة. تعتبر جدران الاشكال الهندسية رمادية ومنتشرة ومعتمة مع الشروط الحدودية لكل من التوازن الإشعاعي وغير الإشعاعي. أولا يتم تحديد مجال درجة الحرارة باستخدام الطريقة التكرارية ثم يتم حساب التدفق الحراري عند الجدران. تحلل هذه الدراسة أيضًا استقلالية الشبكة للتدفق الحراري الإشعاعي غير البعدي باستخدام جذر متوسط الخطأ التربيعي وطرق متوسط. النسبة المئوية للخطأ المطلق. أظهر التحقق من صحة النتائج العددية اتفاقًا ملحوظًا مع الأدبيات المنشورة لمختلف الأشكال الهندسية المعقدة مع الوسائط المشاركة المختلفة. تم تطبيق النموذج المقترح لدراسة تأثير الانحراف الهندسي لكل من دوران الجسم الصلب والمساحة الثابتة. يمكن توسيع نطاق هذه الدراسة إلى حل معادلة الانتقال الاشعاعي لأنظمة إحداثيات عابرة متعامدة وثابتة وغير متعامدة وعابرة وغير متعامدة في التحقيقات المستقبلية.

CHAPTER 1

INTRODUCTION

Radiative heat transfer has a substantially higher temperature dependence than the other two moods of heat transfer (in general, the conduction and convection heat transfer are linearly dependent on the temperature difference, whereas the radiative heat transfer is proportional to the fourth power of the temperature difference). As a result, in high-temperature fields like nuclear reactions, combustion, and aircraft re-entry, radiative heat transfer may play a significantly greater role than conduction and convection. Furthermore, as modern science and technology strive for greater efficiency, the temperature of engineering applications will rise, making radiative heat transfer increasingly relevant. The design of these systems is highly reliant on accurate radiative heat transfer predictions.

1.1 Radiative transfer equation

The radiative transfer equation (RTE) is the central equation for the transmission of radiation in participating media, which defines the general equilibrium of the transport of radiative energy, taking into account the connections between decrease and increase of thermal energy because of absorption, emission, and scattering processes [1,2]. Solving the RTE is crucial for determining the radiative heat transfer in semi-transparent (solids, liquids, and gases), porous materials, and participating media, relevant in a wide range of science and engineering disciplines. Furthermore, the RTE is also important when it comes to determining the radiative heat transfer in rockets [3,4], target detection [5][6], combustion systems [7,8], astrophysics [9,10], optical tomography [11–14], micro-nano heat transfer [15,16], remote sensing [17,18], non-contact temperature field measurement [19], radiotherapy dose estimations [20,21], photo-bioreactors [22], neutron transport and nuclear physics [23], and solar energy harvesting [24–26], among others.

The classical RTE defines the radiative heat energy balance of constant refractive index allocation in the absorbing, emitting, and scattering media. In general, a light beam's radiative power in the medium is a function of spatial position $\boldsymbol{r}$, the direction of transfer $\boldsymbol{\Omega}$, the time t, and wavelength λ which is defined using the physical amount of radiative intensity $I_\lambda(\boldsymbol{r}, \boldsymbol{\Omega}, t)$. The frequency-dependent RTE is a radiative intensity equation that governs by $I_\lambda(\boldsymbol{r}, \boldsymbol{\Omega}, t)$. However, the present thesis conducts the frequency-independent RTE in participating media. The classical frequency-dependent RTE can be written as,

$$\frac{\partial I_\lambda(\boldsymbol{r},\boldsymbol{\Omega},t)}{c\partial t}+\frac{\partial I_\lambda(\boldsymbol{r},\boldsymbol{\Omega},t)}{\partial \boldsymbol{r}} = -\beta_{o,\lambda}I_\lambda(\boldsymbol{r},\boldsymbol{\Omega},t)+\ k_\lambda I_{\lambda b}(\boldsymbol{r},t)+\frac{\sigma_{s,\lambda}}{4\pi}\int I_\lambda(\boldsymbol{r},\boldsymbol{\Omega}_i,t)\delta_\lambda(\boldsymbol{\Omega}_i,\boldsymbol{\Omega})d\Omega_i \quad (1)$$

Where $\beta_{o,\lambda}$, k_λ, and $\sigma_{s,\lambda}$ are the extinction, absorption, and scattering coefficients in terms of wavelength, respectively. c is the light velocity $(3\times10^8\ ms^{-1})$. $I_{\lambda b}$ is the blackbody intensity in terms of wavelength and δ_λ represents the scattering phase function.

In thermal science, the efficient outcome of the RTE has become crucial to these scientific areas, leading to a comprehensive study on this subject. The RTE is a complicated integro-differential equation that allows for accurate solutions in simplified instances. As a result, approximate RTE solutions based on a numerical method are often utilized. Therefore, the RTE necessitates a numerical approach that is both robust and precise and one that can be used with a variety of computational methods.

The classical RTE is a first-order equation representing the transfer of radiative energy in media with a constant refractive index of the propagation of light beams along successive lines in the media. It is beneficial for engineering applications and has been widely utilized in science and engineering challenges for radiative transfer analysis. RTEs come in a variety of shapes and sizes. RTEs, for example, are often stated using multiple coordinate systems depending on the feasibility of handling certain issues. They are subjected to

various approaches in typical orthogonal coordinate systems, such as the Cartesian coordinate system and the cylindrical coordinate system.

Furthermore, to increase numerical solution stability, the classical form of RTEs, namely the formula of the first order, may be translated into 2nd order forms, such as the even-parity expression of the RTE and the 2nd order RTEs [27–29]. However, due to the physical features of a material or a possible temperature/pressure dependence, the refractive index of a medium may be a function of the spatial position. The earth's atmosphere (or other planets), hot air/flame gas, artificial materials, and ocean water, such as graded-index optical fibre, lenses, etc., are examples of participating media with gradient refractive index distribution. In such situations, it is appropriate to extend the classical RTE to take account of the impact of the curved ray direction, causing an RTE in the refractive media [30]. Several researchers have attracted the attention of radiative transfer in sorted index media, and some recent works include the literature [31–36].

1.2 Orthogonal Grid

The simulation of various processes is considered based on partial differential equations (PDE) with a numerical solution. The parameters of the problem (such as the geometry of the problem, the physical characteristics of the solution, the boundary conditions, etc.) also involve the use of very general coordinate systems, which can be obtained by a suitable modification of the Cartesian coordinates. The conversion of coordinates from the Cartesian system (x-y coordinate) to a curvilinear system (ξ–η coordinate) shows a crucial function in computational simulations manipulating grid-based schemes. This is due to the

geometric complexity of the domain's inefficient issues. Usually, the smooth and non-overlapping grid lines are generated by this method. The most beneficial reform could be to produce orthogonal grid lines both at and inside the boundaries, simplifying the discretization of the main formula and minimizing the discretization inaccuracy in resolving the main equation [37]. The orthogonal coordinate transformation, which is controlled by two Laplace formulas and subject to the boundary conditions of Cauchy-Riemann, can achieve this aim [38].

The orthogonal grid lines can also be obtained using a covariant Laplace equation method and the transformation governed by Laplace equations [39–43]. In recollection of Ryskin and Leal, his system is called the RL system [39]. The RL system is an adaptable approach for the numerical generation of orthogonal functions. With the ratio of variable scale factors around the domain, orthogonal grid lines can be formed in various grid spacings. The scale factor ratio is the distortion function (f) and focuses on determining it in most RL system studies. A particular case of the RL system is the Laplace equation method for orthogonal grid generation described above when the deformation function (f) is chosen as 1.

1.3 Definition of Relevant terms

Absorption coefficient (k): The absorption coefficient specifies how far light of a specific wavelength can reach a substance before being absorbed. Light is only weakly absorbed in a material with a low absorption coefficient, and if the material is thin enough, it will look transparent to that wavelength. The substance determines the absorption coefficient and the wavelength of light absorbed. Because light with energy below the band gap is insufficient to drive an electron from the valence band into the conduction band, semiconductor materials show a sharp edge in their absorption coefficient. As a result, this light does not absorb. The absorption coefficients of several semiconductor materials are listed in the table below.

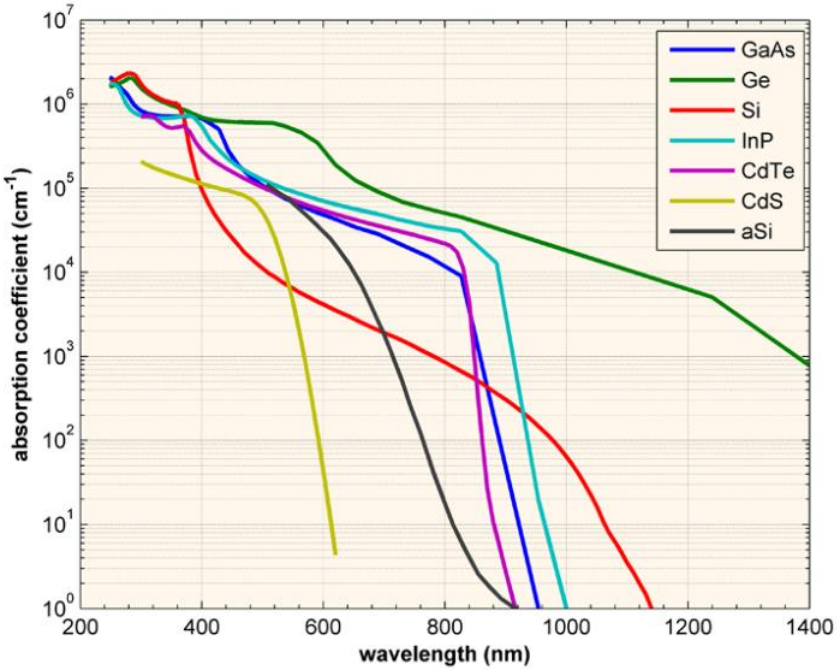

Fig. 1: Absorption coefficient of various semiconductor materials as a function of the vacuum wavelength of light at 300K [44].

Scattering Coefficient (σ_s)**:** The scattering coefficient (σ_s) is a measure of the capacity of particles to scatter photons from a light beam.

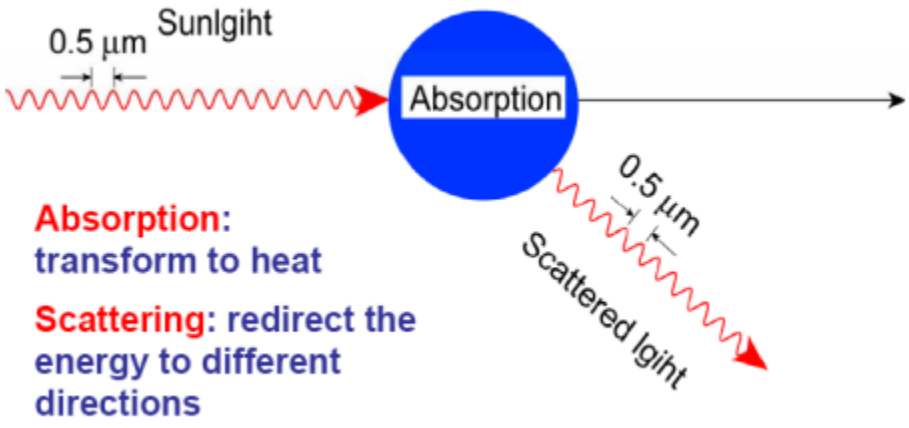

Fig. 2: Attenuation of atmospheric radiation by particulates [44].

Scattering albedo (ω)**:** scattering albedo (ω) can be defined as the ratio of scattering to extinction coefficient.

$$\omega = \frac{\sigma_s}{\beta_o} = \frac{\sigma_s}{k + \sigma_s}; 1 - \omega = \frac{k}{k + \sigma_s} = \frac{k}{\beta_o} \tag{2}$$

Scattering albedo can vary from zero to infinity. For $\omega \to 1$ when the medium is fully scattering alone (absent of absorbing medium), and for $\omega \to 0$, when the medium is purely absorbing.

Extinction coefficient (β_o)**:** The extinction coefficient (β_o) is the sum of scattering and absorption, representing the total effect of the medium on radiation passing the medium.

For example, an aerosol particle can scatter and absorb solar and infrared radiation, altering air temperature and the rates of photochemical reactions.

$$\beta_o = k + \sigma_s$$

The absorption coefficient (k) can be related to the extinction coefficient β_o by the following equation,

$$k = \frac{4\pi\beta_o}{\lambda} \tag{3}$$

Where, λ is the wavelength in nm.

Error Calculations: The present thesis measures two types of errors: root-mean-square error (RMSE) and Mean absolute percentage error (MAPR).

Root-mean-square error (RMSE): RMSE measure is one of the most preferred scale-dependent measures due to its suitabilities for evaluating various models built using the same datasets. RMSE is the square root of the mean of the square of all the errors. The square of the difference between actual and proposed numerical values is calculated. Then, the mean value is taken from all the instances. Finally, RMSE is calculated by taking the square root of the resulting mean value. The following equation can write the RMSE,

$$RMSE = \sqrt{\frac{1}{N}\sum_{i=1}^{N}(x_i - \hat{x}_i)^2} \tag{4}$$

Where N = the number of spatial nodes, $\hat{x}_i$ = the nondimensional radiative heat flux by the proposed model, x_i = the nondimensional radiative heat flux of original values.

Mean absolute percentage error (MAPR): MAPE is the most widely used measure to evaluate the numerical method and the exact solutions. The difference between the actual and the proposed numerical values is divided by the exact value. Then, MAPE is calculated by taking the mean value of all instances and taking percentages. The following equation can write the MAPE,

$$MAPE = \frac{1}{N}\sum_{i=1}^{N}\left|\frac{x_i - \hat{x}_i}{x_i}\right| \times 100\% \quad (5)$$

Where N = the number of spatial nodes, $\hat{x}_i$ = the nondimensional radiative heat flux by the proposed model, x_i = the nondimensional radiative heat flux of original value.

1.4 Supporting Objectives and Approach

The objective of the proposed work is to solve the RTE in complex geometries using body-fitted coordinates in an isotropic scattering medium. The present thesis applies the discrete ordinate method (DOM) to solve the RTE. MATLAB software is used for solving this problem. The main objective is to determine the heat flux vector at any point in the domain.

The specific objectives of the proposed thesis works are:

- To generate a 2D orthogonal grid for different complex geometries.
- To derive the RTE for the orthogonal, curvilinear coordinate system.

- To solve the RTE using the discrete ordinate method (DOM).
- To investigate the numerical results and validate them with other related studies.
- To analyze the grid independence test based on the root mean square and absolute errors.
- To examine the effect of geometry skewness for rigid body rotation and constant area.

1.5 Solution Procedure

The radiative transfer equation (RTE) is challenging to solve numerically because of its integro-differential nature. In the recent past, many scholars have devised various ways for solving the RTE for complex geometries. When solving the RTE, computing complexity and accuracy are the most important considerations. This research presents a newly formed RTE for the orthogonal curvilinear coordinate system in 2D complex geometries, translating the equation to body-fitted coordinate (BFC) and solving the problem using DOM. The geometries' walls are considered gray, diffuse, and opaque, with radiative and non-radiative equilibrium conditions. The temperature field is determined the radiative heat flux of the walls using an iterative process until convergence. The solution procedure is shown in the following flowchart (Fig. 3).

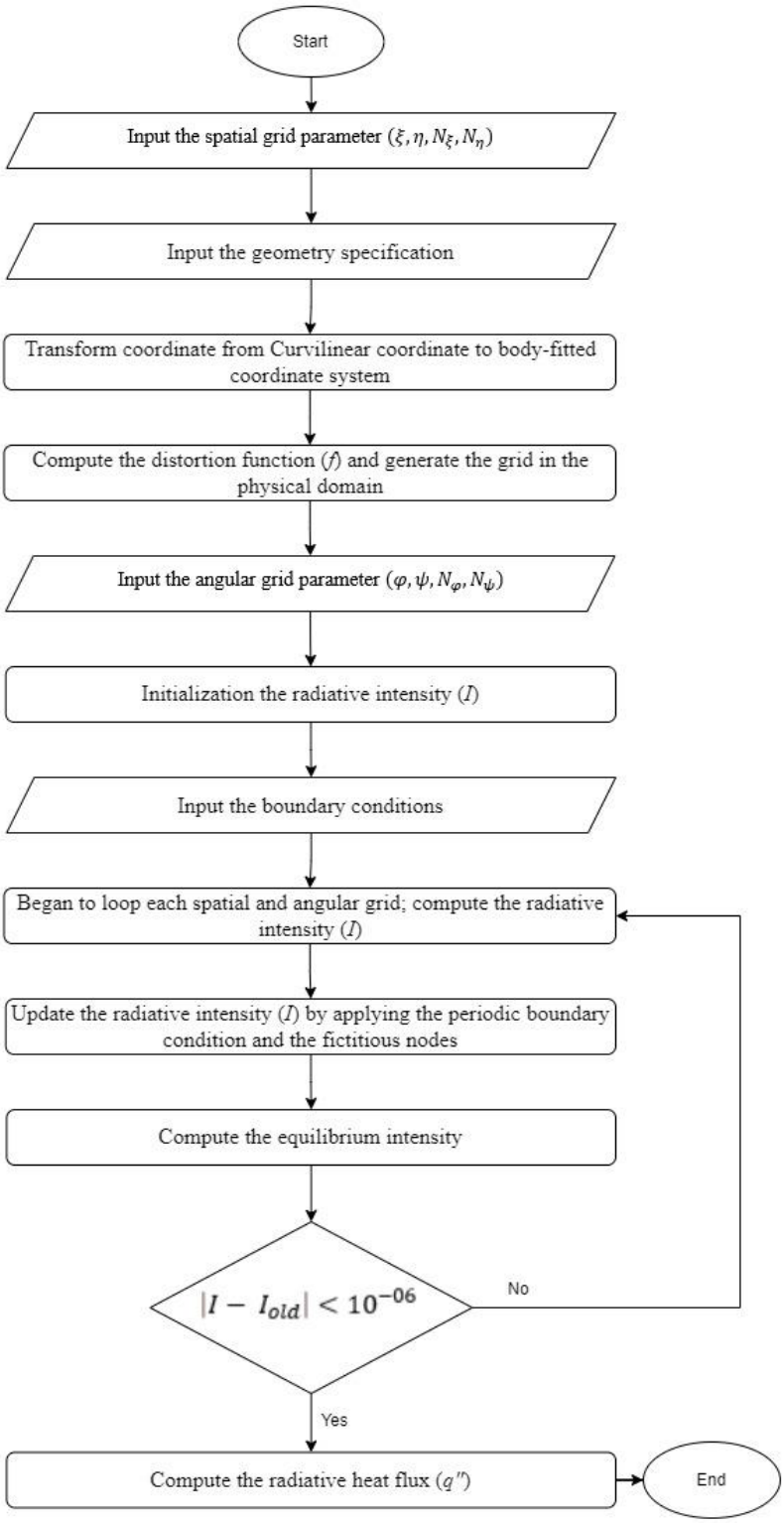

Fig. 3: Flowchart for solving the RTE and computing the radiative heat flux distribution.

1.6 Structure of the thesis

The thesis is structured as follows.

In Chapter 2, a brief overview of the literature of RTE solution techniques is provided. We try to find out the research gap of solving the RTE in a complex geometry in an absorbing, emitting, and scattering medium. Chapter 3 provides the detailed mathematical calculation for the RTE. Here, we derive an equation for radiative transfer for an orthogonal curvilinear coordinate system for 3D to the classical RTE. Chapter 4 proposes, derives, and demonstrates the numerical solution technique for solving the newly developed RTE solution. Here, we also discuss the boundary condition of radiative and non-radiative equilibriums for solving the RTE. In chapter 5, the results are discussed with converting the coordinate system of RTE, validation with the literature, grid independence, and the effect of geometry skewness.

Finally, the overall conclusions of the thesis can be found in Chapter 6.

CHAPTER 2

LITERATURE REVIEW

Computational modelling in real-world applications is necessary for analyzing radiative transfer because of the mathematical convolution of the RTE and the different irregular patterns of problems. At the same time, analytical solutions only exist in a few simple cases. However, numerical modelling of radiative transport in participating media takes a long time. Because of the intricacy and high dimensionality, which incorporates supplemental measurements of two angular sizes and three spatial dimensions, it necessitates considerable effort. Effective and accurate numerical techniques are therefore essential for most actual applications. Many efforts have been made to establish effective radiative transfer study techniques in the participating media.

Until now, several computational methods for the solution of the RTE have been developed. In general, the approaches can be split into two categories; the first approach is

founded on stochastic simulation, which consists of the different execution of Monte Carlo methods (MCM) [45–48], Distributions of Ratios of Energy Scattered Or Reflected (DESOR) method [49,50], and the second approach is the deterministic methods, such as discrete ordinate method (DOM) [51–58], PN approximation [59–62], finite element method (FEM) [63–67], finite difference method (FDM), discontinuous finite element method (DFEM) [68–70], finite volume method (FVM) [71–76], spectral element method [77], spectral method [78], radiation element method [79], the meshless method [80–82], ray-tracing method (RTM) [83,84], and the lattice Boltzmann method (LBM) [85–87] to name a few. Different numerical strategies were analyzed to solve the textbook's RTE [1].

All computational methods endure many numerical inaccuracies since they are approximate methods. The DOM, FVM, and FEM suffer space and angular discretization errors. It can give unphysical features to the solution, making it harder to interpret and completely ruining the answer. The basis and attributes of numerical errors must also be known, which may explain the effects of the numerical solution and layout techniques to mitigate or wipe out errors. The DOM approach has endured two kinds of computational errors for decades, i.e., ray effects and false scattering, and several techniques have been suggested to minimize these errors [88]. The FVM can be called a DOM with a special angular quadrature method, and the discrete ordinate formulas are centred on FEM and many other techniques. Therefore, false dispersion and ray effects are two general types of computational errors that must be known entirely. Hunter and Guo [89] have recently provided a detailed review of the numerical errors in the RTE solution. When applied to complex geometries, DOM remains the most economical process but suffers from a

deficiency recognized as the ray effect due to the angular discretization of radiative intensity.

Chai et al. [90] investigated numerically to solve the radiative transfer equation for five different irregular geometries with transparent media like absorbing, emitting, and anisotropically scattering using FVM. The results showed that the FVM could solve radiative heat transfer problems.

Parthasarathy et al. [91] used the MCM to solve the radiative transfer equation in three irregular two-dimensional geometries with absorbing, emitting, and anisotropic scattering media. They presented three separate scattering phase functions and five scattering albedos for these geometries from purely scattering ($\omega = 1.0$) to absorbing ($\omega = 0.0$) for these geometries.

Talukdar et al. [72] researched the RTE problem with the multi-blocking method in 3D curvilinear coordinates by applying the FVM. In non-orthogonal curvilinear coordinates, the system was introduced to deal with an irregular structure with a body-fitted organized grid. Several issues were solved to validate the consistency and applicability of the proposed multi-blocking. As they validated the present findings of the literature, their conclusions were considered promising.

Talukdar [92] used the collapsed dimension method (CDM) and a blocked-off region procedure to deal with radiative transfer problems in complex geometries. He validated various test problems in non-participating and participating media for radiative and non-radiative equilibrium conditions. The results were satisfactory for both straight-edged, curved, and inclined boundaries. The blocked-off region procedure based on Cartesian coordinates has proven useful for an RTM like the CDM.

In complex 2D and 3D geometries, Wang et al. [93] developed a meshless method and a discrete ordinates method to solve the radiative transfer equation. They used a moving least squares approximation meshless method to solve the second-order partial differential equations. Prediction results of radiative heat transfer problems obtained by the proposed method were compared to assess the meshless method's correctness.

Amiri et al. [94] investigated numerically using FVM and DOM to solve the RTE of different complex geometries in opaque, diffuse, and gray media. They solved the problem using both spatial and blocked-off discretize schemes. The results demonstrated that as the level of complexity of the enclosure (with skewed or curved walls) rose, more accurate grids were needed. They also analyzed the impact of the critical thermophysical parameters (asymmetry factor, extinction coefficient, scattering albedo, and conduction-radiation parameter) on the walls' maximum, conductive, and radiative heat flux.

The collocation spectral method (CSM) based on BFC in participating medium confined in 2D complex geometries investigated Sun and Li [95] to simulate radiative heat transfer problems. For this numerical approach, the RTE in orthogonal Cartesian coordinates should be transformed into the equation in body-fitted nonorthogonal curvilinear coordinates. The results show that a CSM based on BFC was a viable choice for solving radiative heat transfer problems in complex geometries.

The natural element method (NEM) was used by Zhang et al. [96] to solve radiative heat transfer problems in a 2D enclosure involving an absorbing, emitting, and isotropically scattering medium. They figured out how to solve the coupled heat transfer, transient conduction, and radiation problems in rectangular and complex geometries and the steady-state radiation and conduction problems in a gray cylindrical ring. NEM was effective, accurate, and stable and could solve radiative heat transfer problems in two-dimensional semitransparent media.

By finite volume method, Ramamoorthy et al. [97] studied numerically to solve the RTE and create a generalized mesh-based radiation solver (RAD-FVM) in various geometries for gray gas radiation. The results concluded that the improvement in resolution of the spatial and angular grid significantly increases the precision of the numerical results. Using other best-suited quadrature schemes to reflect the k-distribution with more quadrature points could further boost the accuracy of the results.

Petro [98] solved the problems of RTE in participating media by using the DOM and FEM. A grid formation (e.g., innovative expressions for axisymmetric enclosures, ordered and unstructured body-fitted meshes, local grid refinement, multi-block grids, fixed boundaries), the spatial discretization system, and the angular discretization system were developed by the author.

Aghanajafi and Abjadpour [99] applied DOM to solve the RTE in complex geometries meshed by structured and unstructured grids in a participating medium. They considered curvilinear, straight edges, and inclined boundaries of their geometries. The results revealed that using an unstructured grid to solve RTE is appropriate for all geometries with basic, inclined, and curved borders.

Kitzmann et al. [70] used a discontinuous Galerkin finite element method (DG-FEM) directly to solve the two-dimensional spherically symmetric radiative transfer equation. They demonstrated that the DG method could accurately describe radiative transfer in extended atmospheres and capture discontinuities or complex scattering behaviour that presented in the solution of specific radiative transfer tasks and, as a result, caused severe numerical problems for other radiative transfer solution methods.

McCulloch and Bindra [100] developed lattice Boltzmann methods based on algorithms and used them to fundamental the RTE, including radiation–material interactions, and

discovered that they were instrumental in modelling radiative energy exchange between radiation and material medium. LBM models utilized to address one and two-dimensional problems and the benefits of using this approach to handle multi-physics issues in a single framework.

Ma et al. [101] studied the radiative heat transfer problem in irregular porous fins using SEM and FEM. They examined SEM convergence characteristics for abnormal porous fin. They also determined the thermal output of the irregular porous fin, a volume balanced fin efficiency is made, taking into account the difference in material quantity.

Sarvari [102] employed a standard form of DOM to solve the RTE in plane-parallel semi-transparent material with changing refractive index using changeable discrete ordinate directions and the concept of refracted radiative intensity. Despite its simplicity, the results indicated that the variable DOM was accurate in solving the RTE in a semi-transparent medium with adjustable refractive index distribution.

Badri et al. [103] improved the general discretization technique to solve the RTE using vectorial finite elements. They used the manufactured solutions method to verify the discretization technique's accuracy in absorbing, scattering, and emitting substances. The vectorial finite element method was parallelized using domain decomposition to solve significant radiation problems on parallel computers.

Hong and Wu [104] investigated numerically to derive integral equations and solve the RTE in complex geometries using the meshless method in equilibrium in cubic, refractive, scattering media. They observed that the temperatures of cases with diffusely reflective semicircular surfaces were higher than those with black semicircular surfaces in the cubic medium with a more increased optical thickness and a higher temperature differential.

To solve the radiative transfer equation (RTE) in two-dimensional with in square and irregular media with inner obstacles, Wang and Liu [105] used a discontinuous Galerkin finite element method (DGFEM) using unstructured meshes. They applied an up-winding numerical flux across the inner boundaries to keep the computation domain stable, making the DGFEM appropriate and numerically stable for radiative transfer problems with substantial non-uniformity and discontinuities caused by ray effects.

Amiri and Lari [106] established a numerical technique of NEM and DOM to solve the RTE problems in complex geometries in non-gray gases (CO2/H2O/N2 mixtures). They used both spatial and angular discretize schemes to solve the RTE. The results showed that the comparisons of the CK model were very precise and, because of its much more excellent numerical performance, the CK approach was favoured over the LBL model for engineering calculations. Fan et al. [107] studied to solve the RTE in irregular enclosures, discretized by 3D unstructured grids, the Monte Carlo ray-tracing method (MCRTM) in gray semitransparent media.

In a 2D cylindrical geometry containing absorbing, emitting, and scattering medium, Zhou et al. [108] solved the radiative heat equation using a modified discrete ordinate form. In this study, the investigator broke down into two components of radiative power related to the wall and the medium.

Zhang et al. [109] investigated a high order positivity-preserving constraint for DG algorithms to solve RTE on triangular meshes. They theoretically established that the rotating positivity-preserving limitation on triangular grids could maintain both higher-order precision and positivity. The numerical result showed our schemes' higher-order accuracy and positivity-preserving schemes.

Clarke et al. [110] used the discontinuous Galerkin (DG) finite element method to solve the RTE for a plane-parallel issue, including scattering, absorption, and radiation. They used both space and angle directions discretization by the DG method. The DG formulation's suitability for problems with discontinuous solutions is demonstrated by solving a problem with a delta source term. The source term's in-element averaging eliminates negative intensity values for high-order elements.

Gaggioli et al. [111] developed a discrete ordinate approximation approach to treat the transient RTE. They applied the Fourier Continuation Discrete Ordinates (FC-DOM), a

spatially dispersionless and high-order spectral method for solving the RTE. The proposed method showed effectiveness and accuracy by comparing analytic and experimental results.

Sun et al. [112] solved the RTE in the complex enclosure using the DOM and DFIM in body-fitted coordinates in a participating gray medium. The results showed that the DFIM was robust in solving the radiative enclosure optimization design, and the numerical approach was more effective than other optimization techniques.

Djeumegni et al. [113] examined to solve the RTE in simple and complex geometries of spatial and angular discretize scheme of ray-tracing method (RTM) in a semi-transparent medium. They evaluated the fields of incident radiation and radiative flux. The findings were validated with good agreement for simple and complex geometries, and numerical simulations were performed for various large optical thickness ranges.

Djeumegni et al. [114] investigated the radiative heat transfer problem in a 2D with a centred inner square cavity in a semi-transparent gray medium. For many sizes of the inner square cavity, they discretized and computed explicit semi-analytical formulas based on Altaç and Bickley-Naylor functions. The results had been validated with good agreement for simple and complex geometries and numerical simulations for a wide range of optical thicknesses.

Wang et al. [115] investigated the discontinuous Galerkin (DG) finite element method (FEM) to solve the complex integro-differential RTE for concentric cylinders problems, including absorption, scattering, and emission media. They employed in both space and angles of discontinuous Galerkin hybrid methods. The results showed that DG formulation was in good agreement with accuracy when no absorption and scattering terms persisted such robust discontinuities solution.

Shao et al. [116] developed a cascading multigrid asymptotic-preserving discrete ordinate discontinuous streamline diffusion system for radiative transfer equations (RTE) with different scaling. The suggested numerical approach for solving the RTE, notably in diffusive and heterogeneous media, was effective and efficient.

Coelho [57] proposed decomposing radiation intensity into three components: a collimated, a backscattered collimated, and a diffuse component by a new formulation of radiative transfer problems in anisotropically scattering media. Without collimated irradiation, the new DOM formulation produced accurate results. Still, it did not perform well with collimated irradiation, especially for media with an optical thickness of the order of unity or below.

Doicu et al. [117] studied the empirical vector radiative transfer equation for a discrete random medium irradiated by a Gaussian beam using numerical techniques. They used the

Fourier transform approach for the horizontal variables, and for the 1D RTE, they used the discrete ordinate method with matrix exponential.

Feng and Wang [67] applied the discontinuous finite element method to solve transient pure and coupled radiative heat transport problems in two-dimensional participating media. The DFEM solutions of radiation-intensity time-dependent based values were extremely precise, and they were given as tabular numbers with four decimal digits.

Liu et al. [118] proposed a novel multiple-relaxation-time (MRT) lattice Boltzmann model for solving the frequency-independent radiative transfer equation in participating media. They applied 1D, 2D, and 3D RTE for steady-state and transient conditions. According to the findings, the MRT lattice Boltzmann model was accurate and reliable for handling transient and sustained radiative transfer issues in participating media.

Zhou et al. [119] investigated using the Chebyshev integration method to solve the radiative integral transfer equations (RITEs). The computing domain was partitioned into numerous subdomains in their suggested technique, and then the Chebyshev quadrature was applied to each subdomain. They also used the modified collocation spectral method (CSM) to compare the solution with the collocation spectral method. The hybrid Chebyshev integration approach for RITEs may achieve substantially greater accuracy

with acceptable processing time than the CSM or modified CSM for solving the RTE. It might be a useful option for thermal radiation calculations in simple geometries.

Jolivet et al. [120] studied to solve the steady-state monochromatic RTE for a full physics involving absorption, reflection, and scattering medium. They used a hybrid matrix-ready/matrix-free strategy to run the unknown issue through 27 thousand processes in under three minutes. On up to 27 thousand methods, deterministic findings for radiative transfer issues involving absorbing, reflecting, and scattering heterogeneities were provided on arbitrarily deconstructed unstructured grids.

As per the literature survey, many works have already been done to solve the various geometry of RTE. Because it's important, this research is still ongoing for improving the accuracy of the approximate solution for RTE. We have found some research gaps for solution techniques of RTE of complex geometries. In the present thesis, we are proposed a newly formed RTE for an orthogonal curvilinear coordinate system for the three-dimensional problem (in chapter 3). However, this thesis only considers the two-dimensional orthogonal curvilinear coordinate problem for solving various complex enclosures in participating media. We are solved this newly formed RTE by applying the discrete ordinate method, which we are discussed in chapter 4. And the results are validated by the present solution technique with previously published solutions in chapter 5. Furthermore, we are presented with some parametric studies in this thesis paper.

CHAPTER 3

MATHEMATICAL CALCULATIONS

This chapter conducts the mathematical calculations for the orthogonal grid generation and derives the radiative transfer equation (RTE) for Cartesian Coordinate and Orthogonal Curvilinear Coordinate systems. In simulations, a high-quality structured grid with smooth grid metrics is required, as grid shocks or discontinuities in grid metrics cause mesh-related flow distortions as well as additional sources of high wavenumber errors that contribute to aliasing error. Section 3.1 demonstrates the mathematical formula for orthogonal grid generation. This chapter proposes a newly formed RTE for an orthogonal curvilinear coordinate system in section 3.2.

3.1 Orthogonal grid generation

The orthogonal grid generation has a simpler form in the transformed plane than any non-orthogonal formulation. Because of the grid generation, there are fewer and quicker

calculations and fewer numerical errors. Furthermore, an orthogonal body-fitted grid makes prescribing boundary conditions simple and precise. This is one of the main reasons for using an orthogonal grid. In contrast, solving radiative transfer equation using finite difference formulation, one map non-uniformly spaced grid points in physical (x, z)-plane to equispaced points in the computational (ξ, η)-plane by relating the two via, $x = x(\xi, \eta)$ and $z = z(\xi, \eta)$. The grid generation scheme of Ryskin and Leal [39] is centred on the explicit remark that x and z are linear position functions in physical space as Cartesian coordinates system. Thus, $\nabla^2 x$ and $\nabla^2 z$ are constant-valued vector fields which imply,

$$\nabla^2 x = 0;\ \nabla^2 z = 0; \tag{6}$$

For the 2-D case in where ∇^2 is the Laplace covariant operator.

Let g_{ij} be the elements of a multidimensional coordinate system $\xi^1, \xi^2, \ldots\ldots, \xi^n$ a covariant metric tensor that describes an arc length (*ds*), therefore,

$$ds^2 = g_{ij} d\xi^i d\xi^j \tag{7}$$

The Laplacian $\nabla^2 x$ has the contravariant form, thus we can write,

$$\nabla^2 x = g^{ij} x_{,ij} = \left(g^{ij} x_{,i}\right)_{,j} = \left(g^{ij} \frac{\partial x}{\partial x^i}\right)_{,j}$$

$$= \frac{\partial}{\partial x^j}\left(g^{ij}\frac{\partial x}{\partial x^i}\right) + g^{im}\frac{\partial x}{\partial x^i}\left\langle {j \atop mj} \right\rangle$$

Where $\left\langle {i \atop ki} \right\rangle$ are the connection coefficients and are defined as $\boldsymbol{g} = g_{ij}\boldsymbol{E}^i\boldsymbol{E}^j = g^{ij}\boldsymbol{E}_i\boldsymbol{E}_j$ in terms of the elements of the metric tensor. Here, $\boldsymbol{E}^i$ and $\boldsymbol{E}_i$ are the contravariant and covariant basis vectors. Fig. 4 represents the orthogonal coordinate system in terms of basis vectors.

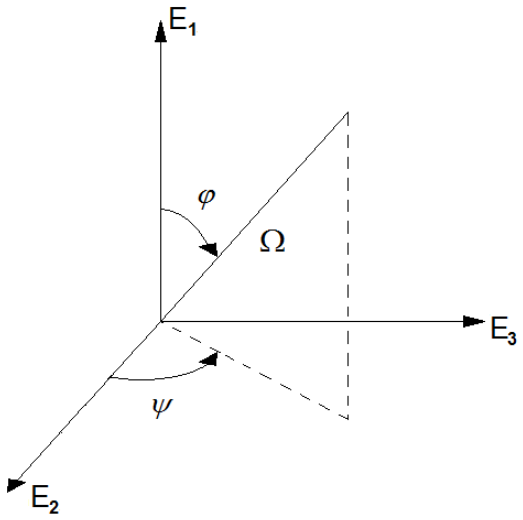

Fig. 4: A schematic view of the unit vector Ω at the point in the orthogonal coordinate system identified at the same point in terms of the base vectors.

For a general curvilinear coordinate system, we may describe all terms,

$$g_{ij} = \boldsymbol{E}_i.\boldsymbol{E}_j \quad g^{ij} = \boldsymbol{E}^i.\boldsymbol{E}^j \quad \left[g^{ij}\right] = \left[g_{ij}\right]^{-1} \tag{8}$$

And

$$\left\langle {k \atop ij} \right\rangle = \frac{g^{km}}{2}\left\{\frac{\partial g_{im}}{\partial x^j} + \frac{\partial g_{jm}}{\partial x^i} - \frac{\partial g_{ij}}{\partial x^k}\right\} \tag{9}$$

We have simplified expressions in an orthogonal, curvilinear coordinate scheme,

$$\left[g_{ij}\right] = \begin{bmatrix} h_1^2 & 0 & 0 \\ 0 & h_2^2 & 0 \\ 0 & 0 & h_3^2 \end{bmatrix}, \quad \left[g^{ij}\right] = \begin{bmatrix} 1/h_1^2 & 0 & 0 \\ 0 & 1/h_2^2 & 0 \\ 0 & 0 & 1/h_3^2 \end{bmatrix}, \qquad \left\langle {i \atop ki} \right\rangle = \frac{1}{2g}\frac{\partial g}{\partial x^k} \tag{10}$$

where g is the determinant of the metric tensor $\left[g_{ij}\right]$. Hence

$$\mathrm{g} = (h_1 h_2 h_3)^2 \tag{11}$$

And,

$$\left\langle {i \atop ki} \right\rangle = \frac{1}{2g}\frac{\partial g}{\partial x^k} = \frac{1}{2(h_1 h_2 h_3)^2}\frac{\partial}{\partial x^k}(h_1 h_2 h_3)^2 = \frac{1}{h_1}\frac{\partial h_1}{\partial x^k} + \frac{1}{h_2}\frac{\partial h_2}{\partial x^k} + \frac{1}{h_3}\frac{\partial h_3}{\partial x^k} \tag{12}$$

$\nabla^2 x$ can be written as,

$$\nabla^2 x = \frac{\partial}{\partial x^j}\left(g^{ij}\frac{\partial x}{\partial x^i}\right) + \frac{1}{\sqrt{g}}\frac{\partial \sqrt{g}}{\partial x^j} g^{ij}\frac{\partial x}{\partial x^i}$$

$$= \frac{1}{\sqrt{g}}\left[\sqrt{g}\,\frac{\partial}{\partial x^j}\left(g^{ij}\frac{\partial x}{\partial x^i}\right) + g^{ij}\frac{\partial x}{\partial x^i}\frac{\partial \sqrt{g}}{\partial x^j}\right]$$

$$= \frac{1}{\sqrt{g}}\frac{\partial}{\partial x^j}\left(\sqrt{g}\,g^{ij}\frac{\partial x}{\partial x^i}\right)$$

For an orthogonal coordinate system $g^{ij} = 0$ for $i \neq j$ and $g_{11} = h_1^2,\ g_{22} = h_2^2,\ g_{33} = h_3^2$

$$\nabla^2 x = \frac{1}{h_1 h_2 h_3}\left[\frac{\partial}{\partial x^1}\left(\frac{h_2 h_3}{h_1}\frac{\partial x}{\partial x^1}\right) + \frac{\partial}{\partial x^2}\left(\frac{h_1 h_3}{h_2}\frac{\partial x}{\partial x^2}\right) + \frac{\partial}{\partial x^3}\left(\frac{h_1 h_2}{h_3}\frac{\partial x}{\partial x^3}\right)\right]$$

For 2D, $x^1 \rightarrow \xi$, $x^3 \rightarrow \eta$ and $h_2 = 1$,

$$\nabla^2 x = \frac{1}{h_1 h_3}\left[\frac{\partial}{\partial \xi}\left(\frac{h_3}{h_1}\frac{\partial x}{\partial \xi}\right) + \frac{\partial}{\partial \eta}\left(\frac{h_1}{h_3}\frac{\partial x}{\partial \eta}\right)\right]$$

Thus,

$$\frac{\partial}{\partial \xi}\left(f\frac{\partial x}{\partial \xi}\right) + \frac{\partial}{\partial \eta}\left(\frac{1}{f}\frac{\partial x}{\partial \eta}\right) = 0 \qquad (13)$$

Similarly,

$$\frac{\partial}{\partial \xi}\left(f\frac{\partial z}{\partial \xi}\right) + \frac{\partial}{\partial \eta}\left(\frac{1}{f}\frac{\partial z}{\partial \eta}\right) = 0 \qquad (14)$$

Where, $f = \frac{h_3}{h_1}$.

f is the distortion function which is described as the ratio of scale factor in the ξ- direction to that in the η -direction, i.e.,

$$h_1 = h_\xi = \sqrt{g_{11}} = \sqrt{\boldsymbol{E}_\xi . \boldsymbol{E}_\xi} = \sqrt{\frac{\partial \boldsymbol{r}}{\partial \xi} . \frac{\partial \boldsymbol{r}}{\partial \xi}}$$

$$h_3 = h_\eta = \sqrt{g_{33}} = \sqrt{\boldsymbol{E}_\eta . \boldsymbol{E}_\eta} = \sqrt{\frac{\partial \boldsymbol{r}}{\partial \eta} . \frac{\partial \boldsymbol{r}}{\partial \eta}}$$

Where, position vector $\boldsymbol{r} = x\boldsymbol{e}_1 + z\boldsymbol{e}_3$, where $\boldsymbol{e}_1$ and $\boldsymbol{e}_3$ are the Cartesian bases vectors.

$$\frac{\partial \boldsymbol{r}}{\partial \xi} = \frac{\partial x}{\partial \xi}\, \boldsymbol{e}_1 + \frac{\partial z}{\partial \xi} \boldsymbol{e}_3$$

$$\frac{\partial \boldsymbol{r}}{\partial \eta} = \frac{\partial x}{\partial \eta}\, \boldsymbol{e}_1 + \frac{\partial z}{\partial \eta}\, \boldsymbol{e}_3$$

Therefore, the scale factors can be written as,

$$h_1 = \sqrt{\left(\frac{\partial x}{\partial \xi}\right)^2 + \left(\frac{\partial z}{\partial \xi}\right)^2} \tag{15}$$

$$h_3 = \sqrt{\left(\frac{\partial x}{\partial \eta}\right)^2 + \left(\frac{\partial z}{\partial \eta}\right)^2} \tag{16}$$

3.2 Radiative Transfer equation (RTE)

The radiative transfer problem described is quite complicated, and there are no general analytic solutions to the radiative transfer equation (RTE). The radiative transfer equation

(RTE) explains the transmission of radiative energy in participating media is introduced in this section. The basic concepts that affect the radiation intensity in a participating medium, such as emission, absorption, and in-scattering, are examined, and mathematical formulas characterize them. Several approximation solutions may be applicable depending on the application, and various numerical solutions to the RTE have been created. This thesis solves the newly formed RTE using the DOM numerical solution.

The present thesis is considered the radiative heat transfer in a complex geometry with perfectly opaque and diffuse surfaces. An absorbing, emitting, and scattering gray medium is contained within the enclosure. The frequency independence RTE for an absorbing, emitting, and scattering gray medium can be written as [121],

$$\frac{\partial I}{c\partial t} + \boldsymbol{\Omega}(\boldsymbol{\nabla} I) = -\beta_o I + kI_b + \frac{\sigma_s}{4\pi}\int I\delta d\Omega' \tag{17}$$

Where c is the speed of light. β_o, k, and σ_s are the extinction, absorption, and scattering coefficients, respectively. I and I_b are the radiative intensity and blackbody radiative intensity. δ for the scattering phase function, which denotes the possibility that a radiation beam moving in the direction Ω' will be scattered in that direction Ω.

The terms of the above equation on the right side indicate that the radiative intensity (I) decreases by both absorption and scattering in the first term $(\beta_o I)$. The second term (kI_b) represents an augment of the radiative intensity by emission. The last integral term on the equation indicates that the intensity increases due to the radiation scattered from the other directions. In this thesis, we are considered isotropic scattering $(\delta = 1)$ medium.

3.2.1 The Radiative Transfer Equation (RTE) for Cartesian Coordinate System

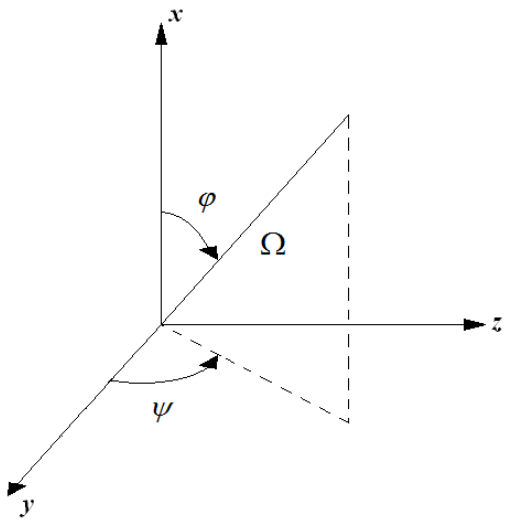

Fig. 5: A schematic view of a unit vector Ω at a point specified in the Cartesian coordinate system in terms of the basic vectors at all points being the same.

In Cartesian coordinates, lets x-axis is the polar axis and choosing a right-hand coordinate system, a unit vector in the direction (φ, ψ) for the solid angle ($\boldsymbol{\Omega}$) can be written as,

$$\boldsymbol{\Omega} = cos\varphi\ \boldsymbol{e_1} + sin\varphi cos\psi\ \boldsymbol{e_2} + sin\varphi sin\,\psi\ \boldsymbol{e_3} \tag{18}$$

$$\boldsymbol{\Omega} = \Omega^1\boldsymbol{e_1} + \Omega^2\boldsymbol{e_2} + \Omega^3\boldsymbol{e_3} \tag{19}$$

$$\boldsymbol{\Omega} = \Omega^i\boldsymbol{e_i} \tag{20}$$

Where $\boldsymbol{e_1}, \boldsymbol{e_2}, \boldsymbol{e_3}$ are the bases vectors for the cartesian coordinate system, which we usually use $\boldsymbol{i}, \boldsymbol{j}, \boldsymbol{k}$. As used in the tensor analysis, equation (20) uses the spectrum and summation convention. The RTE in the Cartesian coordinates can be written as,

$$\frac{\partial I}{c\partial t} + cos\varphi\ \frac{\partial I}{\partial x} + sin\varphi cos\psi\ \frac{\partial I}{\partial y} + sin\varphi sin\,\psi\ \frac{\partial I}{\partial z} = -\beta_o I + kI_b + \frac{\sigma_s}{4\pi}\iint I sin\varphi d\varphi d\psi \tag{21}$$

3.2.2 The Radiative Transfer Equation (RTE) for Curvilinear Coordinate System

The equation can be converted from the Cartesian coordinate (x, y, z)→ (y^1, y^2, y^3) to the orthogonal curvilinear coordinate (x^1, x^2, x^3). We will only write x^i and y^i for the orthogonal curvilinear and Cartesian coordinates using the range convention. The index *i* refers to the values 1, 2, and 3. Consider now, as defined by the following equations, an orthogonal curvilinear coordinate system,

$$y^1 = y^1(x^1, x^2, x^3), \quad y^2 = y^2(x^1, x^2, x^3), \quad y^3 = y^3(x^1, x^2, x^3), \tag{22}$$

The position vector $\boldsymbol{r}$ can be written as

$$\boldsymbol{r} = y^i \boldsymbol{e_i} \tag{23}$$

The covariant base vector ($\boldsymbol{E_i}$) and contravariant base vector ($\boldsymbol{E^j}$) can be defined the orthogonal coordinate system as

$$\boldsymbol{E_i} = \frac{\partial \boldsymbol{r}}{\partial x^i} \tag{24}$$

$$\boldsymbol{E_i}.\boldsymbol{E^j} = \delta_i^j \tag{25}$$

Where, δ_i^j is Kronecker delta, $\delta_i^j = 1$ when $i = j$ and $\delta_i^j = 0$ when $i \neq j$.

These base vectors have no unit magnitude in general. The size and orientation of the basis vectors vary from point to point. We can say that a set of unique basis vectors is identified at this point. In the orthogonal curvilinear coordinate system, a unit vector $\boldsymbol{\Omega}$ can again be described by choosing the $\boldsymbol{E_1}$ direction as the polar axis, as defined in Fig. 4 for the Cartesian system.

$$\boldsymbol{\Omega} = cos\varphi \frac{\boldsymbol{E_1}}{\sqrt{\boldsymbol{E_1}.\boldsymbol{E_1}}} + sin\varphi cos\psi \frac{\boldsymbol{E_2}}{\sqrt{\boldsymbol{E_2}.\boldsymbol{E_2}}} + sin\varphi sin\,\psi \frac{\boldsymbol{E_3}}{\sqrt{\boldsymbol{E_3}.\boldsymbol{E_3}}} \tag{26}$$

$$\boldsymbol{\Omega} = \frac{cos\varphi}{h_1}\boldsymbol{E_1} + \frac{sin\varphi cos\psi}{h_2}\boldsymbol{E_2} + \frac{sin\varphi sin\,\psi}{h_3}\boldsymbol{E_3} \tag{27}$$

$$\boldsymbol{\Omega} = \Omega^i \boldsymbol{E_i} \tag{28}$$

In equation (17), the term $\boldsymbol{\Omega}(\boldsymbol{\nabla} I)$ in an orthogonal curvilinear coordinate system can be described in tensor analysis using the covariant derivative,

$$\boldsymbol{\Omega}(\boldsymbol{\nabla} I) = \frac{\partial}{\partial x^i}\left(\Omega^i \boldsymbol{E_i} I\right)\boldsymbol{E}^j = \left(\Omega^i I\right)_{,i} \tag{29}$$

Equation (29) the subscript *"i"* indicates covariant differentiation with respect to the coordinate x^i. Using the covariant derivative definition, we can write

$$\boldsymbol{\Omega}(\boldsymbol{\nabla} I) = \frac{\partial}{\partial x^i}\left(\Omega^i I\right) + \left\langle {i \atop ki} \right\rangle (\Omega^k I) \tag{30}$$

Where $\left\langle {i \atop ki} \right\rangle$ are the connection coefficients and are defined as $\boldsymbol{g} = g_{ij}\boldsymbol{E}^i\boldsymbol{E}^j = g^{ij}\boldsymbol{E}_i\boldsymbol{E}_j$ in terms of the elements of the metric tensor. For a general curvilinear coordinate system, we may describe all terms,

$$g_{ij} = \boldsymbol{E}_i . \boldsymbol{E}_j \quad g^{ij} = \boldsymbol{E}^i . \boldsymbol{E}^j \quad \left[g^{ij}\right] = \left[g_{ij}\right]^{-1} \tag{31}$$

And

$$\left\langle {k \atop ij} \right\rangle = \frac{g^{km}}{2}\left\{\frac{\partial g_{im}}{\partial x^j} + \frac{\partial g_{jm}}{\partial x^i} - \frac{\partial g_{ij}}{\partial x^k}\right\} \tag{32}$$

We have simplified expressions in an orthogonal, curvilinear coordinate scheme,

$$\left[g_{ij}\right] = \begin{bmatrix} h_1^2 & 0 & 0 \\ 0 & h_2^2 & 0 \\ 0 & 0 & h_3^2 \end{bmatrix}, \quad \left[g^{ij}\right] = \begin{bmatrix} 1/h_1^2 & 0 & 0 \\ 0 & 1/h_2^2 & 0 \\ 0 & 0 & 1/h_3^2 \end{bmatrix}, \qquad \left\langle {i \atop ki} \right\rangle = \frac{1}{2g}\frac{\partial g}{\partial x^k} \tag{33}$$

where g is the determinant of the metric tensor $\left[g_{ij}\right]$. Hence

$$\mathrm{g} = (h_1 h_2 h_3)^2 \tag{34}$$

And,

$$\left\langle {i \atop ki} \right\rangle = \frac{1}{2g}\frac{\partial g}{\partial x^k} = \frac{1}{2(h_1 h_2 h_3)^2}\frac{\partial}{\partial x^k}(h_1 h_2 h_3)^2 = \frac{1}{h_1}\frac{\partial h_1}{\partial x^k} + \frac{1}{h_2}\frac{\partial h_2}{\partial x^k} + \frac{1}{h_3}\frac{\partial h_3}{\partial x^k} \tag{35}$$

Substituting equation (35) into equation (30) and rearranging, we obtain,

$$\begin{aligned}\boldsymbol{\nabla}.(\boldsymbol{\Omega}I) = \frac{1}{h_1h_2h_3}\Big[& cos\varphi\frac{\partial}{\partial x^1}(h_2h_3I) + sin\varphi cos\psi\frac{\partial}{\partial x^2}(h_1h_3I) \\ & + sin\varphi sin\,\psi\frac{\partial}{\partial x^3}(h_1h_2I)\Big] \\ & + \Big[\frac{1}{h_1}\frac{\partial\varphi}{\partial x^1}\frac{\partial}{\partial\varphi}(\,cos\varphi I) + \frac{1}{h_2}\frac{\partial\varphi}{\partial x^2}\frac{\partial}{\partial\varphi}(sin\varphi cos\psi I) \\ & + \frac{1}{h_3}\frac{\partial\varphi}{\partial x^3}\frac{\partial}{\partial\varphi}(sin\varphi sin\,\psi I)\Big] \\ & + \Big[\frac{1}{h_1}\frac{\partial\psi}{\partial x^1}\frac{\partial}{\partial\psi}(\,cos\varphi I) + \frac{1}{h_2}\frac{\partial\psi}{\partial x^2}\frac{\partial}{\partial\psi}(sin\varphi cos\psi I) \\ & + \frac{1}{h_3}\frac{\partial\psi}{\partial x^3}\frac{\partial}{\partial\psi}(sin\varphi sin\,\psi I)\Big]\end{aligned} \tag{36}$$

Calculating of the derivatives $\frac{\partial\varphi}{\partial x^i}$ and $\frac{\partial\psi}{\partial x^i}$,

The key problem is being able to derive representations for the derivatives $\frac{\partial\varphi}{\partial x^i}$ and $\frac{\partial\psi}{\partial x^i}$ while writing the RTE in an orthogonal curvilinear coordinate scheme. Below, these expressions were derived by Yilbas et al. [122],

$$\frac{\partial\varphi}{\partial x^1} = \frac{cos\psi}{h_2}\frac{\partial h_1}{\partial x^2} + \frac{sin\psi}{h_3}\frac{\partial h_1}{\partial x^3} \qquad \frac{\partial\psi}{\partial x^1} = cot\varphi\left[-\frac{sin\psi}{h_2}\frac{\partial h_1}{\partial x^2} + \frac{cos\psi}{h_3}\frac{\partial h_1}{\partial x^3}\right]$$

$$\frac{\partial\varphi}{\partial x^2} = -\frac{cos\psi}{h_1}\frac{\partial h_2}{\partial x^1} \qquad \frac{\partial\psi}{\partial x^2} = \frac{cot\varphi sin\psi}{h_1}\frac{\partial h_2}{\partial x^1} + \frac{1}{h_3}\frac{\partial h_2}{\partial x^3}$$

$$\frac{\partial\varphi}{\partial x^3} = -\frac{sin\psi}{h_1}\frac{\partial h_3}{\partial x^1} \qquad \frac{\partial\psi}{\partial x^3} = -\frac{cot\varphi cos\psi}{h_1}\frac{\partial h_3}{\partial x^1} - \frac{1}{h_2}\frac{\partial h_3}{\partial x^2}$$

The derivatives above are the general form of the $\frac{\partial \varphi}{\partial x^i}$ and $\frac{\partial \psi}{\partial x^i}$ derivatives. It should be noted that the equation form mentioned above corresponds to the concept of polar and azimuthal angles (φ, ψ), as shown in Fig. 4. Replacing equation (36) in equation (17), the RTE is obtained in any orthogonal curvilinear coordinate system below,

$$\frac{\partial I}{c\partial t} + \frac{cos\varphi}{h_1}\frac{\partial I}{\partial x^1} + \frac{sin\varphi cos\psi}{h_2}\frac{\partial I}{\partial x^2} + \frac{sin\varphi sin\psi}{h_3}\frac{\partial I}{\partial x^3} + \left[\frac{cos\varphi}{h_1}\left(\frac{cos\psi}{h_2}\frac{\partial h_1}{\partial x^2} + \frac{sin\psi}{h_3}\frac{\partial h_1}{\partial x^3}\right) - \frac{sin\varphi cos^2\psi}{h_1 h_2}\frac{\partial h_2}{\partial x^1} - \frac{sin\varphi sin^2\psi}{h_1 h_3}\frac{\partial h_3}{\partial x^1}\right]\frac{\partial I}{\partial \varphi} + \left[-\frac{cos\varphi cot\varphi sin\psi}{h_1 h_2}\frac{\partial h_1}{\partial x^2} + \frac{cos\varphi cot\varphi cos\psi}{h_1 h_3}\frac{\partial h_1}{\partial x^3} + \frac{cos\varphi cos\psi sin\psi}{h_1 h_2}\frac{\partial h_2}{\partial x^1} + \frac{sin\varphi cos\,\psi}{h_2 h_3}\frac{\partial h_2}{\partial x^3} - \frac{sin\varphi cos\psi sin\psi}{h_1 h_3}\frac{\partial h_3}{\partial x^1} - \frac{sin\varphi sin\psi}{h_2 h_3}\frac{\partial h_3}{\partial x^2}\right]\frac{\partial I}{\partial \psi} = -\beta_o I + kI_b + \frac{\sigma_s}{4\pi}\iint I sin\varphi d\varphi d\psi \quad (37)$$

Where, c is the speed of light, $k,\ \sigma_s\ and\ \beta_o = k + \sigma_s$ are the absorption, scattering, and extinction coefficient, respectively. Here, I_b is the black body intensity.

Equation (37) is the final equation for RTE, which we solve numerically using the discrete ordinate method. Chapter 4 discusses a detailed procedure to solve the RTE in different radiative mediums with boundary conditions.

Heat flux ($\boldsymbol{q}^{"}$):

The radiative heat flux can be written as,

$$\boldsymbol{q}^{"} = \int I\boldsymbol{\Omega} d\Omega \tag{38}$$

From equation (17), we have

$$\boldsymbol{\nabla}.(\boldsymbol{\Omega} I) = -\beta_o I + kI_b + \frac{\sigma_s}{4\pi}\int I\delta d\Omega'$$

$$\Rightarrow \boldsymbol{\nabla}.\int(\boldsymbol{\Omega} I)d\Omega = -\beta_o \int I\, d\Omega + k\int I_b\, \delta d\Omega + \frac{\sigma_s}{4\pi}\int \delta d\Omega' \int I\, d\Omega$$

$$\Rightarrow \boldsymbol{\nabla}.\boldsymbol{q}^{"} = -\beta_o \int I\, d\Omega + 4\pi k I_b\ + \sigma_s \int I\delta d\Omega'$$

$$\Rightarrow \boldsymbol{\nabla}.\boldsymbol{q}^{"} = -(k+\sigma_s)\int I\delta\, d\Omega' + 4\pi k I_b\ + \sigma_s \int I\delta d\Omega'$$

$$\Rightarrow \boldsymbol{\nabla}.\boldsymbol{q}^{"} = -k\int I\delta\, d\Omega' + 4\pi k I_b$$

$$\Rightarrow \boldsymbol{\nabla}.\boldsymbol{q}^{"} = k\left[4\pi I_b - \int I\delta\, d\Omega'\right] \tag{39}$$

Equation (39) represents the divergence of the radiative heat flux vector. We can apply this equation for radiative equilibrium or non-radiative equilibrium cases. If the medium is radiative equilibrium, the divergence of the radiative heat flux vector will be zero, i.e., ($\boldsymbol{\nabla}.\boldsymbol{q}^{"} = 0$). And if the medium generates heat energy, the medium will have non-radiative

equilibrium. In this case, the divergence of the radiative heat flux vector will not be zero, i.e., $(\boldsymbol{\nabla}.\boldsymbol{q}^{"} \neq 0)$.

The amount of heat energy moving through a surface is heat flux or thermal flux. The heat flux vector $(\boldsymbol{q}^{"})$ can be defined as

$$\boldsymbol{q}^{"} = q_x^{"}\boldsymbol{i} + q_y^{"}\boldsymbol{j} + q_z^{"}k \tag{40}$$

Where,

$$q_x^{"}(x,y,z) = \int_0^{2\pi}\int_0^{\pi} I cos\varphi sin\varphi d\varphi d\psi \tag{41}$$

$$q_y^{"}(x,y,z) = \int_0^{2\pi}\int_0^{\pi} I sin^2\varphi cos\psi d\varphi d\psi \tag{42}$$

And

$$q_z^{"}(x,y,z) = \int_0^{2\pi}\int_0^{\pi} I sin^2\varphi sin\psi d\varphi d\psi \tag{43}$$

Where φ and ψ are the polar and azimuthal angles, polar angle (φ) varies from 0 to π. On other hand azimuthal angle (ψ) varies 0 to 2π.

CHAPTER 4

NUMERICAL SOLUTION

The Radiative Transfer Equation (RTE) is an integro-differential equation that may be solved numerically iteratively using the finite-difference method (FDM). The RTE's convergent solution is found following the iterative phase. In this case, the algorithm proceeds to the next time step after the first step's convergent solution are achieved. The heat flow at each enclosure wall is calculated after confirming convergence for the last step. The numerical solution for orthogonal grid generation and RTE solution methodologies are discussed in this chapter.

4.1 Numerical Solution of Orthogonal Grid Generation

From equations (13) and (14), for the 2D orthogonal grid generation equation, we have

$$\frac{\partial}{\partial \xi}\left(f\frac{\partial x}{\partial \xi}\right)+\frac{\partial}{\partial \eta}\left(\frac{1}{f}\frac{\partial x}{\partial \eta}\right)=0$$

$$\frac{\partial}{\partial \xi}\left(f\frac{\partial z}{\partial \xi}\right)+\frac{\partial}{\partial \eta}\left(\frac{1}{f}\frac{\partial z}{\partial \eta}\right)=0$$

Finite difference methods discretize the above two PDEs. We obtain [123],

$$x_{i,j}=\left[\frac{f_{i+1/2,j}}{(\Delta\xi)^2}x_{i+1,j}+\frac{f_{i-1/2,j}}{(\Delta\xi)^2}x_{i-1,j}+\frac{1/f_{i,j+1/2}}{(\Delta\eta)^2}x_{i,j+1}+\frac{1/f_{i,j-1/2}}{(\Delta\eta)^2}x_{i,j-1}\right] / \left[\frac{f_{i+1/2,j}}{(\Delta\xi)^2}+\frac{f_{i-1/2,j}}{(\Delta\xi)^2}+\frac{1/f_{i,j+1/2}}{(\Delta\eta)^2}+\frac{1/f_{i,j-1/2}}{(\Delta\eta)^2}\right] \quad (44)$$

$$z_{i,j}=\left[\frac{f_{i+1/2,j}}{(\Delta\xi)^2}z_{i+1,j}+\frac{f_{i-1/2,j}}{(\Delta\xi)^2}z_{i-1,j}+\frac{1/f_{i,j+1/2}}{(\Delta\eta)^2}z_{i,j+1}+\frac{1/f_{i,j-1/2}}{(\Delta\eta)^2}z_{i,j-1}\right] / \left[\frac{f_{i+1/2,j}}{(\Delta\xi)^2}+\frac{f_{i-1/2,j}}{(\Delta\xi)^2}+\frac{1/f_{i,j+1/2}}{(\Delta\eta)^2}+\frac{1/f_{i,j-1/2}}{(\Delta\eta)^2}\right] \quad (45)$$

Here, $f_{i+\frac{1}{2},j}=\frac{f_{i+1,j}+f_{i,j}}{2}$, $f_{i-\frac{1}{2},j}=\frac{f_{i,j}+f_{i-1,j}}{2}$, $f_{i,j+\frac{1}{2}}=\frac{f_{i,j+1}+f_{i,j}}{2}$ and $f_{i,j-\frac{1}{2}}=\frac{f_{i,j}+f_{i,j-1}}{2}$

And indices (i,j) represents the direction ξ and η, respectively. The partial derivative x with respect to ξ is given by,

$$\frac{\partial x}{\partial \xi} = x_{i+1/2,j} - x_{i-1/2,j}$$

Similarly, $\frac{\partial x}{\partial \eta}$, $\frac{\partial z}{\partial \xi}$, and $\frac{\partial z}{\partial \eta}$ are expressed in the above equation (44) and equation (45). $f_{i,j}$is taken from the literature [124]. A typical grid point $(\boldsymbol{i,j})$ is shown in Fig. 6.

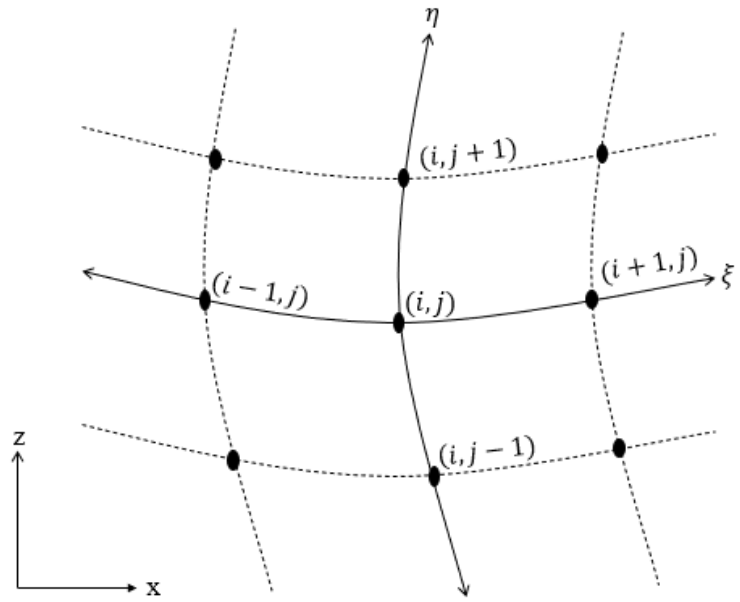

Fig. 6: A typical grid point $(\boldsymbol{i,j})$.

4.2 RTE in a numerically generated curvilinear coordinate system

To simplify the equation (37) with steady-state and two dimensions, we obtain,

$x^1 \to \xi$, $x^3 \to \eta$ and $h_2 = 1$;

$$\frac{cos\varphi}{h_1}\frac{\partial I}{\partial \xi}+\frac{sin\varphi sin\psi}{h_3}\frac{\partial I}{\partial \eta}+\left[\frac{cos\varphi sin\psi}{h_1 h_3}\frac{\partial h_1}{\partial \eta}-\frac{sin\varphi sin^2\psi}{h_1 h_3}\frac{\partial h_3}{\partial \xi}\right]\frac{\partial I}{\partial \varphi}+\left[\frac{cos\varphi cot\varphi cos\psi}{h_1 h_3}\frac{\partial h_1}{\partial \eta}-\frac{sin\varphi cos\psi sin\psi}{h_1 h_3}\frac{\partial h_3}{\partial \xi}\right]\frac{\partial I}{\partial \psi}=-\beta_o I+kI_b+\iint I sin\varphi d\varphi d\psi$$

$$\Rightarrow \frac{cos\varphi}{h_1}\frac{\partial I}{\partial \xi}+\frac{sin\varphi sin\psi}{h_3}\frac{\partial I}{\partial \eta}+\frac{sin\psi}{h_1 h_3}\left[cos\varphi\frac{\partial h_1}{\partial \eta}-sin\varphi sin\psi\frac{\partial h_3}{\partial \xi}\right]\frac{\partial I}{\partial \varphi}+\frac{cos\varphi sin\psi}{h_1 h_3}\left[\frac{1}{sin\varphi}\frac{\partial h_1}{\partial \eta}-sin\psi\frac{\partial h_3}{\partial \xi}\right]\frac{\partial I}{\partial \psi}=-\beta_o I+kI_b+\frac{\sigma_s}{4\pi}\iint I sin\varphi d\varphi d\psi \quad (46)$$

From the grid generation algorithm, the scale factors h_1 and h_3 at each point in the numerical domain are attained. The prior equation will be written as defined below, for convenience in further discussion,

$$C1\frac{\partial I}{\partial \xi}+C2\frac{\partial I}{\partial \eta}+C3\frac{\partial I}{\partial \varphi}+C4\frac{\partial I}{\partial \psi}=-\beta_o I+kI_b+\frac{\sigma_s}{4\pi}\iint I sin\varphi d\varphi d\psi \quad (47)$$

Where, $C1=\frac{cos\varphi}{h_1}$, $C2=\frac{sin\varphi sin\psi}{h_3}$, $C3=\frac{sin\psi}{h_1 h_3}\left[cos\varphi\frac{\partial h_1}{\partial \eta}-sin\varphi sin\psi\frac{\partial h_3}{\partial \xi}\right]$, $C4=\frac{cos\varphi sin\psi}{h_1 h_3}\left[\frac{1}{sin\varphi}\frac{\partial h_1}{\partial \eta}-sin\psi\frac{\partial h_3}{\partial \xi}\right]$

The C1, C2, C3, C4 symbols denote the functions of (ξ,η,φ,ψ). Let's discretized the above equations by using the finite difference method. The angles (φ,ψ) are discretized by just spitting their limit, which is divided into equal intervals. In the $0\le\varphi\le\pi$ range, the polar angle varies, and this interval is divided into 24 equal intervals. Therefore, there are 25 'nodes' for φ interval. In the $0\le\psi\le 2\pi$ range, the azimuthal angle varies, and this

interval is divided into 48 equal intervals. Thus, the interval for ψ is 49 'nodes'. In particular, 25×49=1225 distinct directions span the entire solid angle of 4π. By applying Simpson's rule, the double integral $\frac{1}{4\pi}\iint Isin\varphi d\varphi d\psi$ is calculated to each single integral.

Discretization of derivatives is simple, but aspects of stability need to be considered. It is well known that only if the coefficients in the discretized equation of all the newcomers (radiative intensities *I*) are positive can the finite difference discretisation result in a stable numerical scheme. In the equation, taking into account the first term discretization,

$$C1\frac{\partial I}{\partial \xi} = C1(i,j,m,n)\frac{I(i+1,j,m,n) - I(i,j,m,n)}{\Delta\xi} \tag{48}$$

Where (i,j,m,n) represent the indices for the variables of (ξ,η,φ,ψ) respectively. In Equation (47), the forward difference approximates the first-order derivative. This estimation, however, can only result in a constant discretization if the $C1(i,j,m,n)$ coefficient is negative. When it is positive, a backward difference must be used to measure the first-order derivative. This technique can very quickly be executed in numerical code. The coefficients C1, C2, and C3, C4 are essential to distinct. Now C1, C2 can be defined as,

$$C1 = \frac{cos\varphi}{h_1} \qquad C2 = \frac{sin\varphi sin\psi}{h_3}$$

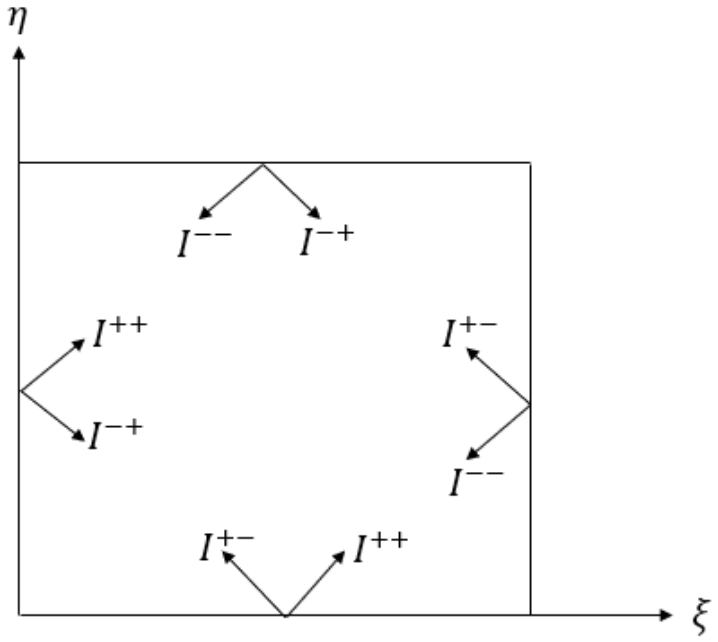

Fig. 7: A schematic view of the computational domain and *I* defines the radiative intensity at the boundaries.

The scale factors h_1 and h_3 are forever positive. Based on the polar (φ) and azimuthal (ψ) angles, the expressions C1 and C2 are negative or positive. It turns out that to attain constant discretization for all values of φ and ψ, The whole 4π solid angle can be partitioned into four quadrants. In the 1st quadrant, $0 < \varphi < \frac{\pi}{2}$, $0 < \psi < \pi$ and we will imply the radiative intensity as $I^{++}(i,j,m,n)$; in the 2nd quadrant, $\frac{\pi}{2} < \varphi < \pi$, $0 < \psi < \pi$ and we will imply the radiative intensity as $I^{-+}(i,j,m,n)$; in the 3rd quadrant, $0 < \varphi < \frac{\pi}{2}$, $\pi < \psi < 2\pi$ and we will imply the radiative intensity as $I^{+-}(i,j,m,n)$; finally, in the 4th

quadrant $\frac{\pi}{2} < \varphi < \pi$, $\pi < \psi < 2\pi$ and we will imply the radiative intensity as $I^{--}(i,j,m,n)$.

In the 1st quadrant, the backward difference formula for both $\frac{\partial I}{\partial \xi}$ and $\frac{\partial I}{\partial \eta}$ are to be used because both terms $cos\varphi$ and $sin\varphi sin\psi$ are positive. Only $cos\varphi$ is negative in the 2nd quadrant; therefore, a forward difference must be used for $\frac{\partial I}{\partial \xi}$. Since only $sin\varphi sin\psi$ is negative in the 3rd quadrant and thus a forward difference must be used for $\frac{\partial I}{\partial \eta}$. The forward difference formula for both derivatives $\frac{\partial I}{\partial \xi}$ and $\frac{\partial I}{\partial \eta}$ are to be used because, in the 4th quadrant, both $cos\varphi$ and $sin\varphi sin\psi$ are negative. To correct the boundary conditions, splitting the entire 4π solid angle into four quadrants is also essential. The summary of the numerical solution approach for the coefficient of C1 and C2 is shown in Table 1.

Table 1: Numerical solution approach for the coefficients of C1 and C2.

Quadrant	Polar angle (φ)	Azimuthal angle (ψ)	C1	C2	Radiative intensity	$\frac{\partial I}{\partial \xi}$	$\frac{\partial I}{\partial \eta}$
1st	$0 < \varphi < \frac{\pi}{2}$	$0 < \psi < \pi$	Positive	Positive	$I^{++}(i,j,m,n)$	Backward difference	Backward difference
2nd	$\frac{\pi}{2} < \varphi < \pi$	$0 < \psi < \pi$	Negative	Positive	$I^{-+}(i,j,m,n)$	Forward difference	Backward difference
3rd	$0 < \varphi < \frac{\pi}{2}$	$\pi < \psi < 2\pi$	Positive	Negative	$I^{+-}(i,j,m,n)$	Backward difference	Forward difference
4th	$\frac{\pi}{2} < \varphi < \pi$	$\pi < \psi < 2\pi$	Negative	Negative	$I^{--}(i,j,m,n)$	Forward difference	Forward difference

The third and fourth terms of C3 and C4 are viewed as brutal since these coefficients are very complicated, and predicting their sign, positive or negative, might not be straightforward. In this case, to use a backward difference method for the derivative $\frac{\partial I}{\partial \varphi}$ when C3 is positive and to use a forward difference formula when C3 is negative. For the derivative $\frac{\partial I}{\partial \psi}$ based on the sign of the coefficient C4, similar considerations apply. The final discretized equations are defined below for every single quadrant of the whole 4π solid angle,

First Quadrant: $0 < \varphi < \frac{\pi}{2}$, $0 < \psi < \pi$

$$
\begin{aligned}
I^{++}_{i,j,m,n}\left[\frac{C1_{i,j,m,n}}{\Delta\xi}+\frac{C2_{i,j,m,n}}{\Delta\eta}+\left|\frac{C3_{i,j,m,n}}{\Delta\varphi}\right|+\left|\frac{C4_{i,j,m,n}}{\Delta\psi}\right|+\beta_o\right] \\
= \left(\frac{C1_{i,j,m,n}}{\Delta\xi}\right) I^{++}_{i-1,j,m,n} + \left(\frac{C2_{i,j,m,n}}{\Delta\eta}\right) I^{++}_{i,j-1,m,n} \\
+ max\left[\left(\frac{C3_{i,j,m,n}}{\Delta\varphi}\right) I^{++}_{i,j,m-1,n}, -\left(\frac{C3_{i,j,m,n}}{\Delta\varphi}\right) I^{++}_{i,j,m+1,n}\right] \\
+ max\left[\left(\frac{C4_{i,j,m,n}}{\Delta\psi}\right) I^{++}_{i,j,m,n-1}, -\left(\frac{C4_{i,j,m,n}}{\Delta\psi}\right) I^{++}_{i,j,m,n+1}\right] + kI_b \\
+ \frac{\sigma_s}{4\pi} Integrate_{i,j,m,n}
\end{aligned}
\tag{49}
$$

Second Quadrant: $\frac{\pi}{2} < \varphi < \pi,\ 0 < \psi < \pi$

$$
\begin{aligned}
I^{-+}_{i,j,m,n}\left[-\frac{C1_{i,j,m,n}}{\Delta\xi}+\frac{C2_{i,j,m,n}}{\Delta\eta}+\left|\frac{C3_{i,j,m,n}}{\Delta\varphi}\right|+\left|\frac{C4_{i,j,m,n}}{\Delta\psi}\right|+\beta_o\right] \\
= -\left(\frac{C1_{i,j,m,n}}{\Delta\xi}\right)I^{-+}_{i-1,j,m,n}+\left(\frac{C2_{i,j,m,n}}{\Delta\eta}\right)I^{-+}_{i,j-1,m,n} \\
+ max\left[\left(\frac{C3_{i,j,m,n}}{\Delta\varphi}\right)I^{-+}_{i,j,m-1,n},-\left(\frac{C3_{i,j,m,n}}{\Delta\varphi}\right)I^{-+}_{i,j,m+1,n}\right] \\
+ max\left[\left(\frac{C4_{i,j,m,n}}{\Delta\psi}\right)I^{-+}_{i,j,m,n-1},-\left(\frac{C4_{i,j,m,n}}{\Delta\psi}\right)I^{-+}_{i,j,m,n+1}\right]+\ kI_b \\
+\frac{\sigma_s}{4\pi}Integrate_{i,j,m,n}
\end{aligned}
\tag{50}
$$

Third Quadrant: $0 < \varphi < \frac{\pi}{2},\ \pi < \psi < 2\pi$

$$
\begin{aligned}
I^{+-}_{i,j,m,n}\left[\frac{C1_{i,j,m,n}}{\Delta\xi}-\frac{C2_{i,j,m,n}}{\Delta\eta}+\left|\frac{C3_{i,j,m,n}}{\Delta\varphi}\right|+\left|\frac{C4_{i,j,m,n}}{\Delta\psi}\right|+\beta_o\right] \\
= \left(\frac{C1_{i,j,m,n}}{\Delta\xi}\right)I^{+-}_{i-1,j,m,n}-\left(\frac{C2_{i,j,m,n}}{\Delta\eta}\right)I^{+-}_{i,j-1,m,n} \\
+ max\left[\left(\frac{C3_{i,j,m,n}}{\Delta\varphi}\right)I^{+-}_{i,j,m-1,n},-\left(\frac{C3_{i,j,m,n}}{\Delta\varphi}\right)I^{+-}_{i,j,m+1,n}\right] \\
+ max\left[\left(\frac{C4_{i,j,m,n}}{\Delta\psi}\right)I^{+-}_{i,j,m,n-1},-\left(\frac{C4_{i,j,m,n}}{\Delta\psi}\right)I^{+-}_{i,j,m,n+1}\right]+\ kI_b \\
+\frac{\sigma_s}{4\pi}Integrate_{i,j,m,n}
\end{aligned}
\tag{51}
$$

Fourth Quadrant: $\frac{\pi}{2} < \varphi < \pi, \pi < \psi < 2\pi$

$$I^{--}_{i,j,m,n}\left[-\frac{C1_{i,j,m,n}}{\Delta\xi}-\frac{C2_{i,j,m,n}}{\Delta\eta}+\left|\frac{C3_{i,j,m,n}}{\Delta\varphi}\right|+\left|\frac{C4_{i,j,m,n}}{\Delta\psi}\right|+\beta_o\right]$$

$$= -\left(\frac{C1_{i,j,m,n}}{\Delta\xi}\right)I^{--}_{i-1,j,m,n}-\left(\frac{C2_{i,j,m,n}}{\Delta\eta}\right)I^{--}_{i,j-1,m,n}$$

$$+ max\left[\left(\frac{C3_{i,j,m,n}}{\Delta\varphi}\right)I^{--}_{i,j,m-1,n}, -\left(\frac{C3_{i,j,m,n}}{\Delta\varphi}\right)I^{--}_{i,j,m+1,n}\right] \quad (52)$$

$$+ max\left[\left(\frac{C4_{i,j,m,n}}{\Delta\psi}\right)I^{--}_{i,j,m,n-1}, -\left(\frac{C4_{i,j,m,n}}{\Delta\psi}\right)I^{--}_{i,j,m,n+1}\right] + kI_b$$

$$+ \frac{\sigma_s}{4\pi}Integrate_{i,j,m,n}$$

4.3 Boundary Condition

Radiative Equilibrium and Non-radiative Equilibrium:

The radiative intensity (*I*) is a function of temperature. To solve the RTE, the temperature field must be known. The cases of constant temperature and radiative equilibrium are considered in this study. From equation (39), we have,

$$\boldsymbol{\nabla}.\boldsymbol{q}^{"} = k\left[4\pi I_b - \int I\delta\, d\Omega'\right]$$

Where, $\boldsymbol{\nabla}.\boldsymbol{q}^{"}$ is the divergence of the radiative heat flux vector.

Case 1: Radiative equilibrium

For radiative equilibrium $\boldsymbol{\nabla}.\boldsymbol{q}^{"} = 0$,

Thus, blackbody radiative intensity can be written as

$$I_b = \frac{1}{4\pi}\iint I sin\varphi d\varphi d\psi \tag{53}$$

Case 2: Non-radiative equilibrium (heat generation)

For non-radiative equilibrium $\boldsymbol{\nabla}.\boldsymbol{q}^{"} \neq 0$,

Therefore, blackbody radiative intensity can be calculated by the following equation,

$$I_b = \frac{\sigma T_g^4}{\pi} \tag{54}$$

Where, T_g is the enclosure temperature which generates the heat inside the enclosure.

The boundary conditions associated with derivatives $\frac{\partial I}{\partial \varphi}$ and $\frac{\partial I}{\partial \psi}$ will first be examined. We may note that every one of the above four differential equations needs two boundary conditions for their solution. For instance, the two boundary conditions for the intensity $I_{i,j,m,n}^{++}$ for the first equation are given by the equilibrium intensities at the left and bottom boundaries at which the specific intensity $I_{i,j,m,n}^{++}$ is specified. The difference equation for $I_{i,j,m,n}^{++}$ is resolved from these boundary intensities until a modified intensity estimate is obtained for all the nodes denoted by $(\xi_i, \eta_j, \varphi_m, \psi_n)$. Identical considerations apply for the different radiative intensities in the other three quadrants.

The derivatives of $\frac{\partial I}{\partial \varphi}$ and $\frac{\partial I}{\partial \psi}$ only exist in a curvilinear coordinate system and disappear in a Cartesian coordinate system. The associated boundary conditions must therefore be carefully designed. For the derivative $\frac{\partial I}{\partial \psi}$ we may apply the periodic boundary condition. The azimuthal angles 0 and 2π show the same 'position'. This means that the radiative intensity of the azimuthal angle should be the same at these values. This criterion for stability offers the boundary condition for the derivative $\frac{\partial I}{\partial \psi}$.

CHAPTER 5

RESULTS AND CONCLUSIONS

5.1 Orthogonal Curvilinear Coordinate

The fundamental radiative transfer equation (RTE) is represented by equation (17). The two-dimensional complex geometry issues are the subject of the current investigation. This type of problem was numerically solved by many researchers using a variety of unique approaches. With an orthogonal coordinate system, we are deduced for three-dimensional RTE on equation (35) represented in every orthogonal coordinate system. Using this basic form of the equation, the RTE can be expressed in a variety of orthogonal coordinate systems, including Cartesian, Cylindrical, and Spherical coordinate systems, as well as in a variety of other orthogonal coordinate systems. Furthermore, when dealing with a complex domain, body-fitted coordinates allow us to solve the radiative intensity problem using the FDM, which is an alternative to the FEM, FVM, and other conventional techniques.

5.2 Grid Independence and Validation

Three studies are selected to thoroughly verify the numerical solution for solving the RTE using the discrete ordinate method (DOM). In this thesis, we are solved the RTE of a gray, absorbing/emitting (but not scattering) medium in a square enclosure; absorbing/emitting, and isotropically scattering homogeneous medium in a quadrilateral enclosure; and non-scattering homogeneous medium in a trapezoidal enclosure. These problems are solved using MATLAB R2019b-for educational use software. The computation is implemented with an Intel Core i5 processor on a personal computer. The maximum error of the radiative intensity $|I - I_{old}| < 10^{-06}$ is adopted as the convergence criterion for global iterations.

The shape type, quality, and quantity of grids must be considered while constructing an optimal grid. The number of grids impacts the total computing cost and the accuracy of simulation analysis findings. The use of coarse grids introduces a considerable spatial discretization error, lowering the accuracy of analytical results. Too many fine grids, on the other hand, can dramatically raise the round-off error beyond the truncation error, decreasing the accuracy of analysis findings [125]. As a result, choosing the correct number of grids is critical.

The grid independence is determined in this section using an error estimate of nondimensional radiative heat flux on the square, quadrilateral, and trapezoidal enclosure walls. It then validated the current work with published literature on absorbing, emitting, and isotropically scattering medium in a square, quadrilateral, and trapezoidal enclosures.

5.2.1 A gray, absorbing/emitting (but not scattering) medium

Firstly, we are considered a test case study of example 17.4 problem on Modest's radiative heat transfer book [1]. This problem involves a square enclosure of side lengths L with a gray, absorbing/emitting (but not scattering) medium presented in Fig. 8. Radiative equilibrium and constant absorption coefficient ($KL = 1$) are considered to solve this problem. The bottom wall is isothermal at the temperature T_w (with constant blackbody intensity T_{bw}), while the other walls are considered at zero temperature, and all four surfaces are black. The corner codes of the square geometry of the Cartesian system are (0,0), (1,0), (1,1), and (0,1) (all dimensions are in meter). Then we convert the physical domain to the computational domain, with the characteristic length of 1m.

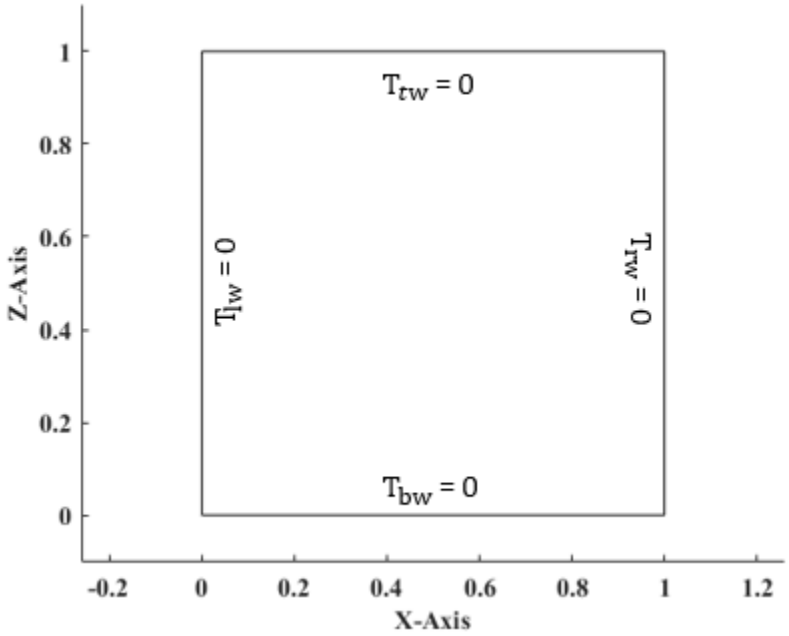

Fig. 8: Physical problem for a gray, absorbing/emitting (but not scattering) medium for a square enclosure.

Grid independence:

Fig. 9 shows the grid independence of square enclosure of constant spatial nodes with varying angular nodes. Fig. 9 (a), (b), and (c) illustrate the non-dimensional heat flux along the bottom wall of the modified square enclosure for (a) $N_\xi \times N_\eta = 20 \times 20$, (b) $N_\xi \times N_\eta = 24 \times 24$, and (c) $N_\xi \times N_\eta = 28 \times 28$ spatial grids. The results show that the numerical solutions change small deviations with changing the angular grids. Table 2 shows the error calculations for constant spatial nodes with varying angular nodes of square enclosure. These errors are calculated based on the exact solutions. The maximum root-mean-square error (RMSE) is 0.0034 for spatial grids of $N_\xi \times N_\eta = 20 \times 20$ and angular grids of $N_\varphi \times N_\psi = 24 \times 28$. On the other hand, the maximum mean-absolute-percentage error (MAPE) is 1.91% for both spatial grids of $N_\xi \times N_\eta = 20 \times 20$ and $N_\xi \times N_\eta = 24 \times 24$ with angular grids of $N_\varphi \times N_\psi = 24 \times 28$. In contrast, the minimum EMSE and MAPE are 0.0016 and 0.93% for spatial grids of $N_\xi \times N_\eta = 28 \times 28$ with angular grids of $N_\varphi \times N_\psi = 48 \times 96$. For the numerical complexities and the sizes, the present results do not much deviate from the exact solutions. We may choose fewer spatial and angular grids for numerical solutions to avoid the computational complexities and sizes.

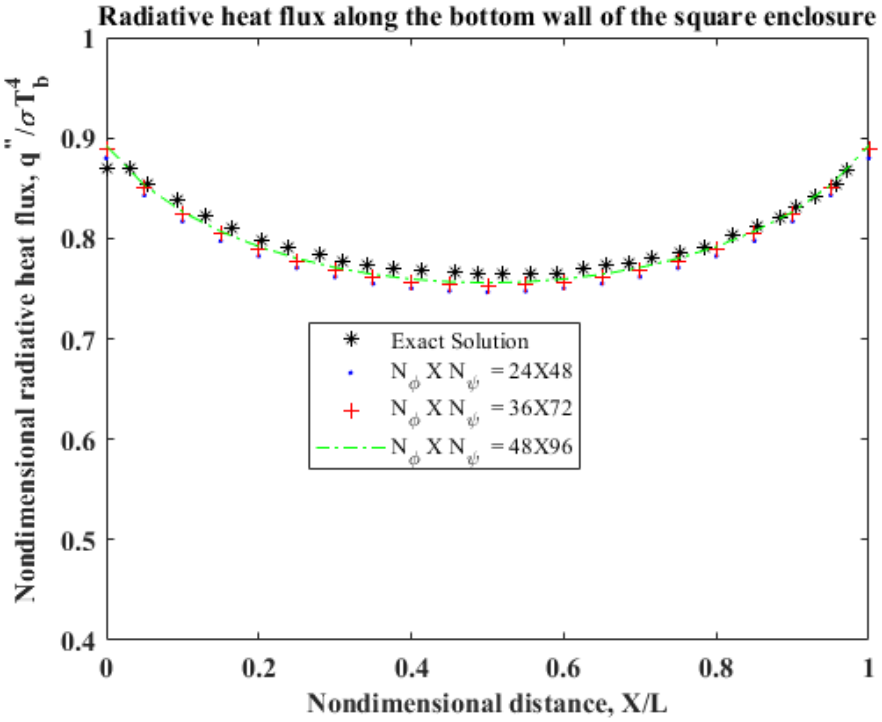
Radiative heat flux along the bottom wall of the square enclosure
Nondimensional radiative heat flux, q"/σT_b^4
Nondimensional distance, X/L
Exact Solution
N_φ X N_ψ = 24X48
N_φ X N_ψ = 36X72
N_φ X N_ψ = 48X96
1
0.9
0.8
0.7
0.6
0.5
0.4
0
0.2
0.4
0.6
0.8
1

(a)

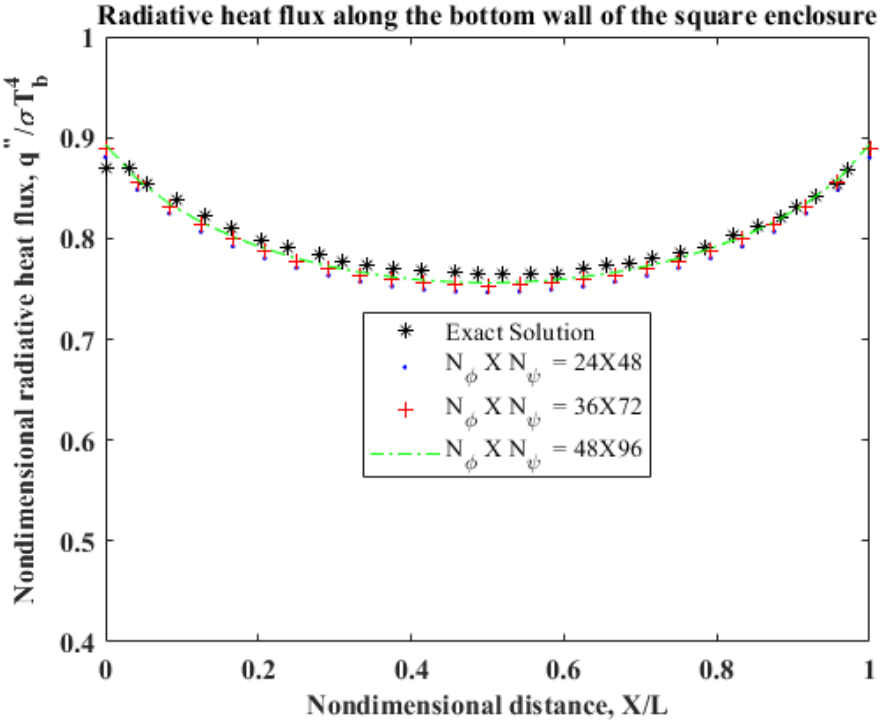
Radiative heat flux along the bottom wall of the square enclosure
Nondimensional radiative heat flux, q"/σT_b^4
Nondimensional distance, X/L
Exact Solution
N_φ X N_ψ = 24X48
N_φ X N_ψ = 36X72
N_φ X N_ψ = 48X96
1
0.9
0.8
0.7
0.6
0.5
0.4
0
0.2
0.4
0.6
0.8
1

(b)

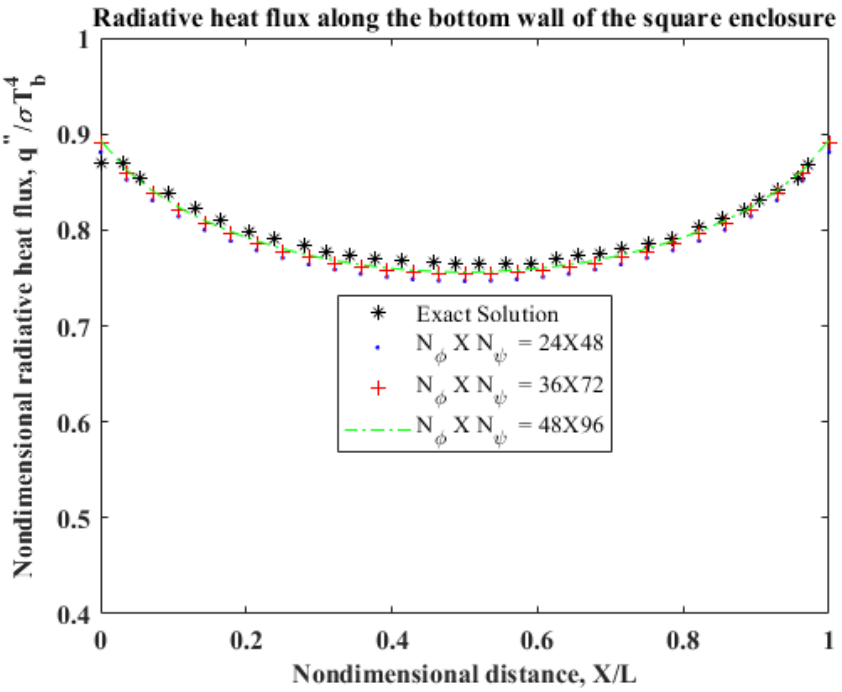

(c)

Fig. 9: Grid independence test of modified square enclosure for constant spatial grids, (a) $N_\xi \times N_\eta = 20 \times 20$, (b) $N_\xi \times N_\eta = 24 \times 24$, and (c) $N_\xi \times N_\eta = 28 \times 28$ with varying discrete angular grids.

Fig. 10 also shows the grid independence of square enclosure of constant angular nodes with varying spatial nodes. Fig. 10 (a), (b), and (c) illustrate the non-dimensional heat flux along the bottom wall of the square enclosure for (a) $N_\varphi \times N_\psi = 24 \times 48$, (b) $N_\varphi \times N_\psi = 36 \times 72$, and (c) $N_\varphi \times N_\psi = 48 \times 96$ angular grids. The figure shows that the results are almost constant for constant angular grids with varying spatial grids. Table 3 illustrates the error calculations for constant angular nodes with varying spatial nodes of modified square enclosure. For constant angular nodes, the results are deviated to the RMSE of only 0.0005 for increasing almost $N_\xi \times N_\eta = 20 \times 20$ spatial grids. However, the best solution is

obtained from the present numerical model for the angular nodes of $N_{\varphi} \times N_{\psi} = 48 \times 96$ with the spatial grids of $N_{\xi} \times N_{\eta} = 28 \times 28$.

Table 2: Grid independence test based on error calculations for constant spatial nodes with varying angular nodes of square enclosure.

Spatial nodes ($N_{\xi} \times N_{\eta}$)	Angular nodes ($N_{\varphi} \times N_{\psi}$)	Root-mean-square error	Mean absolute percentage error, %
20×20	24×48	0.0034	1.91
	36×72	0.0023	1.25
	48×96	0.0021	1.01
24×24	24×48	0.0031	1.91
	36×72	0.0021	1.23
	48×96	0.0018	0.97
28×28	24×48	0.0029	1.90
	36×72	0.0019	1.20
	48×96	0.0016	0.93

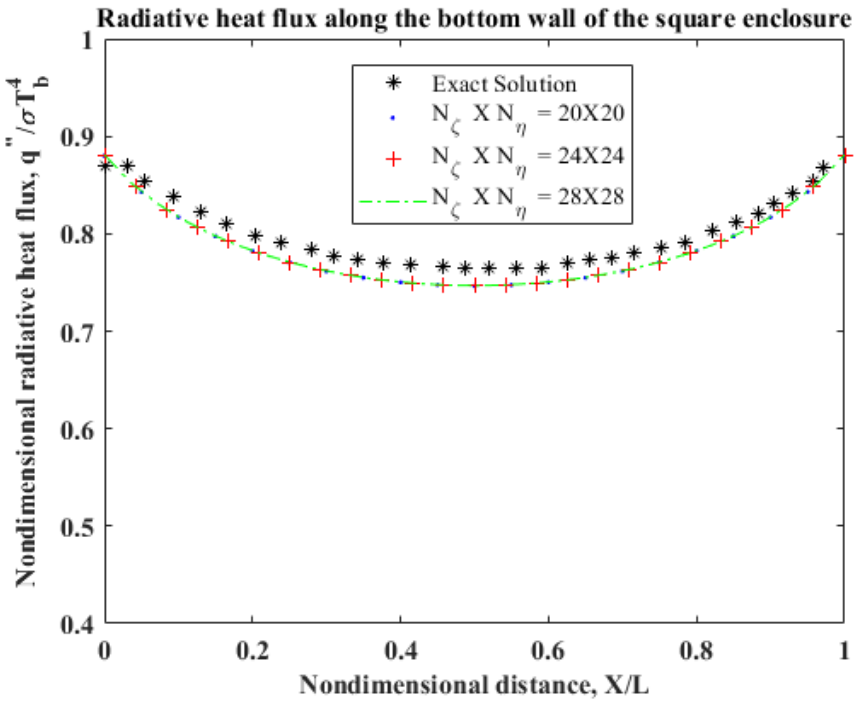
Radiative heat flux along the bottom wall of the square enclosure
Exact Solution
N_ζ X N_η = 20X20
N_ζ X N_η = 24X24
N_ζ X N_η = 28X28
Nondimensional radiative heat flux, q"/σT_b^4
Nondimensional distance, X/L
1
0.9
0.8
0.7
0.6
0.5
0.4
0
0.2
0.4
0.6
0.8
1

(a)

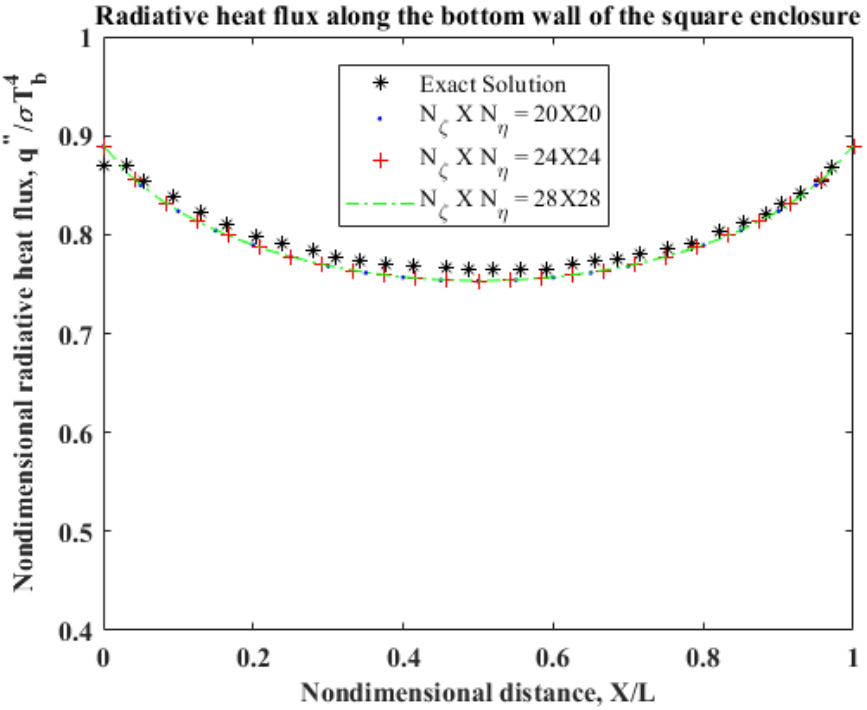
Radiative heat flux along the bottom wall of the square enclosure
Exact Solution
N_ζ X N_η = 20X20
N_ζ X N_η = 24X24
N_ζ X N_η = 28X28
Nondimensional radiative heat flux, q"/σT_b^4
Nondimensional distance, X/L
1
0.9
0.8
0.7
0.6
0.5
0.4
0
0.2
0.4
0.6
0.8
1

(b)

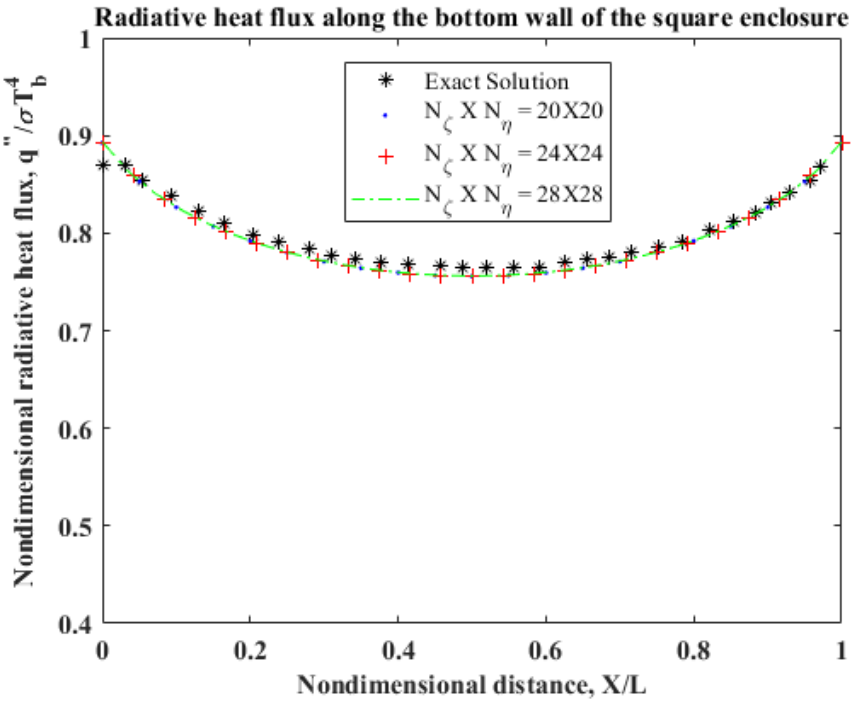

(c)

Fig. 10: Grid independence test of square enclosure for constant angular grids, (a) $N_\varphi \times N_\psi = 24 \times 48$, (b) $N_\varphi \times N_\psi = 36 \times 72$, and (c) $N_\varphi \times N_\psi = 48 \times 96$ with varying discrete spatial grids.

Validation:

After ensuring that the present numerical model is grid-independent, we compare our existing results to previously published solutions. The existing model can be applied with any spatial or angular grid. Fig. 11 (a) shows the grid generations for the $N_\xi \times N_\eta = 20 \times 20$ collocation points based on the body-fitted coordinate. The nondimensional radiative heat flux along the bottom wall of the square enclosure is plotted in Fig. 11 (b) for the constant absorption coefficient ($KL = 1$). Here, the simulation result is obtained

$N_\xi \times N_\eta = 20 \times 20$ spatial grids with $N_\varphi \times N_\psi = 24 \times 48$ discretized grids by polar and azimuthal angles. The present result shows excellent agreement with the exact solution [1]. The numerical results of RMSE and MAPE with the exact solution are 0.0198 and 2.45%, respectively.

Table 3: Grid independence test based on error calculations for constant angular nodes with varying spatial nodes of square enclosure.

Angular grids ($N_\varphi \times N_\psi$)	Spatial grids ($N_\xi \times N_\eta$)	Root-mean-square error	Mean absolute percentage error, %
24×48	20×20	0.0034	1.91
	24×24	0.0031	1.91
	28×28	0.0029	1.90
36×72	20×20	0.0023	1.25
	24×24	0.0021	1.23
	28×28	0.0019	1.20
48×96	20×20	0.0021	1.01
	24×24	0.0018	0.97
	28×28	0.0016	0.93

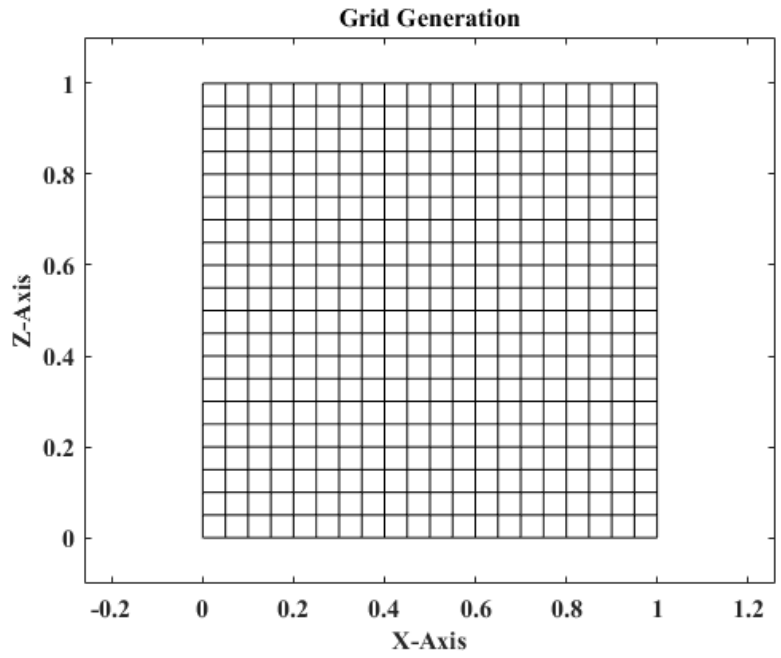

(a)

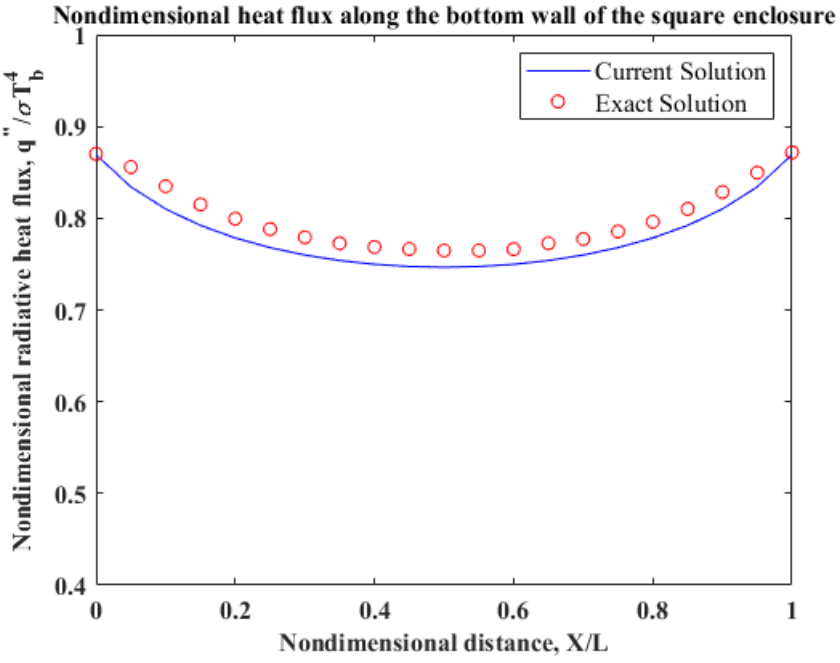

(b)

Fig. 11: (a) grid generation; (b) nondimensional radiative heat flux along the bottom wall of the square enclosure.

Rigid-body rotation:

Here, the modified square geometry (rigid-body rotation) is demonstrated for checking the effect of geometry skewness, as shown in . 12 (b). The modified square enclosure contains the same area ($1m^2$) as Fig. 8. This study is also considered radiative equilibrium and constant absorption coefficient ($KL = 1$) and considered the isothermal temperature T_w (with constant blackbody intensity T_{bw}) at AB wall and the remaining walls contain zero temperature, with all four surfaces being black. The discrete ordinate method is applied to solve this problem.

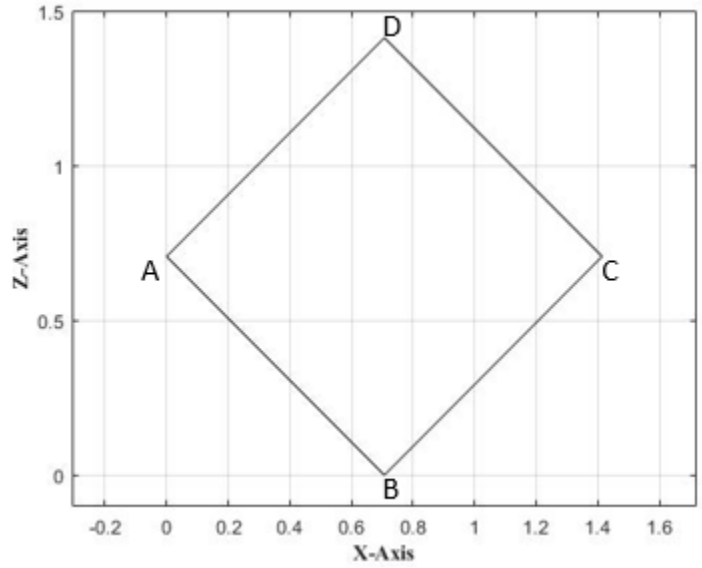

Fig. 12: Modified square enclosure.

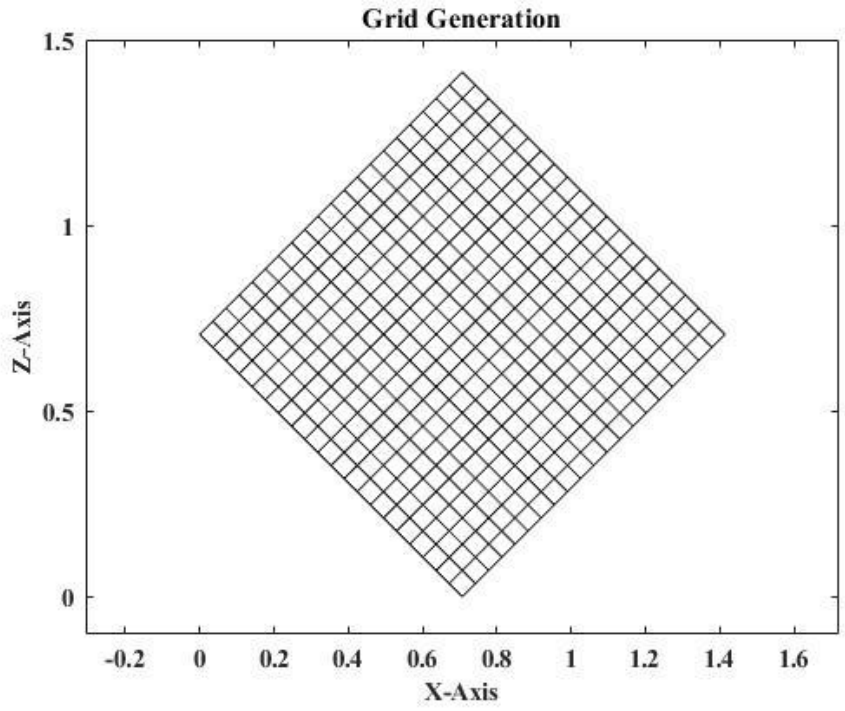

(a)

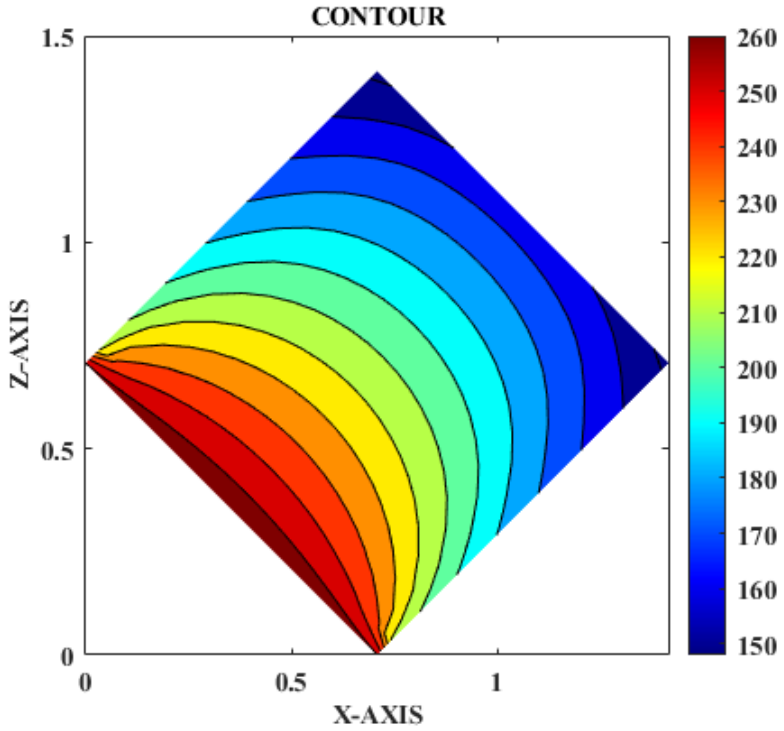

(b)

Fig. 13: (a) Grid generation; (b) temperature contour for the modified square geometry.

Fig. 13 (a) shows the $N_\xi \times N_\eta = 20 \times 20$ spatial grids based on the body-fitted coordinate. Fig. 13 (b) illustrates the temperature contour of modified square geometry for constant absorption coefficient ($KL = 1$). The figure depicts how the temperature is spread throughout the enclosure because the temperature is higher at the AB wall and zero at the other walls. The heat flux vector plot of a modified square enclosure is shown in Fig. 14. The diagram clearly shows how the heat flux is spread inside the enclosure. Fig. 15 shows the dimensionless radiative heat flux at the bottom wall of the modified square enclosures for the constant absorption coefficient ($KL = 1$). The numerical result is obtained discretizing with $N_\xi \times N_\eta = 20 \times 20$ spatial grids and $N_\varphi \times N_\psi = 24 \times 48$ angular discretization. The nondimensional radiative heat flux at the bottom wall of the modified square geometry fully matches the original square geometry. These results are pretty close to the exact solution [1].

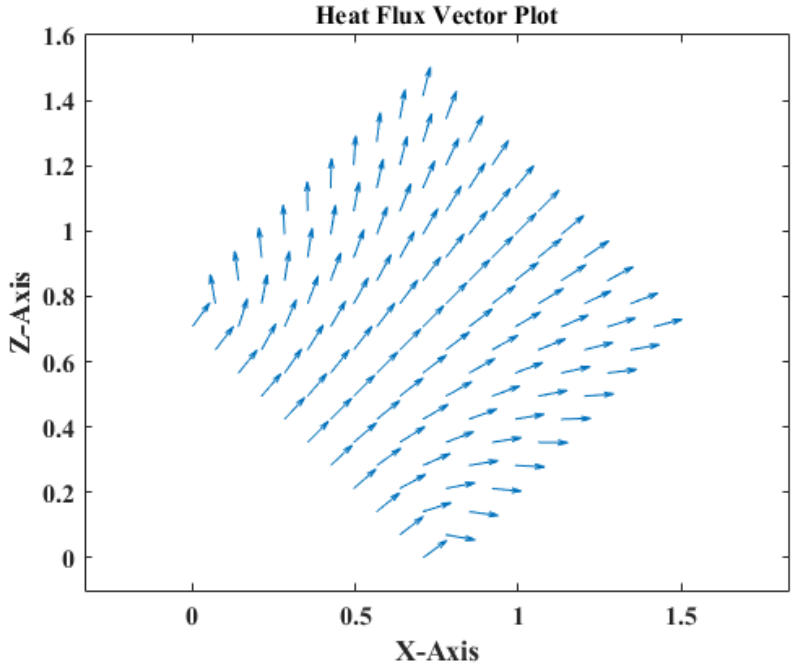

Fig. 14: Heat flux vector for a modified square enclosure.

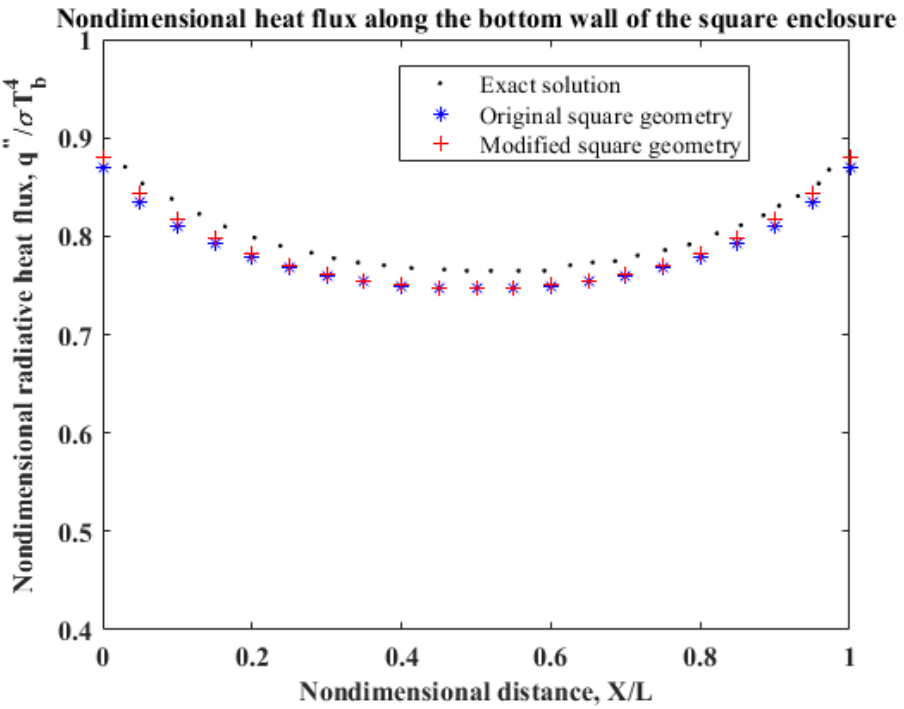

Fig. 15: Dimensionless heat flux at the bottom wall of modified and original square geometries.

5.2.2 Absorbing emitting and isotropically scattering homogeneous medium in a quadrilateral enclosure

The second problem is considered a quadrilateral enclosure that other researchers previously studied [90,126] to validate complex enclosures. This irregular enclosure is described the coordinate of (0,0), (2.2,0), (1.8,1.2), and (0.5,1.0). Here, all dimensions are considered in the meter (Fig. 16). A non-radiative equilibrium is considered with a constant temperature T_g and cold boundaries ($T_w = 0$) in this problem. All walls of the enclosure are considered black. Three different absorption coefficients are examined with an

absorbing-emitting and an isotropically scattered homogeneous medium. We are also assumed a characteristic length of the computational domain is 1m.

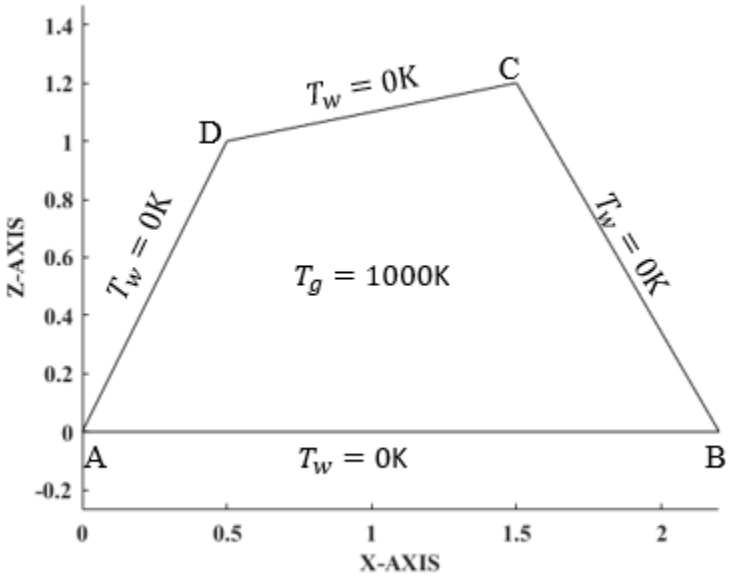

Fig. 16**:** Physical problem for an absorbing emitting and isotropically scattering homogeneous medium in a quadrilateral enclosure.

Grid Independence:

This case study is investigated the grid independence test based on the error calculations by varying the spatial grid $(N_\xi \times N_\eta)$ with a constant angular grid $(N_\varphi \times N_\psi)$ and by varying the angular grid $(N_\varphi \times N_\psi)$ with a constant spatial grid $(N_\xi \times N_\eta)$. Fig. 17 (a), (b), and (c) show the nondimensional radiative heat flux along the bottom wall in the quadrilateral enclosure for three different $N_\varphi \times N_\psi = 24 \times 48$, $N_\varphi \times N_\psi = 36 \times 72$, and $N_\varphi \times N_\psi = 48 \times 96$ angular grids with constant (a) $N_\xi \times N_\eta = 18 \times 18$, (b) $N_\xi \times N_\eta =$

20×20, and (c) $N_\xi \times N_\eta = 22 \times 22$ spatial grids, respectively. All figures are plotted for three different absorption coefficients. These figures are also compared the

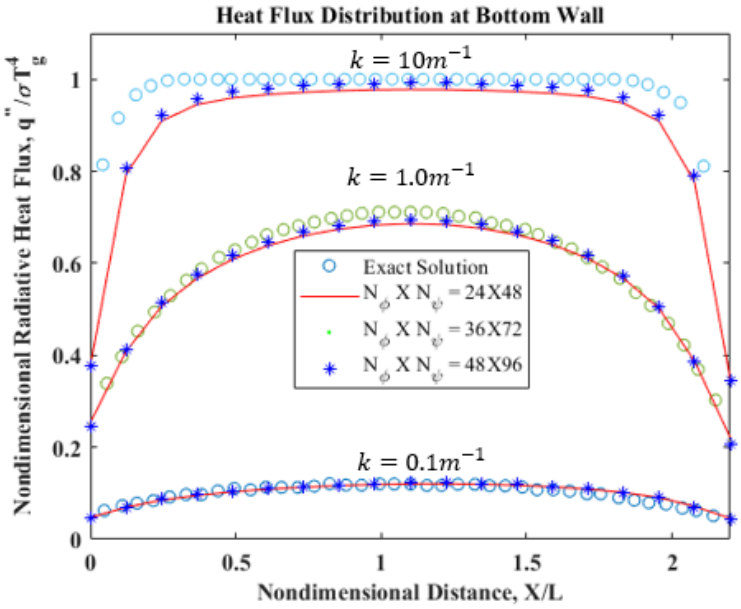

$(a)\ N_\xi \times N_\eta = 18 \times 18$

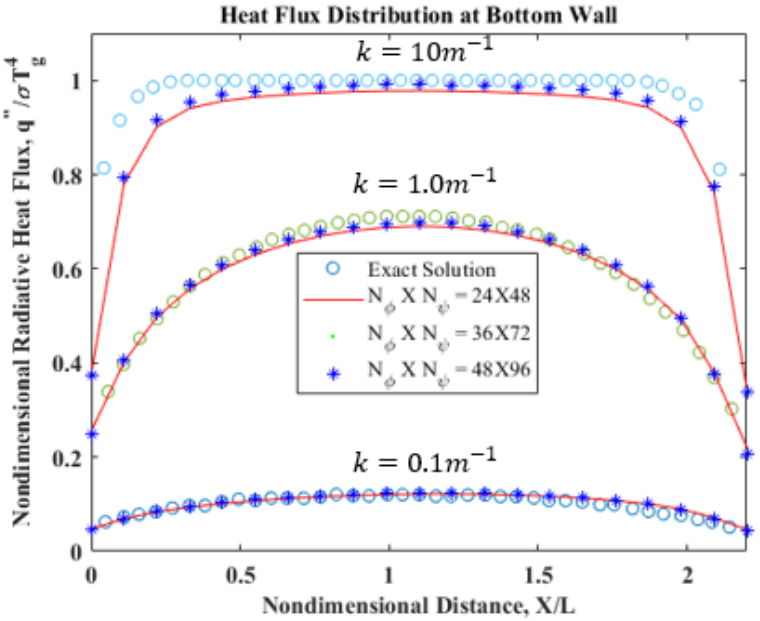

$(b)\ N_\xi \times N_\eta = 20 \times 20$

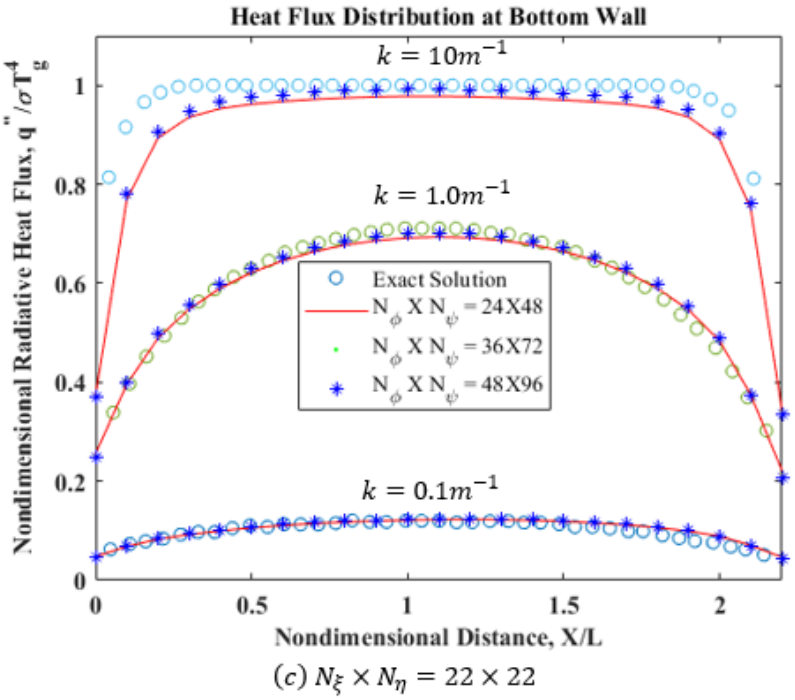

$(c)\ N_\xi \times N_\eta = 22 \times 22$

Fig. 17: Grid independence for dimensionless heat flux at the bottom wall in a quadrilateral enclosure for constant spatial grids, (a) $N_\xi \times N_\eta = 18 \times 18$, (b) $N_\xi \times N_\eta = 20 \times 20$, and (c) $N_\xi \times N_\eta = 22 \times 22$ with varying discrete angular grids.

nondimensional radiative heat flux for existing solutions with the exact solutions. Results show that the numerical solutions slightly deviate from the real solutions. Table 4 demonstrates the root-mean-square error and mean absolute percentage error for the nondimensional radiative heat flux of the existing numerical model with the exact solution for three different absorption coefficients. The table shows that the error decreases by increasing the spatial or angular grids with constant angular or spatial grids. For instance, the RMSR reduces from 0.0014 to 0.0012 by increasing from $N_\xi \times N_\eta = 18 \times 18$ to $N_\xi \times N_\eta = 22 \times 22$ spatial grids with constant $N_\varphi \times N_\psi = 24 \times 48$ angular grids for the

absorption coefficient of $k = 0.1m^{-1}$. And for absorption coefficients of $k = 1m^{-1}$and $k = 10m^{-1}$, the RMSE drops from 0.0066 to 0.0050 and 0.0080 to 0.0056 by increasing from $N_\xi \times N_\eta = 18 \times 18$ to $N_\xi \times N_\eta = 22 \times 22$ the spatial grids with constant $N_\varphi \times N_\psi = 24 \times 48$ angular grids. The maximum RMSE is 0.0080 for the absorption coefficient of $k = 10m^{-1}$ of $N_\xi \times N_\eta = 18 \times 18$ spatial grids with $N_\varphi \times N_\psi = 24 \times 48$ angular grids. On the other hand, the maximum MAPE is 5.91% for the absorption coefficient of $k = 0.1m^{-1}$ of $N_\xi \times N_\eta = 18 \times 18$ spatial grids with $N_\varphi \times N_\psi = 24 \times 48$ angular grids. The minimum MAPE is 2.06% for the absorption coefficient of $k = 10m^{-1}$ of $N_\xi \times N_\eta = 22 \times 22$ spatial grids with $N_\varphi \times N_\psi = 48 \times 96$ angular grids. The MAPE is decreased by 0.71% of $N_\xi \times N_\eta = 22 \times 22$ the spatial grids with changing the angular grids of $N_\varphi \times N_\psi = 24 \times 48$ to $N_\varphi \times N_\psi = 48 \times 96$ for the absorption coefficient of $k = 10m^{-1}$. This indicates that the error difference is very low for changing the spatial or angular grids with varying the angular or spatial grids. But for the approximate solutions, we can allow these solutions in terms of the complexities of the numerical technique. In this case, we can choose the smaller number of spatial grids with the smaller number of directional grids.

On the other hand, Fig. 18 (a), (b), and (c) show the nondimensional radiative heat flux along the bottom wall in the quadrilateral enclosure for three different spatial grids ($N_\xi \times N_\eta = 18 \times 18$, $N_\xi \times N_\eta = 20 \times 20$, and $N_\xi \times N_\eta = 22 \times 22$) with varying (a) $N_\varphi \times N_\psi = 24 \times 48$, (b) $N_\varphi \times N_\psi = 36 \times 72$, and (c) $N_\varphi \times N_\psi = 48 \times 96$ angular grids, respectively. Table **5** illustrates root-mean-square error (RMSE) and mean absolute

percentage error (MAPE) calculations for constant angular grids with varying spatial grids at the bottom wall in a quadrilateral enclosure.

Table 4: Grid independence test based on root-mean-square error (RMSE) and mean absolute percentage error (MAPE) calculations for constant spatial grids with varying angular grids at the bottom wall in a quadrilateral enclosure.

Angular Grids $(\mathbf{N_\varphi \times N_\psi})$	**Absorption coefficients k, m^{-1}**	**Spatial Grids** $(\mathbf{N_\xi \times N_\eta})$					
		18×18		20×20		22×22	
		RMSE	MAPE, %	RMSE	MAPE, %	RMSE	MAPE, %
24 × 48	0.1	0.0014	5.91	0.0012	5.69	0.0012	5.51
	1.0	0.0066	4.13	0.0056	3.91	0.0050	3.86
	10.0	0.0080	3.36	0.0065	3.02	0.0056	2.77
36 × 72	0.1	0.0012	5.42	0.0011	5.23	0.0010	5.14
	1.0	0.0057	3.88	0.0048	3.67	0.0044	3.72
	10.0	0.0071	2.73	0.0058	2.36	0.0050	2.06
48 × 96	0.1	0.0012	5.22	0.0011	5.04	0.0010	5.04
	1.0	0.0054	3.86	0.0046	3.67	0.0043	3.70
	10.0	0.0069	2.73	0.0057	2.37	0.0049	2.06

The maximum RMSE error is 0.0080 of $N_\xi \times N_\eta = 18 \times 18$ with $N_\varphi \times N_\psi = 24 \times 48$ for $k = 10m^{-1}$ and the minimum RMSE error is 0.0010 of $N_\xi \times N_\eta = 22 \times 22$ with $N_\varphi \times N_\psi = 48 \times 96$ for $k = 0.1m^{-1}$. On the other hand, the maximum MAPE error is 5.91% of $N_\xi \times N_\eta = 18 \times 18$ with $N_\varphi \times N_\psi = 24 \times 48$ for the absorption coefficient of $k = 0.1m^{-1}$ and the minimum MAPE error is 2.06% of $N_\xi \times N_\eta = 22 \times 22$ with $N_\varphi \times N_\psi = 48 \times 96$ for the absorption coefficient of $k = 10m^{-1}$.

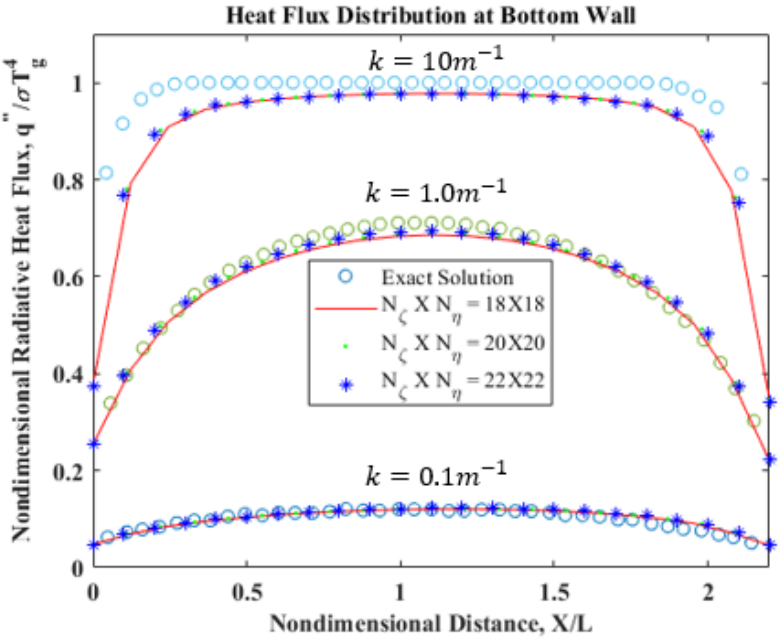

(a) $N_\varphi \times N_\psi = 24 \times 48$

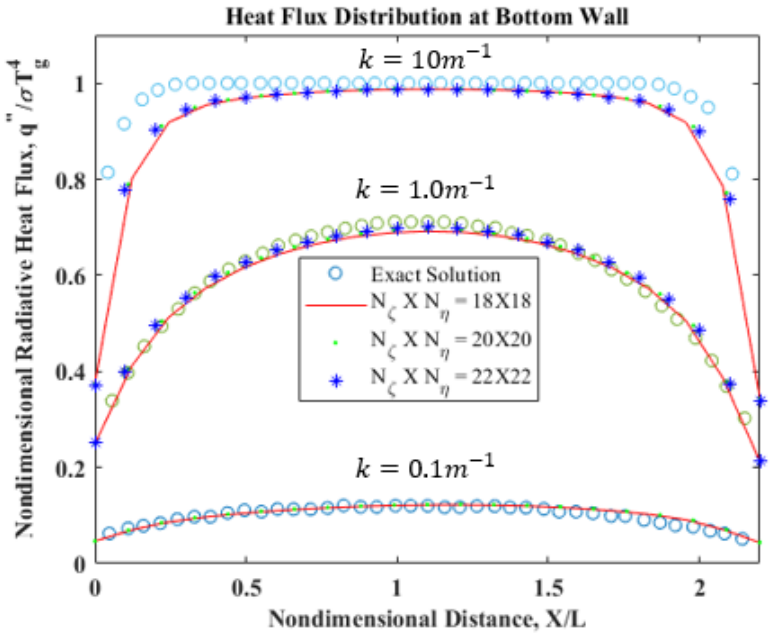

(b) $N_\varphi \times N_\psi = 36 \times 72$

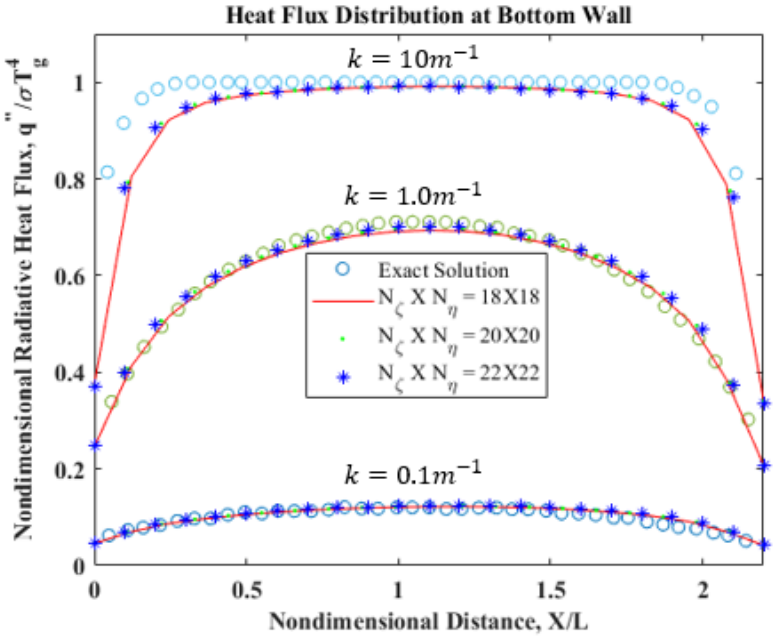

(c) $N_\varphi \times N_\psi = 48 \times 96$

Fig. 18: Grid independence for dimensionless heat flux at the bottom wall in a quadrilateral enclosure for constant angular spatial grids, (a) $N_\varphi \times N_\psi = 24 \times 48$, (b) $N_\varphi \times N_\psi = 36 \times 72$, and (c) $N_\varphi \times N_\psi = 48 \times 96$ with varying spatial grids.

Validation:

Fig. 19 (a) shows grid generations of the $N_\xi \times N_\eta = 20 \times 20$ collocation points system based on BFC. The problem is solved the $N_\xi \times N_\eta = 20 \times 20$ spatial grids with $N_\varphi \times N_\psi = 24 \times 48$ directional grids. The nondimensional radiative heat fluxes at the bottom wall are plotted in Fig. 19 (b) for three values of absorption coefficients, namely, $k = 0.1m^{-1}$, $k = 1m^{-1}$, and $k = 10m^{-1}$ respectively. The existing numerical solutions are compared to the exact solutions. According to the study, the present solutions reasonably agree with the exact values. The maximum RMSE and MAPE are 0.008 and 5.91%, respectively, compared with the exact solutions.

As shown in Fig. 19 (a), the absorption coefficient substantially impacts the radiative heat flux distributions on the bottom wall. The radiative heat flow on the bottom wall is primarily a function of the surface temperature when the absorption coefficient is as low as $k = 0.1m^{-1}$; when the wall temperatures are equal to zero, the radiative heat flux is relatively weak. Otherwise, the radiative heat flux on the bottom wall of an optically thick media is mainly controlled by the medium temperature: if the medium temperature is T_g, the radiative heat flux will be close to σT_g^4.

Table 5: Grid independence test based on root-mean-square error (RMSE) and mean absolute percentage error (MAPE) calculations for constant angular grids with varying spatial grids at the bottom wall in a quadrilateral enclosure.

Spatial Grids $(\mathbf{N_\xi \times N_\eta})$	**Absorption coefficients k, m^{-1}**	**Angular Grids** $(\mathbf{N_\varphi \times N_\psi})$					
		24×48		36×72		48×96	
		RMSE	MAPE, %	RMSE	MAPE, %	RMSE	MAPE, %
18×18	0.1	0.0014	5.91	0.0012	5.42	0.0012	5.22
	1.0	0.0066	4.13	0.0057	3.88	0.0054	3.86
	10.0	0.0080	3.36	0.0071	2.73	0.0069	2.73
20×20	0.1	0.0012	5.69	0.0011	5.23	0.0011	5.04
	1.0	0.0056	3.91	0.0048	3.67	0.0046	3.67
	10.0	0.0065	3.02	0.0058	2.36	0.0057	2.36
22×22	0.1	0.0012	5.51	0.0010	5.14	0.0010	5.04
	1.0	0.0050	3.86	0.0044	3.72	0.0043	3.70
	10.0	0.0056	2.77	0.0050	2.06	0.0049	2.06

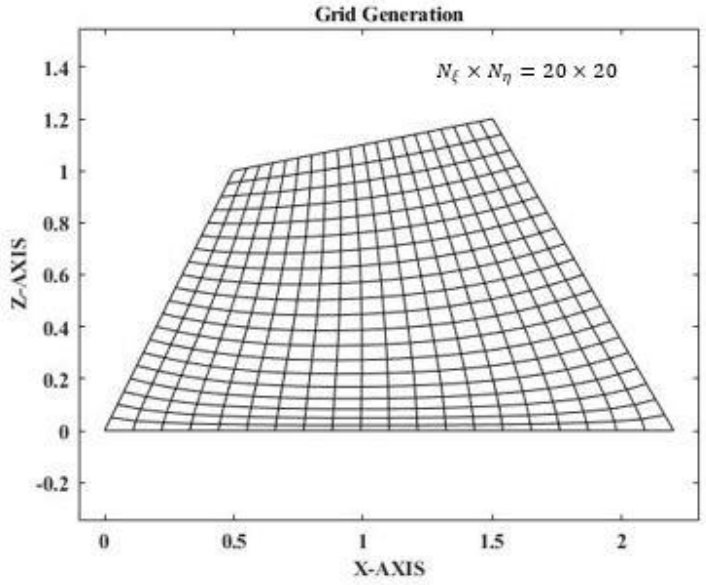

(a)

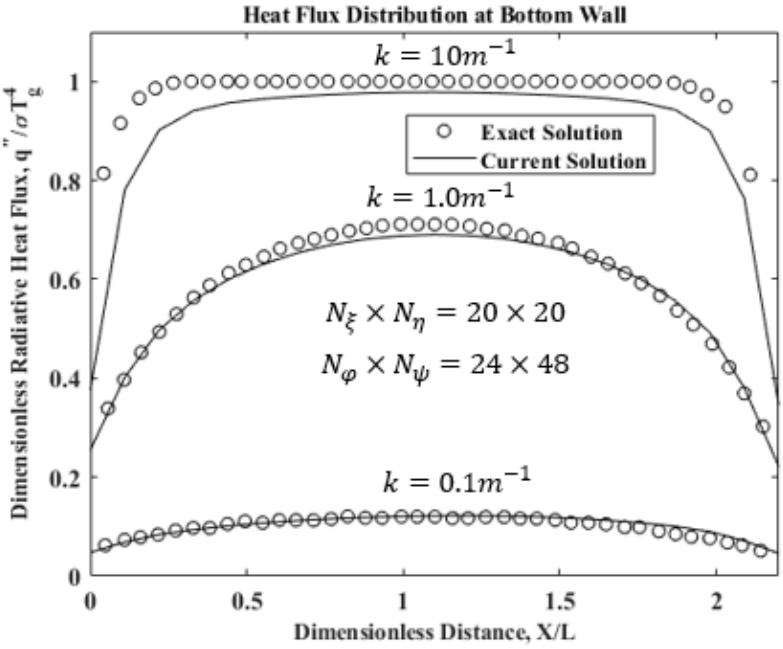

(b)

Fig. 19: (a) grid generation; (b) Nondimensional radiative heat flux the bottom wall of a quadrilateral enclosure.

Secondly, we are considered another problem in the same quadrilateral enclosure in Fig. 20 (a). The geometry is assumed to be filled with a purely scattering medium at constant zero temperature ($T_g = 0K$), and the walls are assumed to be black and cold ($T_w = 0K$), except for the bottom wall, where $T_{AB} = 300K$. In this case, the extinction coefficient is considered of $\beta_o = 1m^{-1}$. This problem is solved $N_\xi \times N_\eta = 18 \times 18$ spatial grids with $N_\varphi \times N_\psi = 24 \times 48$ angular grids. Fig. 20 (b) shows the nondimensional radiative heat flux $q_{BC}/\sigma T_{AB}^4$ on the BC wall of quadrilateral enclosure. Compared with the collocation spectral method (CSM) [95], the maximum RMSE and MAPE of present works are less than 0.00362 and 3.4312%, respectively.

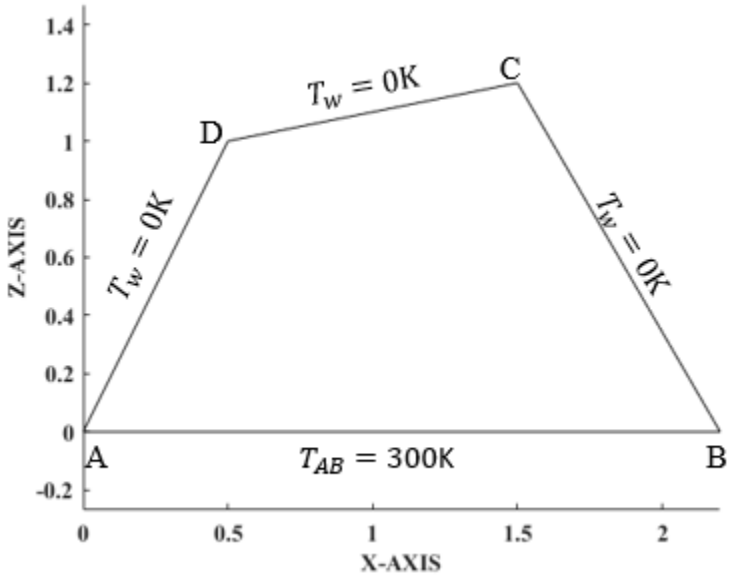

(a)

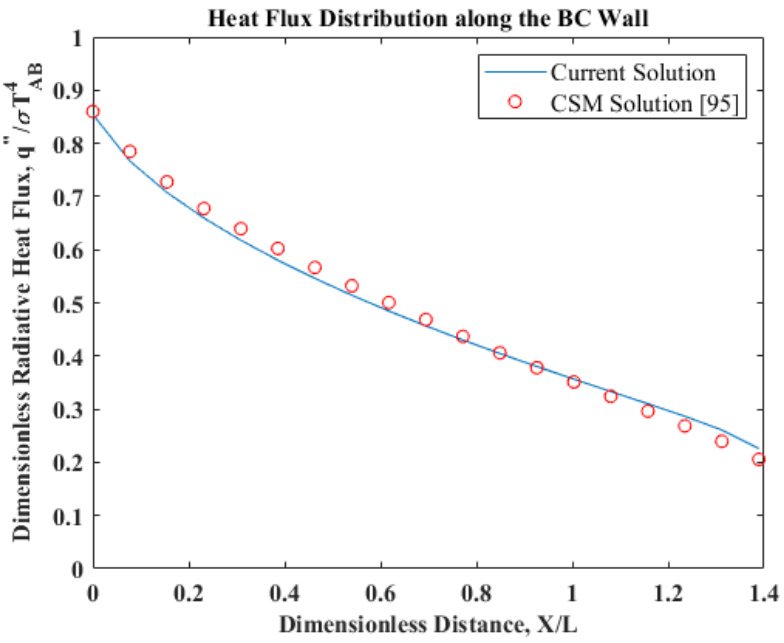

(b)

Fig. 20: (a) Geometry and boundary conditions; (b) nondimensional radiative heat flux along the BC wall of the quadrilateral enclosure.

5.2.3 Non-scattering homogeneous medium in a trapezoidal enclosure

In this case, radiative heat transfer in a two-dimensional trapezoidal enclosure filled with a non-scattering gray medium is considered, as shown in Fig. 21. The dimensions of Cartesian system of the trapezoidal enclosure are (0,0), (1,0), (1,1), (0.8,1), and (0,0.5). The unit of all dimensions is assumed in meters. The medium temperature T_g is kept as an isothermally at 1000K, but all boundary walls' temperature is maintained at $T_w = 0K$. All the boundary walls are considered black. Three different absorption coefficients are considered with an absorbing-emitting and non-scattered gray medium. The characteristic length of the computational domain is assumed of L = 1 m.

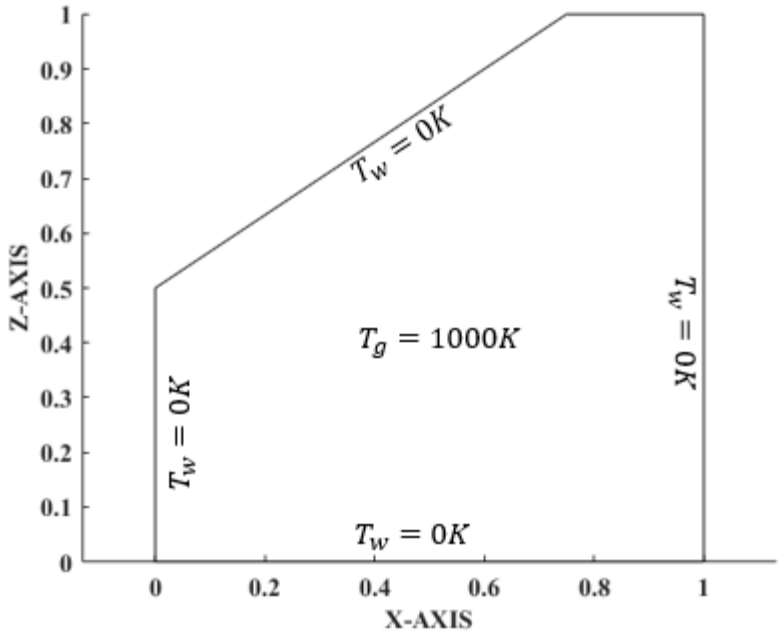

Fig. 21: Physical problem for non-scattering homogeneous medium in a trapezoidal enclosure.

Grid Independence:

This study is examined the grid independence test based on the error calculations for both bottom and top walls varying the spatial grid ($N_\xi \times N_\eta$) with a constant angular grid ($N_\varphi \times N_\psi$) and by varying the angular grid ($N_\varphi \times N_\psi$) with a constant spatial grid ($N_\xi \times N_\eta$). Fig. 22 (a), (b), and (c) show the nondimensional radiative heat flux along the bottom wall in the trapezoidal enclosure for three different $N_\varphi \times N_\psi = 24 \times 48$, $N_\varphi \times N_\psi = 36 \times 72$, and $N_\varphi \times N_\psi = 48 \times 96$ angular grids with constant (a) $N_\xi \times N_\eta = 18 \times 18$, (b) $N_\xi \times N_\eta = 20 \times 20$, and (c) $N_\xi \times N_\eta = 22 \times 22$ spatial grids, respectively. These figures are also compared the nondimensional radiative heat flux for existing

solutions with the exact solutions. Results show that the numerical solutions slightly deviate from the actual solutions.

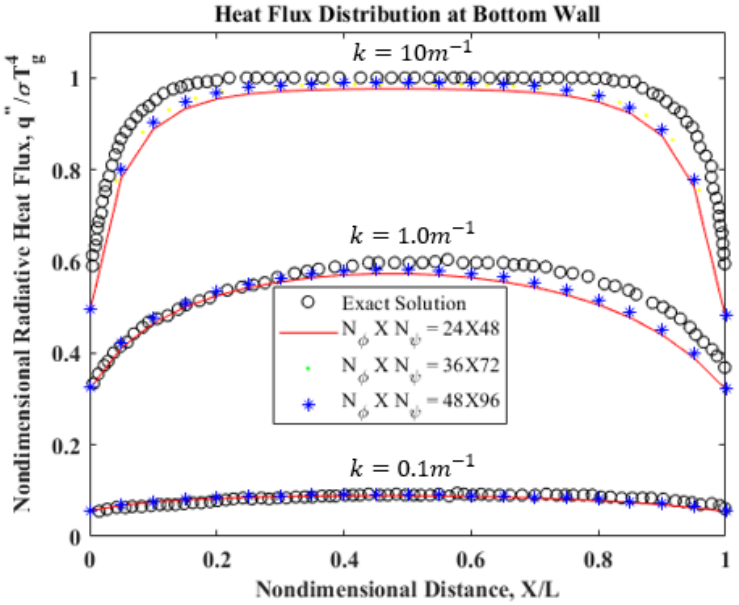

$(a)\ N_\xi \times N_\eta = 20 \times 20$

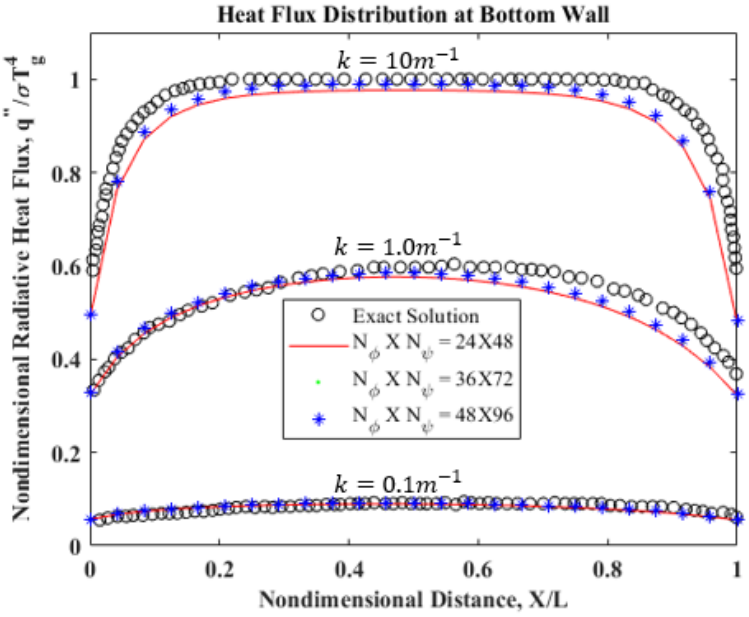

$(b)\ N_\xi \times N_\eta = 24 \times 24$

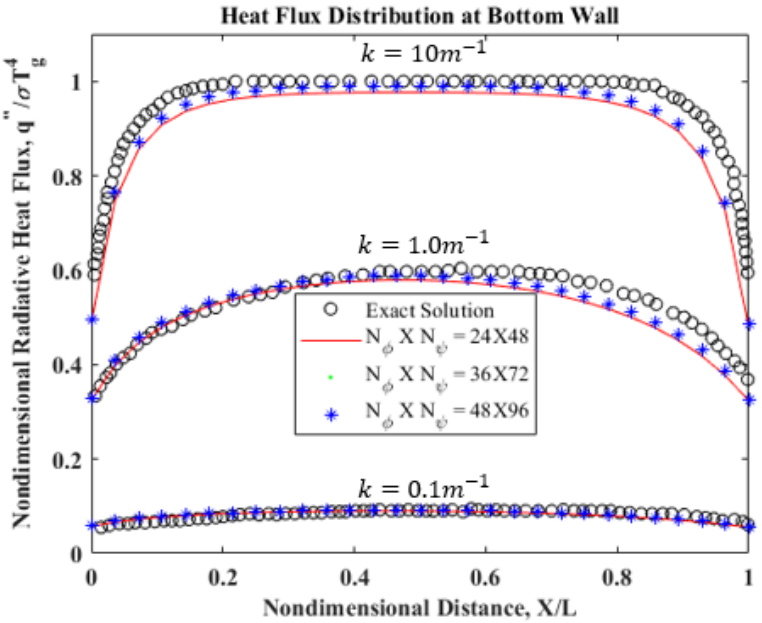

$(c)\ N_\xi \times N_\eta = 28 \times 28$

Fig. 22: Grid independence test for dimensionless heat flux at the bottom wall in a trapezoidal enclosure for constant spatial grids, (a) $N_\xi \times N_\eta = 20 \times 20$, (b) $N_\xi \times N_\eta = 24 \times 24$, and (c) $N_\xi \times N_\eta = 28 \times 28$ with varying angular grids.

Table 6 demonstrates the RMSE and the MAPE for the nondimensional radiative heat flux of the existing numerical model with the exact solution for three different absorption coefficients. The table shows that the error decreases by increasing the spatial or angular grids with constant angular or spatial grids. For instance, the RMSR reduces from 0.0108 to 0.0079 by increasing from $N_\xi \times N_\eta = 20 \times 20$ to $N_\xi \times N_\eta = 28 \times 28$ spatial grids with constant $N_\varphi \times N_\psi = 36 \times 72$ angular grids for the absorption coefficient of $k = 10m^{-1}$. And for absorption coefficients of $k = 0.1m^{-1}$and $k = 1m^{-1}$, the RMSR drops from 0.0013 to 0.0011 and 0.0064 to 0.0048 by increasing from $N_\xi \times N_\eta = 20 \times 20$ to

Table 6: Grid independence test based on root-mean-square error (RMSE) and mean absolute percentage error (MAPE) calculations for constant spatial grids with varying angular grids at the bottom wall in a trapezoidal enclosure.

Angular Grids $(\mathbf{N_\varphi \times N_\psi})$	**Absorption coefficients k, m^{-1}**	**Spatial Grids** $(\mathbf{N_\xi \times N_\eta})$					
		20× 20		24×24		28×28	
		RMSE	MAPE, %	RMSE	MAPE, %	RMSE	MAPE, %
24 × 48	0.1	0.0014	6.68	0.0013	6.66	0.0012	6.62
	1.0	0.0075	5.42	0.0063	4.78	0.0056	4.55
	10.0	0.0125	5.73	0.0105	5.28	0.0094	5.02
36 × 72	0.1	0.0013	6.28	0.0012	6.24	0.0011	6.21
	1.0	0.0064	4.40	0.0053	4.17	0.0048	4.06
	10.0	0.0108	4.73	0.0090	4.28	0.0079	4.01
48 × 96	0.1	0.0013	6.21	0.0012	6.21	0.0011	6.21
	1.0	0.0059	4.24	0.0050	3.98	0.0045	3.88
	10.0	0.0102	4.33	0.0084	3.87	0.0074	3.61

$N_\xi \times N_\eta = 28 \times 28$ the spatial grids with constant $N_\varphi \times N_\psi = 36 \times 72$ angular grids. The maximum MAPE is 6.68% for the absorption coefficient of $k = 0.1m^{-1}$ of $N_\xi \times N_\eta = 20 \times 20$ spatial grids with $N_\varphi \times N_\psi = 24 \times 48$ angular grids. On the other

hand, the maximum RMSE is 0.0125 for the absorption coefficient of $k = 10m^{-1}$ of $N_\xi \times N_\eta = 20 \times 20$ spatial grids with $N_\varphi \times N_\psi = 24 \times 48$ angular grids. The minimum MAPE is 3.61% for the absorption coefficient of $k = 10m^{-1}$ of $N_\xi \times N_\eta = 28 \times 28$ spatial grids with $N_\varphi \times N_\psi = 48 \times 96$ angular grids. The RMSE is decreased by 0.0023 of $N_\xi \times N_\eta = 20 \times 20$ the spatial grids with changing the angular grids of $N_\varphi \times N_\psi = 24 \times 48$ to $N_\varphi \times N_\psi = 48 \times 96$ for the absorption coefficient of $k = 10m^{-1}$.

On the other hand, Fig. 23 (a), (b), and (c) show the nondimensional radiative heat flux along the bottom wall in the trapezoidal enclosure for three different spatial grids ($N_\xi \times N_\eta = 18 \times 18$, $N_\xi \times N_\eta = 20 \times 20$, and $N_\xi \times N_\eta = 22 \times 22$) with varying (a) $N_\varphi \times N_\psi = 24 \times 48$, (b) $N_\varphi \times N_\psi = 36 \times 72$, and (c) $N_\varphi \times N_\psi = 48 \times 96$ angular grids, respectively. Table **7** shows the RMSE and the MAPE measurements for constant angular grids with varying spatial grids at the bottom wall in a quadrilateral enclosure for three different absorption coefficients. Table **7** illustrates that the error decreases by increasing the spatial or angular grid with a constant angular or spatial grid for the same absorption coefficient. The maximum RMSE error is 0.0125 of $N_\xi \times N_\eta = 20 \times 20$ with $N_\varphi \times N_\psi = 24 \times 48$ for $k = 10m^{-1}$ and the minimum RMSE error is 0.0011 of $N_\xi \times N_\eta = 28 \times 28$ with both $N_\varphi \times N_\psi = 36 \times 72$ and $N_\varphi \times N_\psi = 48 \times 96$ for $k = 0.1m^{-1}$. In addition, the maximum MAPE error is 6.68% of $N_\xi \times N_\eta = 20 \times 20$ with $N_\varphi \times N_\psi = 24 \times 48$ for the absorption coeffient of $k = 0.1m^{-1}$ and the minimum MAPE error is 3.61% of $N_\xi \times N_\eta = 28 \times 28$ with $N_\varphi \times N_\psi = 48 \times 96$ for for the absorption coeffient of $k = 10m^{-1}$.

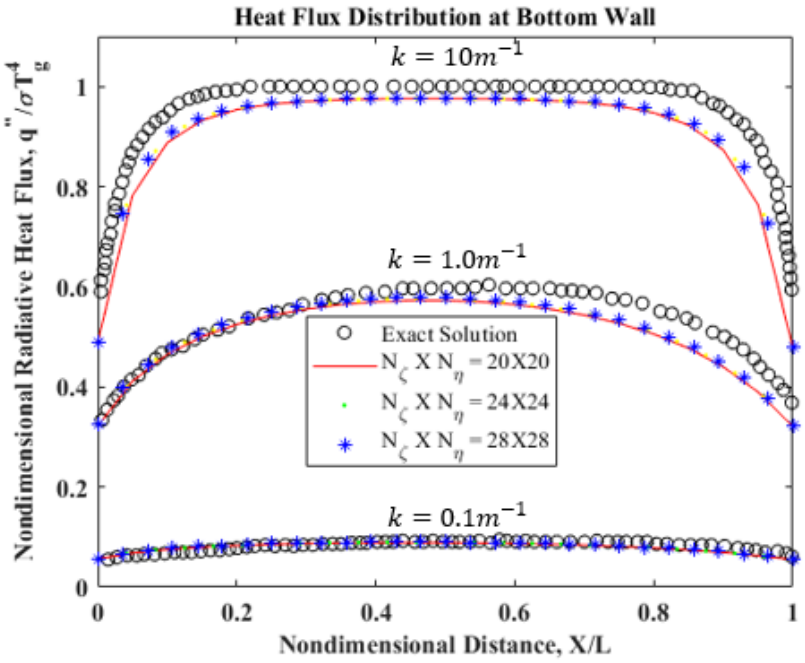

(a) $N_\varphi \times N_\psi = 24 \times 48$

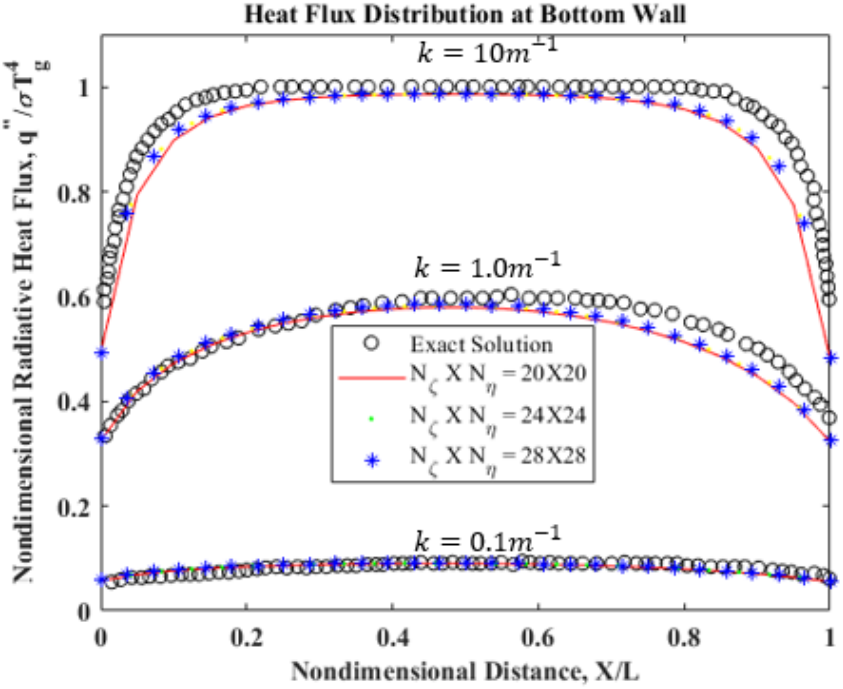

(b) $N_\varphi \times N_\psi = 36 \times 72$

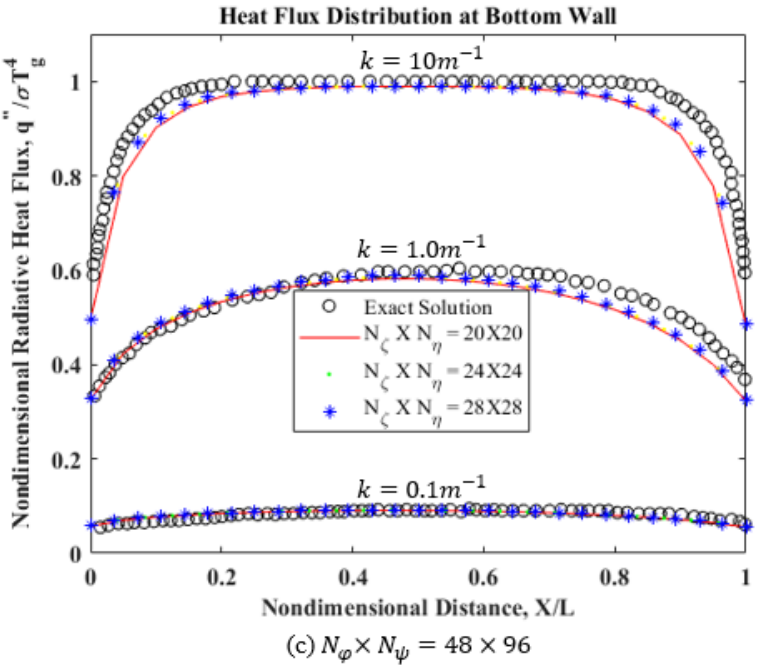

(c) $N_\varphi \times N_\psi = 48 \times 96$

Fig. 23: Grid independence test for dimensionless heat flux at the bottom wall in a trapezoidal enclosure for constant angular spatial grids, (a) $N_\varphi \times N_\psi = 24 \times 48$, (b) $N_\varphi \times N_\psi = 36 \times 72$, and (c) $N_\varphi \times N_\psi = 48 \times 96$ with varying spatial grids.

Fig. 22 and Fig. 23 represent the grid independence of nondimensional radiative heat flux for the trapezoidal enclosure along the bottom wall. Now, we investigate the grid independence of nondimensional radiative heat flux for the trapezoidal enclosure along the top wall. Fig. 24 (a), (b), and (c) show the nondimensional radiative heat flux along the top wall in the trapezoidal enclosure for three different $N_\varphi \times N_\psi = 24 \times 48$, $N_\varphi \times N_\psi = 36 \times 72$, and $N_\varphi \times N_\psi = 48 \times 96$ angular grids with constant (a) $N_\xi \times N_\eta = 18 \times 18$, (b) $N_\xi \times N_\eta = 20 \times 20$, and (c) $N_\xi \times N_\eta = 22 \times 22$ spatial grids, respectively.

Table 7: Grid independence test based on root-mean-square error (RMSE) and mean absolute percentage error (MAPE) calculations for constant angular grids with varying spatial grids at the bottom wall in a trapezoidal enclosure.

Spatial Grids $(\mathbf{N_\xi \times N_\eta})$	**Absorption coefficients k, m^{-1}**	**Angular Grids** $(\mathbf{N_\varphi \times N_\psi})$					
		24×48		36×72		48×96	
		RMSE	MAPE, %	RMSE	MAPE, %	RMSE	MAPE, %
20×20	0.1	0.0014	6.68	0.0013	6.28	0.0013	6.21
	1.0	0.0075	5.42	0.0064	4.40	0.0059	4.24
	10.0	0.0125	5.73	0.0108	4.73	0.0102	4.33
24×24	0.1	0.0013	6.66	0.0012	6.24	0.0012	6.21
	1.0	0.0063	4.78	0.0053	4.17	0.0050	3.98
	10.0	0.0105	5.28	0.0090	4.28	0.0084	3.87
28×28	0.1	0.0012	6.62	0.0011	6.21	0.0011	6.21
	1.0	0.0056	4.55	0.0048	4.06	0.0045	3.88
	10.0	0.0094	5.02	0.0079	4.01	0.0074	3.61

All results are compared the nondimensional radiative heat flux for existing solutions with the published exact solutions. Results show that the numerical solutions are notably in good agreement with the exact solutions. However, there is some deviation of existing numerical solutions with the exact solutions. This is because of the grid generation and the

numerical method error. The RMSE and the MAPE for the nondimensional radiative heat flux of present solutions with the exact solution for three distinct absorption coefficients ($\mathrm{k} = 0.1\mathrm{m}^{-1}, \mathrm{k} = 1\mathrm{m}^{-1}$, and $\mathrm{k} = 10\mathrm{m}^{-1}$) are illustrated in Table 8. The table indicates that raising the spatial or angular grid alone with constant angular or spatial grid reduces both errors. For example, the RMSE reduces from 0.0025 to 0.0021 by increasing from $N_\xi \times N_\eta = 20 \times 20$ to $N_\xi \times N_\eta = 28 \times 28$ spatial grids with constant $N_\varphi \times N_\psi = 24 \times 48$ angular grids for the absorption coefficient of $k = 0.1m^{-1}$. And for absorption coefficients of $k = 1m^{-1}$and $k = 10m^{-1}$, the RMSE drops from 0.0121 to 0.0095 and 0.0130 to 0.0107 by increasing from $N_\xi \times N_\eta = 20 \times 20$ to $N_\xi \times N_\eta = 28 \times 28$ the spatial grids with constant $N_\varphi \times N_\psi = 24 \times 48$ angular grids. The maximum RMSE is 0.0130 for the absorption coefficient of $k = 1m^{-1}$ of $N_\xi \times N_\eta = 20 \times 20$ spatial grids with $N_\varphi \times N_\psi = 24 \times 48$ angular grids. On the other hand, the maximum MAPE is 8.29% for the absorption coefficient of $k = 1m^{-1}$ of $N_\xi \times N_\eta = 20 \times 20$ spatial grids with $N_\varphi \times N_\psi = 24 \times 48$ angular grids. The minimum MAPE is 3.64% for the absorption coefficient of $k = 10m^{-1}$ of $N_\xi \times N_\eta = 28 \times 28$ spatial grids with $N_\varphi \times N_\psi = 48 \times 96$ angular grids. The MAPE is decreased by 0.72% of $N_\xi \times N_\eta = 28 \times 28$ the spatial grids with changing the angular grids of $N_\varphi \times N_\psi = 24 \times 48$ to $N_\varphi \times N_\psi = 48 \times 96$ for the absorption coefficient of $k = 0.1m^{-1}$. This indicates that the error difference is very low for changing the spatial or angular grids with varying the angular or spatial grids. But for the approximate solutions, we can allow these solutions in terms of the complexities of the numerical technique. In this case, we may choose the smaller number of spatial grids with the smaller number of directional grids.

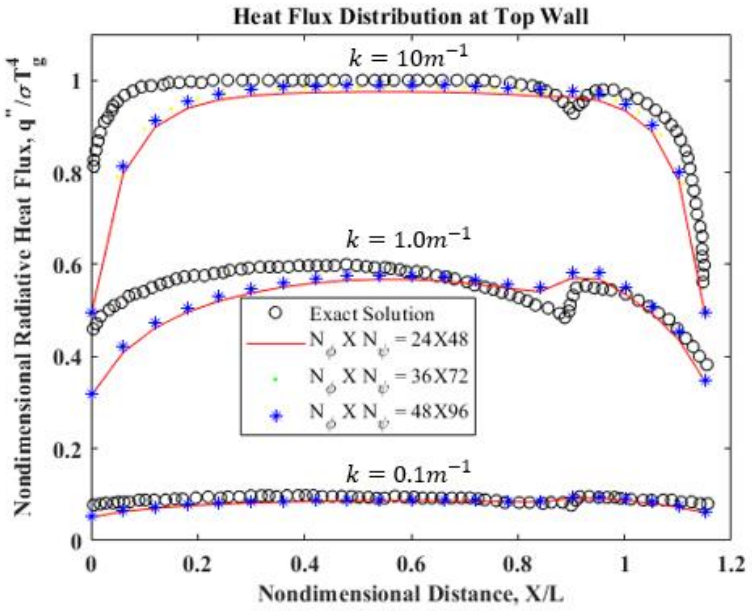

$(a)\ N_\xi \times N_\eta = 20 \times 20$

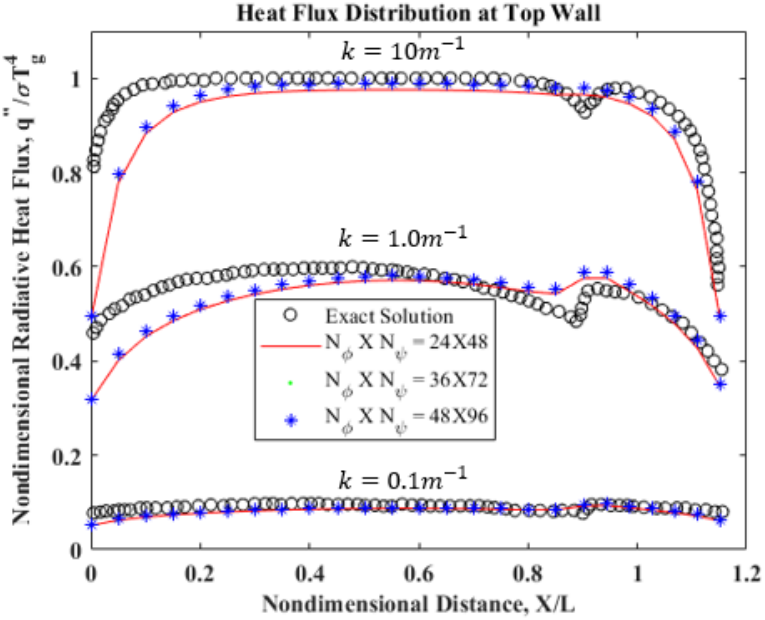

$(b)\ N_\xi \times N_\eta = 24 \times 24$

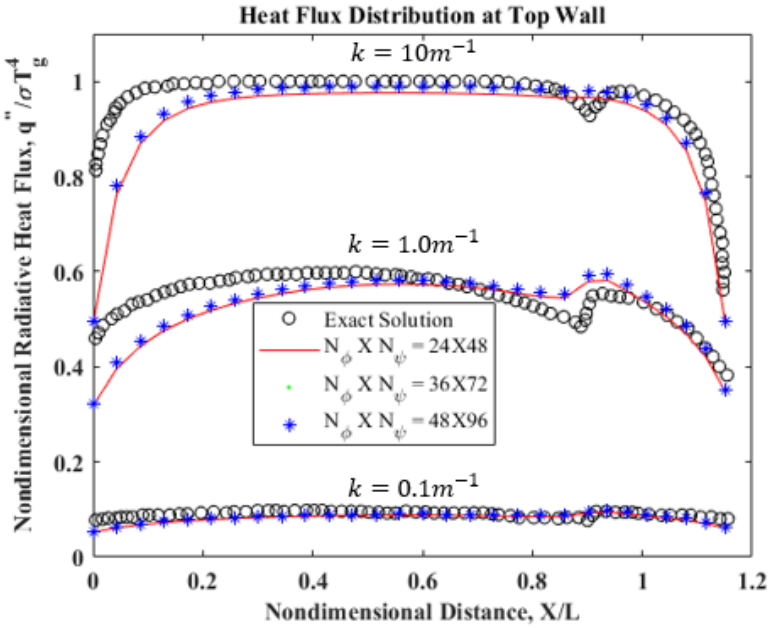

$(c)\ N_\xi \times N_\eta = 28 \times 28$

Fig. 24: Grid independence test for dimensionless heat flux at the top wall in a trapezoidal enclosure for constant spatial grids, (a) $N_\xi \times N_\eta = 20 \times 20$, (b) $N_\xi \times N_\eta = 24 \times 24$, and (c) $N_\xi \times N_\eta = 28 \times 28$ with varying angular grids.

On the other hand, Fig. 25 (a), (b), and (c) show the nondimensional radiative heat flux along the top wall in the trapezoidal enclosure for three different angular grids of (a) $N_\varphi \times N_\psi = 24 \times 48$, (b) $N_\varphi \times N_\psi = 36 \times 72$, and (c) $N_\varphi \times N_\psi = 48 \times 96$, with varying ($N_\xi \times N_\eta = 20 \times 20$, $N_\xi \times N_\eta = 24 \times 24$, and $N_\xi \times N_\eta = 28 \times 28$) spatial grids, respectively. Table 9 illustrates the RMSE and the MAPE calculations for constant angular grids with varying spatial grids at the top wall in a trapezoidal enclosure.

Table 8: Grid independence test based on root-mean-square error (RMSE) and mean absolute percentage error (MAPE) calculations for constant spatial grids with varying angular grids at the top wall in a trapezoidal enclosure.

Angular Grids $(\mathbf{N_\varphi \times N_\psi})$	**Absorption coefficients k, m^{-1}**	**Spatial Grids** $(\mathbf{N_\xi \times N_\eta})$					
		20× 20		24×24		28×28	
		RMSE	MAPE, %	RMSE	MAPE, %	RMSE	MAPE, %
24 × 48	0.1	0.0025	7.35	0.0022	7.25	0.0021	7.21
	1.0	0.0121	8.29	0.0105	7.73	0.0095	7.45
	10.0	0.0130	5.18	0.0117	5.04	0.0107	4.92
36 × 72	0.1	0.0023	6.85	0.0021	6.78	0.0019	6.72
	1.0	0.0114	7.56	0.0099	7.10	0.0090	6.81
	10.0	0.0114	4.29	0.0103	4.14	0.0094	4.00
48 × 96	0.1	0.0022	6.63	0.0020	6.53	0.0019	6.49
	1.0	0.0111	7.31	0.0097	6.85	0.0088	6.61
	10.0	0.0108	3.95	0.0098	3.79	0.0089	3.64

The maximum MAPE error is 8.29% of $N_\xi \times N_\eta = 20 \times 20$ with $N_\varphi \times N_\psi = 24 \times 48$ for $k = 1m^{-1}$ and the minimum MAPE error is 3.64% of $N_\xi \times N_\eta = 28 \times 28$ with $N_\varphi \times N_\psi = 48 \times 96$ for $k = 10m^{-1}$. On the other hand, the maximum RMSE error is

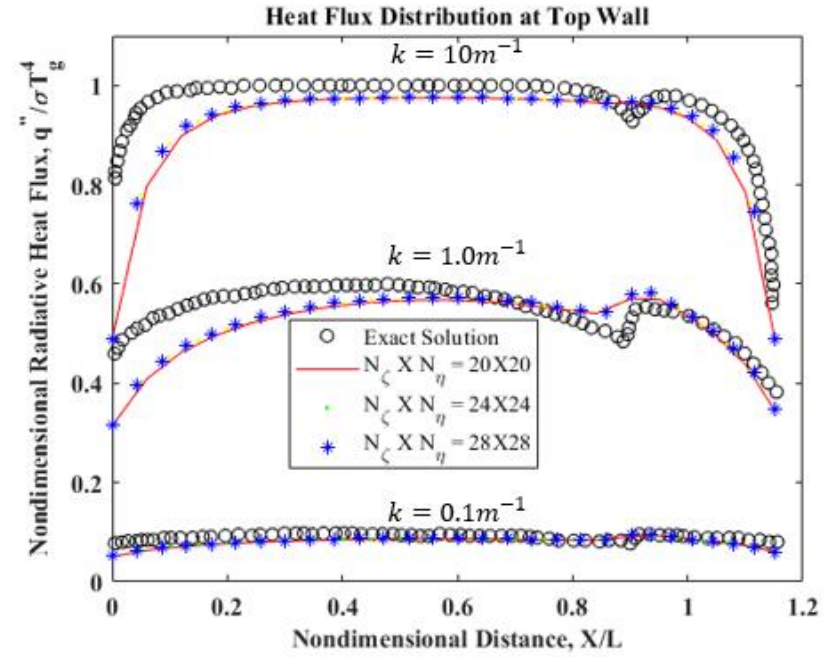

(a) $N_\varphi \times N_\psi = 24 \times 48$

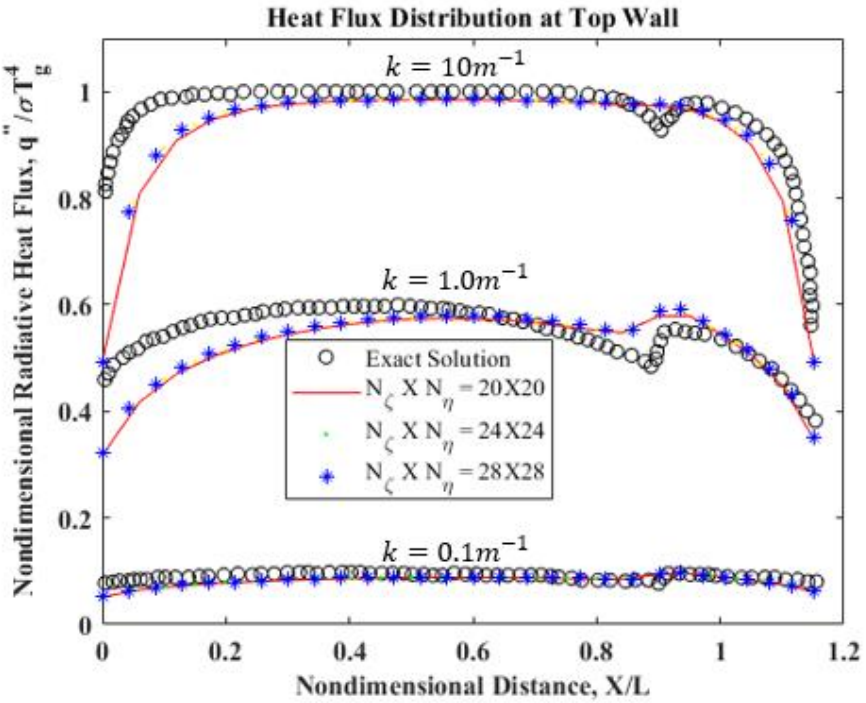

(b) $N_\varphi \times N_\psi = 36 \times 72$

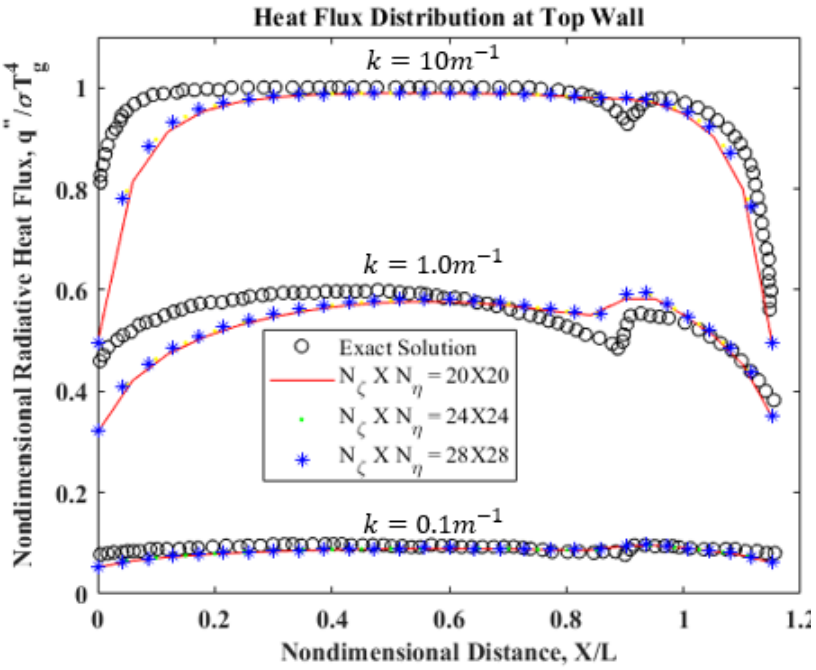

(c) $N_\varphi \times N_\psi = 48 \times 96$

Fig. 25: Grid independence test for dimensionless heat flux at the top wall in a trapezoidal enclosure for constant angular grids, (a) $N_\varphi \times N_\psi = 24 \times 48$, (b) $N_\varphi \times N_\psi = 36 \times 72$, and (c) $N_\varphi \times N_\psi = 48 \times 96$ with varying discrete spatial grids.

0.0130 of $N_\xi \times N_\eta = 20 \times 20$ with $N_\varphi \times N_\psi = 24 \times 48$ for the absorption coefficient of $k = 10m^{-1}$ and the minimum RMSE error is 0.0021 of $N_\xi \times N_\eta = 28 \times 28$ with $N_\varphi \times N_\psi = 48 \times 96$ for the absorption coefficient of $k = 0.1m^{-1}$.

Table 9: Grid independence based on root-mean-square error (RMSE) and mean absolute percentage error (MAPE) calculations for constant angular grids with varying spatial grids at the top wall in a quadrilateral enclosure.

Spatial Grids $(\mathbf{N_\xi \times N_\eta})$	**Absorption coefficients k, m^{-1}**	**Angular Grids** $(\mathbf{N_\varphi \times N_\psi})$					
		24×48		36×72		48×96	
		RMSE	MAPE, %	RMSE	MAPE, %	RMSE	MAPE, %
20×20	0.1	0.0025	7.35	0.0023	6.85	0.0022	6.63
	1.0	0.0121	8.29	0.0114	7.56	0.0111	7.31
	10.0	0.0130	5.18	0.0114	4.29	0.0108	3.95
24×24	0.1	0.0022	7.25	0.0021	6.78	0.0020	6.53
	1.0	0.0105	7.73	0.0099	7.10	0.0097	6.85
	10.0	0.0117	5.04	0.0103	4.14	0.0098	3.79
28×28	0.1	0.0021	7.21	0.0019	6.72	0.0019	6.49
	1.0	0.0095	7.45	0.0090	6.81	0.0088	6.61
	10.0	0.0107	4.92	0.0094	4.00	0.0089	3.64

Compared to the top and bottom walls, the top wall shows a larger error than the bottom wall. The discrete ordinate method has two main drawbacks of numerical solutions of RTE. The first one is false scattering which has happened due to the problem of the spatial grid,

and the second one is the ray effect which has occurred due to the angular grids issues. The false scattering can be eliminated by increasing the spatial grids. In contrast, the ray effect also can be eliminated by increasing the volume of the spatial grids. So numerical solutions must choose the right spatial grids with angular grids.

Validation:

Fig. 26 shows the grid generations for $N_\xi \times N_\eta = 20 \times 20$ spatial grids in the computational domain. This problem is solved for a non-scattering homogeneous medium. The medium is maintained at a constant temperature of 1000K. The problem is also solved with $N_\varphi \times N_\psi = 24 \times 48$ anguar grids. The dimensionless radiative heat fluxes at the bottom and top walls are plotted in Fig. 27 (a) and (b) for three values of absorption coefficients, namely, $k = 0.1m^{-1}$, $k = 1m^{-1}$, and $k = 10m^{-1}$ respectively and are compared with the exact solutions. By comparison, it can be shown that the present solutions have good accuracy and excellent stability in solving the radiative heat transfer in complex geometries. Based on the exact solution, the maximum RMSE and MAPE are less than 0.0130 and 8.29%.

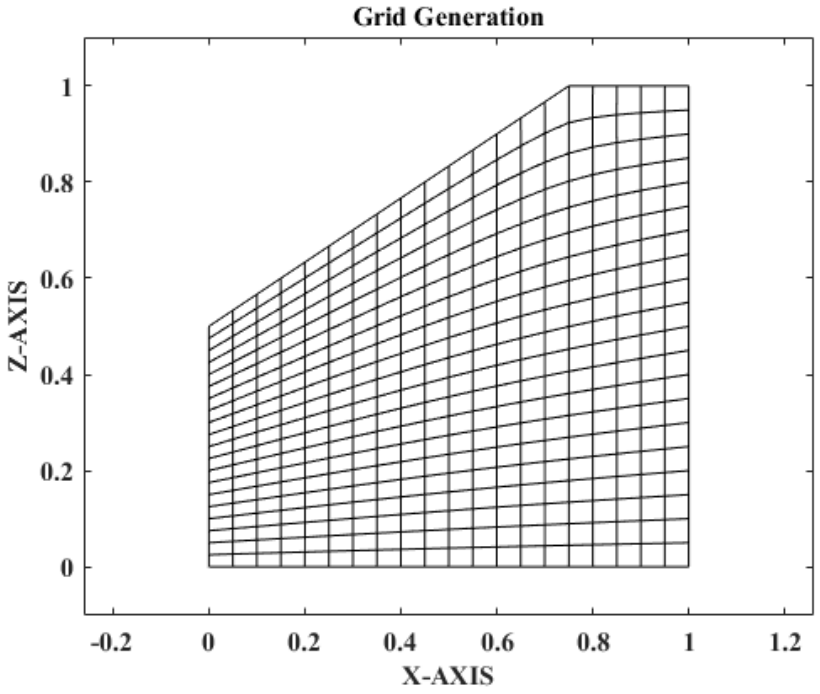

Fig. 26: Grid generation for a trapezoidal enclosure.

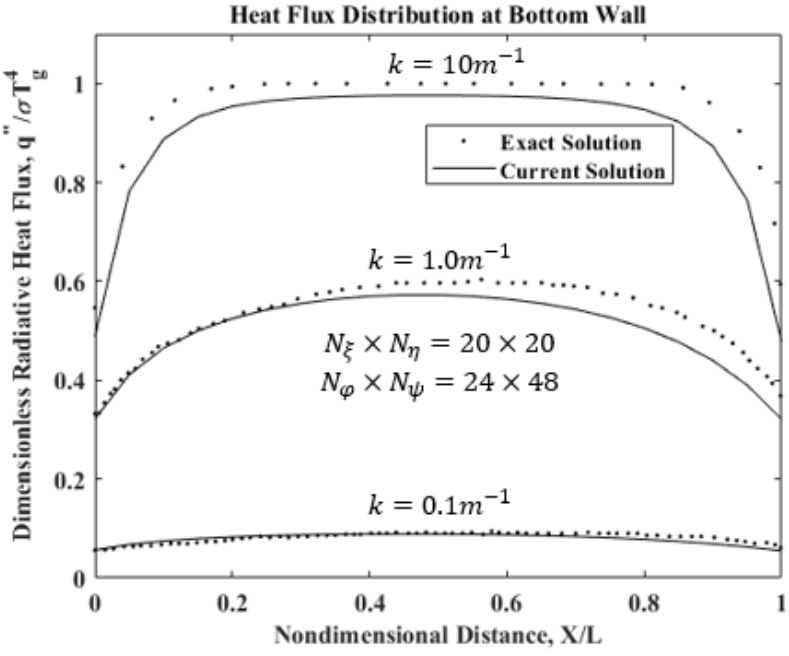

(a)

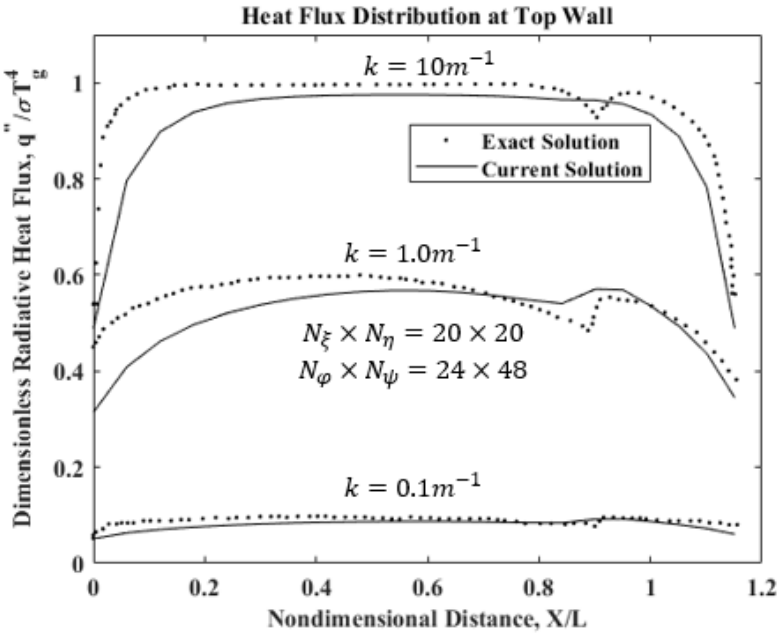

(b)

Fig. 27: Dimensionless radiative heat flux along (a) the bottom wall; (b) the top wall of a trapezoidal enclosure.

Parametric studies:

Six types of quadrilateral enclosures, trapezoid to the rectangle, are investigated to check the effect of geometry skewness of trapezoidal enclosure by changing the length of a and b with constant enclosure area non-scattering homogenous medium. These geometries present with the same area by changing the length difference of b and a, containing 0.5 to 0.0. The trapezoidal enclosure of Fig. 28 (a) has already discussed in section 5.2.3 for non-scattering homogenous media. We are assumed the computational domain of 1m. This problem is conducted to an isothermal medium temperature at 1000K, and all

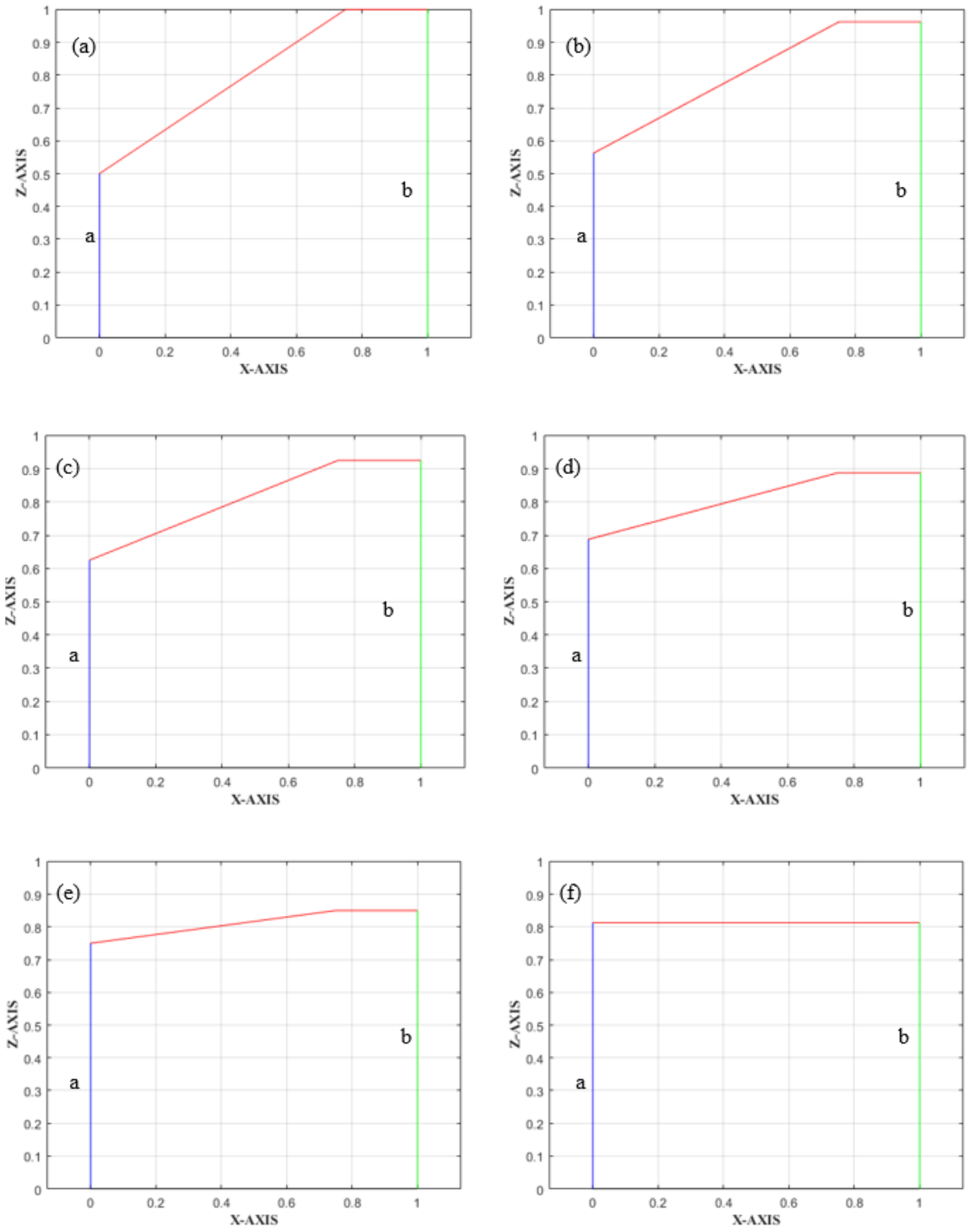

Fig. 28: Geometries configuration of quadrilateral enclosures for (a) b-a = 0.5; (b) b-a = 0.4; (c) b-a = 0.3; (d) b-a = 0.2; (e) b-a = 0.1; and (f) b-a = 0.0.

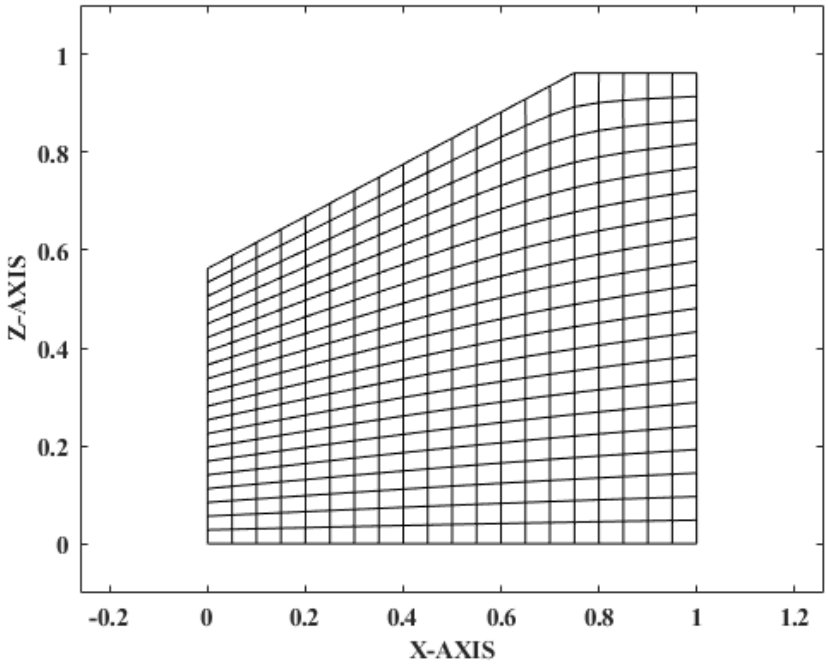

Fig. 29: Grid generations for trapezoidal (b-a = 0.4) enclosure.

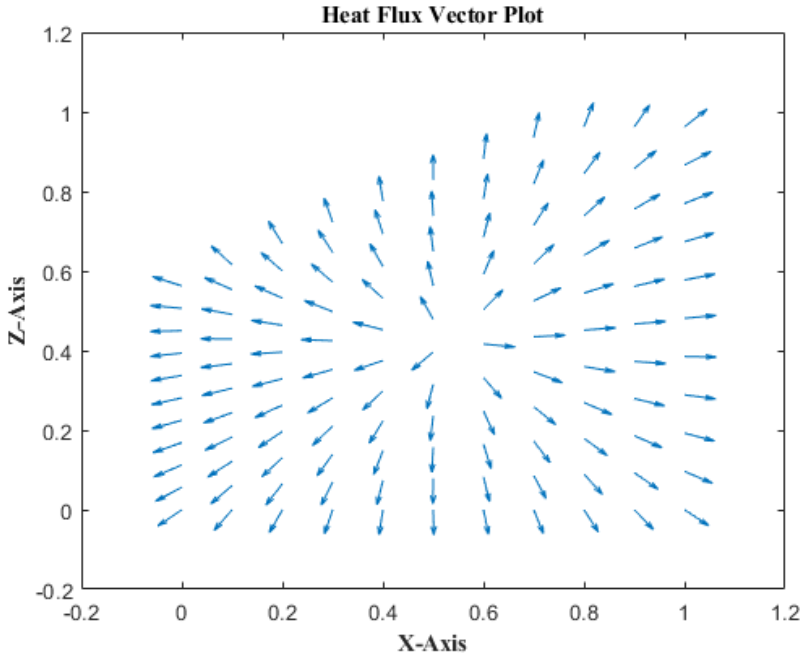

Fig. 30: Heat flux vector plot for trapezoidal (b-a = 0.4) enclosure for the absorption coefficient of $k = 0.1m^{-1}$.

.

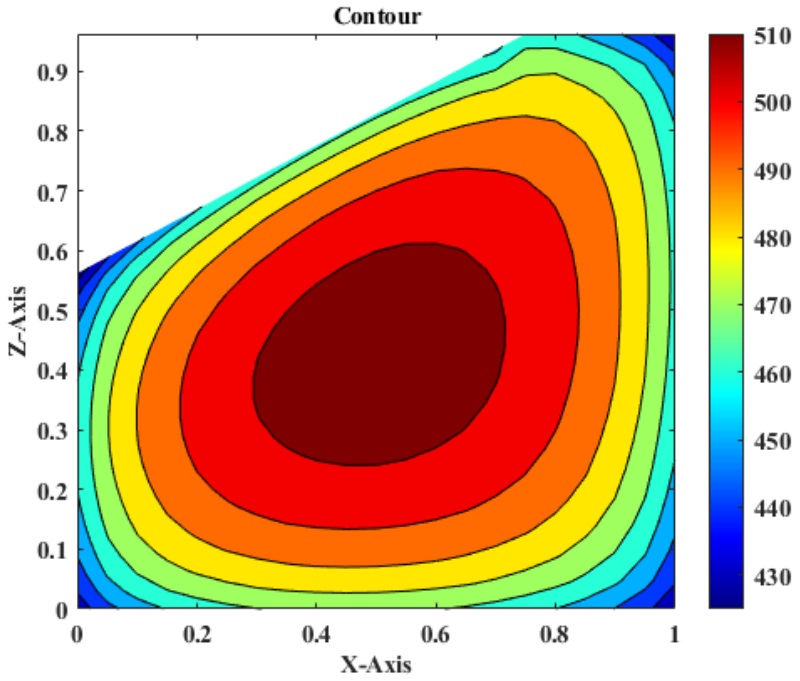

Fig. 31: Temperature contour for trapezoidal (b-a = 0.4) enclosure for the absorption coefficient of $k = 0.1m^{-1}$.

boundary walls' temperature is maintained at 0K. The boundary walls are also assumed black. Three different absorption coefficients are considered to solve this problem and are validated with the exact solutions. Fig. 29 shows the grid generation for trapezoidal (b-a = 0.4) enclosure. Here $N_\xi \times N_\eta = 20 \times 20$ spatial grids are considered.

Fig. 30 and Fig. 31 depict the heat flux vector plot and temperature contour for the trapezoidal (b-a = 0.4) enclosure for the absorption coefficient of $k = 0.1m^{-1}$. Fig. 32

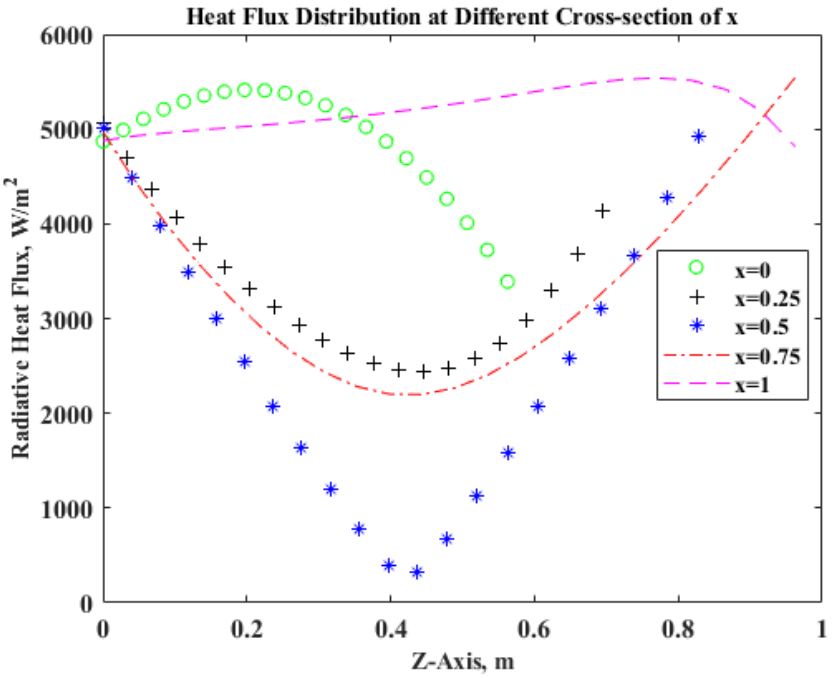

(a) $k = 0.1m^{-1}$

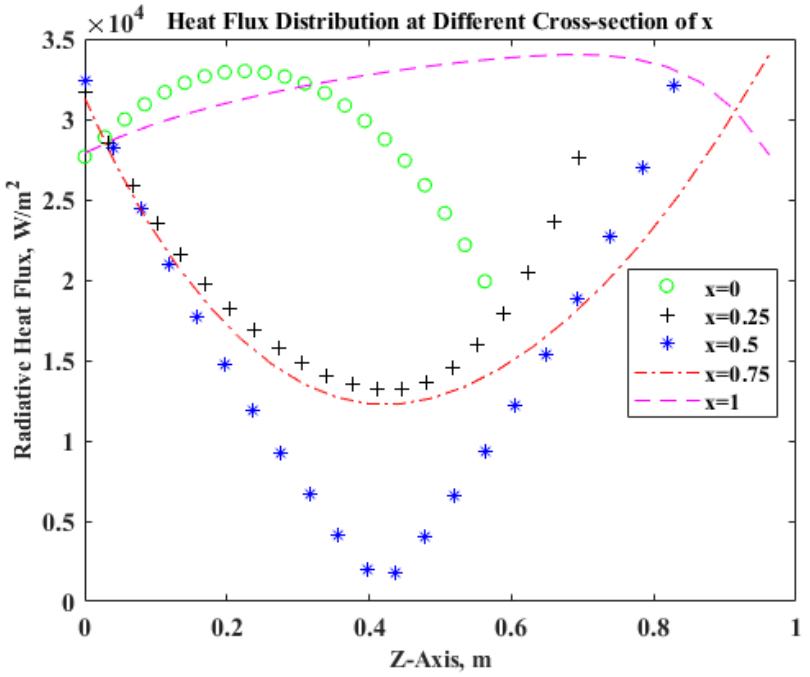

(b) $k = 1m^{-1}$

Fig. 32: Radiative heat flux distribution of trapezoidal (b-a = 0.4m) enclosure for the absorption coefficient of (a) $k = 0.1m^{-1}$ and (b) $k = 1m^{-1}$ at the different cross-sections of the x-axis.

depicts the radiative heat flux distribution of trapezoidal (b-a = 0.4m) enclosure for the absorption coefficient of (a) $k = 0.1m^{-1}$ and (b) $k = 1m^{-1}$ at the different cross-sections of the x-axis, namely at x=0, x=0.25m, x=0.5m, x=0.75m, and x=1.0m. the figure shows that the radiative heat fluxes are maximum at the enclosure's left (x=0m) and right (x=1m) walls. The radiative heat flux is minimum for x=0.5m when z=0.4374m of the enclosure is almost zero. This is because of heat generation inside the enclosure.

Fig. 33 demonstrates the dimensionless heat flux along the bottom wall of the modified six quadrilateral enclosures for the absorption coefficient of $k = 0.1m^{-1}$; $k = 1m^{-1}$; and $k = 10m^{-1}$. As shown in Fig. 33 (a), radiative heat flow patterns on the bottom wall are greatly influenced by the absorption coefficient. As long as the absorption coefficient is less than $k = 0.1m^{-1}$, the radiative heat flow on the bottom wall is strongly dependent on surface temperature; when the wall temperatures are equal to zero, the radiative heat flux is feeble. In contrast, the radiative heat flux on the bottom wall of an optically thick media is mainly controlled by the medium temperature: if the medium temperature is T_g, the radiative heat flux will be close to σT_g^4. The heat flux distribution of the bottom wall (same length for every enclosure) is slightly changing with the change in the quadrilateral enclosure shape (Fig. 33). This is because of the grid generations. We may neglect this small effect of changing a similar geometry configuration with the same area.

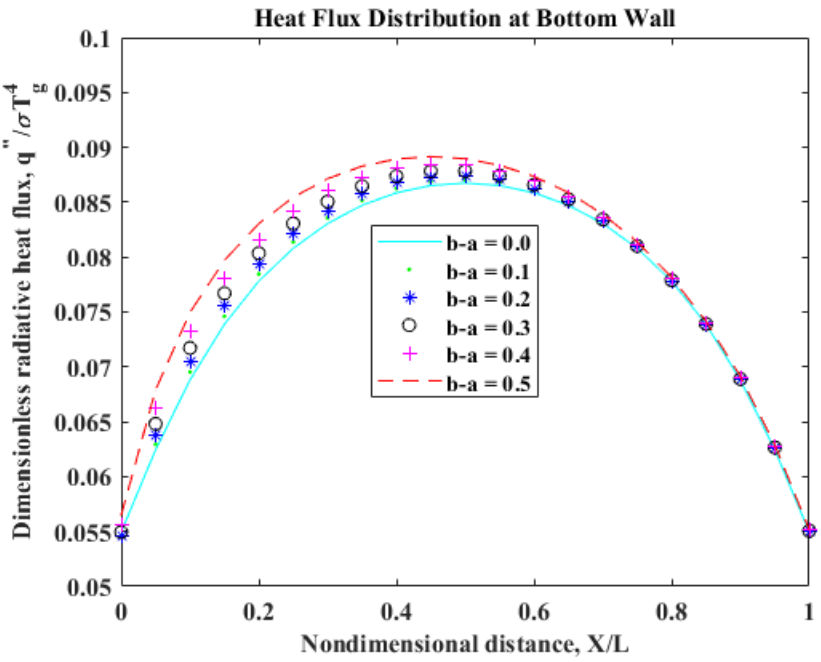

(a) $k = 0.1m^{-1}$

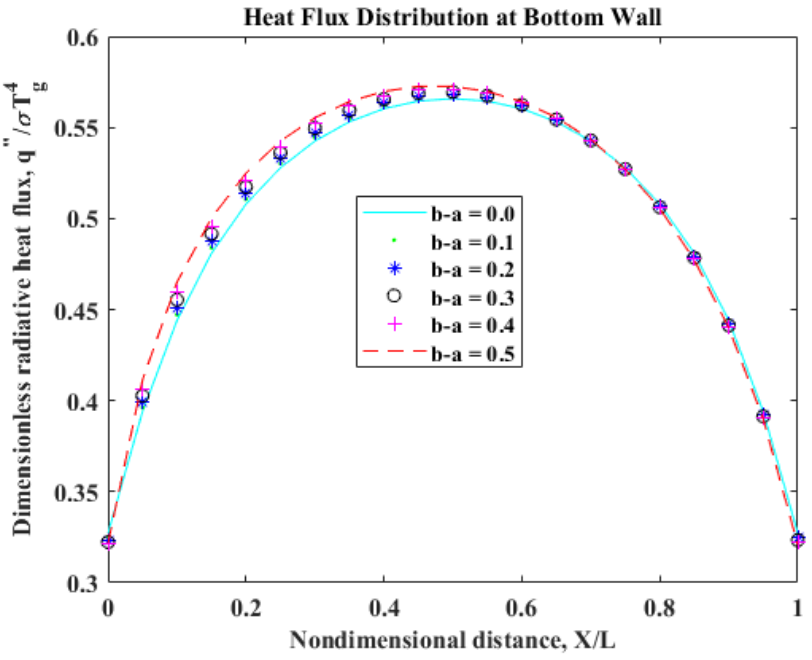

(b) $k = 1m^{-1}$

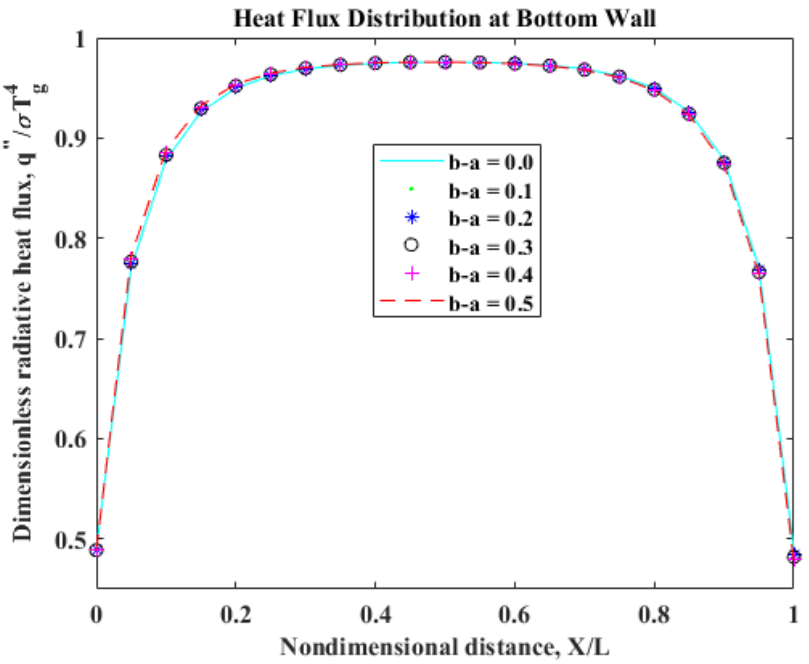

(c) $k = 10m^{-1}$

Fig. 33: Dimensionless heat flux along the bottom wall of the modified trapezoidal enclosures for (a) $k = 0.1m^{-1}$; (b) $k = 1m^{-1}$; and (c) $k = 10m^{-1}$.

On the other hand, Fig. 34 illustrates the dimensionless heat flux along the top wall of the modified six quadrilateral enclosures for the absorption coefficient of $k = 0.1m^{-1}$; $k = 1m^{-1}$; and $k = 10m^{-1}$. The dimensionless heat fluxes remain constant until 0.8 on the z-axis. Then, as the geometrical configurations change, the heat flow distributions also change. When the difference between two lines (a and b) equals zero, dimensionless heat flux distributions behave similarly to the bottom wall. Increases in the heat flow distributions occur when the difference between b and a is increased. The figures (a), (b), and (c) demonstrate that for each absorption coefficient, the heat flux distribution varies for each enclosure due to the top wall's length varying from 1.1416 to 1.0.

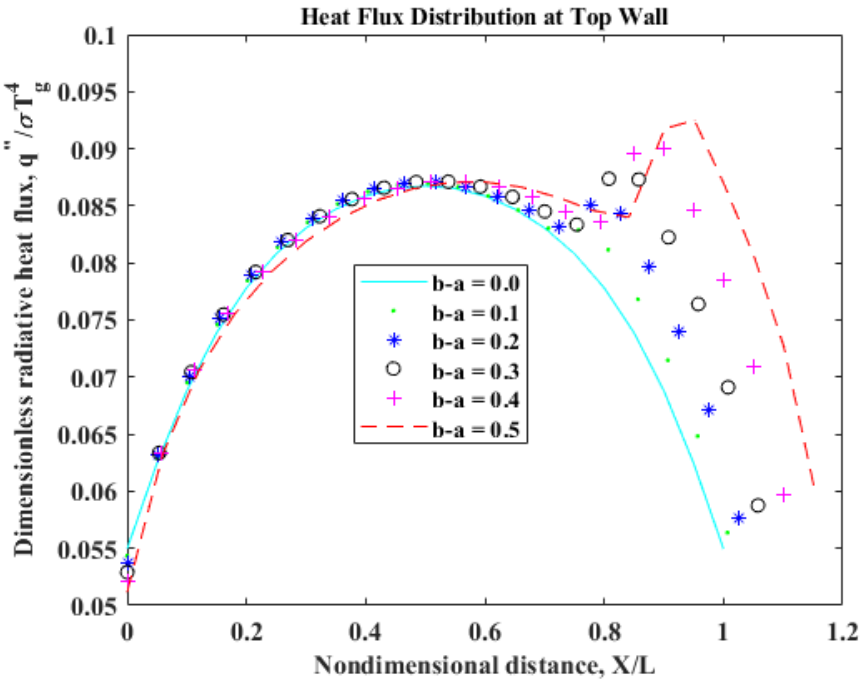

(a) $k = 0.1m^{-1}$

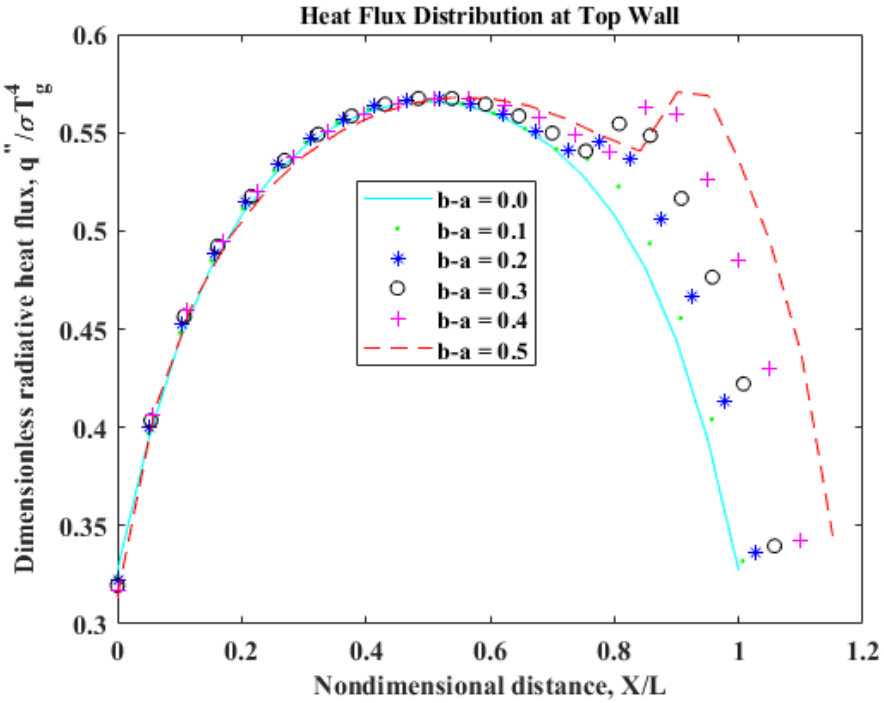

(b) $k = 1m^{-1}$

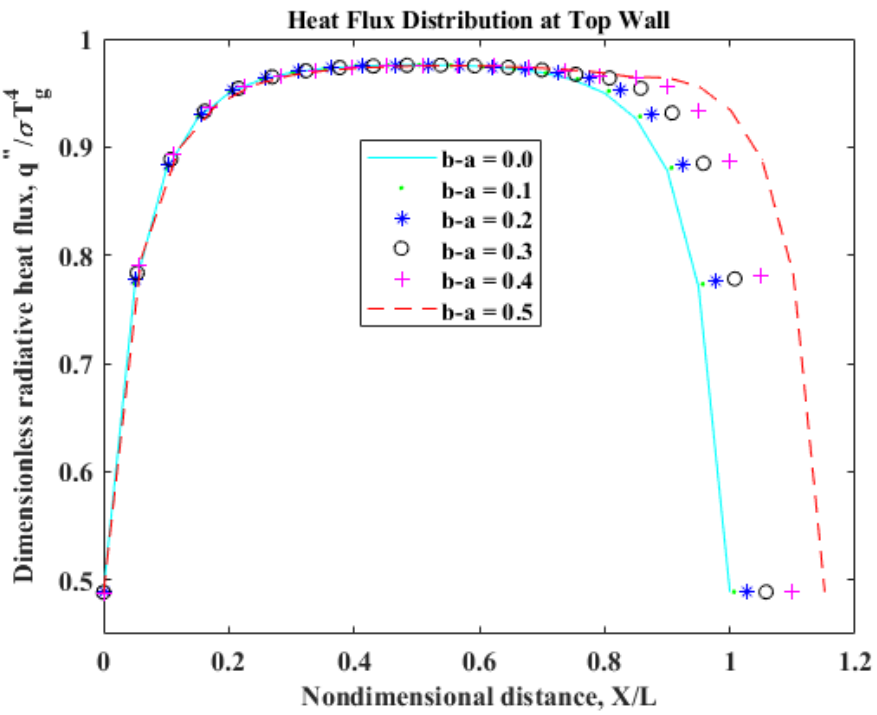

(c) $k = 10m^{-1}$

Fig. 34: Dimensionless heat flux along the top wall of the modified trapezoidal enclosures for (a) $k = 0.1m^{-1}$; (b) $k = 1m^{-1}$; and (c) $k = 10m^{-1}$.

CHAPTER 6

CONCLUSIONS

The radiative transfer equation (RTE) is solved in 2D complex geometries using body-fitted coordinates with absorption, emitting, and isotropic scattering media. Three types of geometries are considered for solving the radiative heat flux of the walls. RTE is derived from an orthogonal curvilinear coordinate system, transforms the equation into a body-fitted coordinate, and solves the problem using the discrete ordinate method. This thesis is considered different absorption and extinction coefficients with radiative and non-radiative equilibriums conditions. This thesis is also investigated grid independence based on the root-mean-square error and mean absolute percentage error calculations. The results are validated with the published literature and showed an excellent agreement with the exact solutions. These comparisons are indicated that the current model has good accuracy and computational simplicity for irregular geometries. The influence of geometric skewness using the rigid body rotation and changing the geometry length with the constant area on square and quadrilateral enclosures of participating media is also demonstrated in this thesis.

This research is very fundamental for solving the RTE for two-dimensional geometries problems. This study can be extended by following…

a) Solving the RTE for a three-dimensional orthogonal curvilinear system.
b) Solving the transient RTE for both two and three-dimensional orthogonal curvilinear systems.
c) Solving the RTE for a non-orthogonal coordinate system.
d) Can be extended with an anisotropic scattering problem.
e) Can be extended by solving the energy equations of conduction-radiation, convection-radiation, and conduction-convection-radiation problems.
f) This study can also be applied to the practical fields of non-invasive biomedical image models, solar energy collection, target detection, astrophysics, combustion, etc.

References

[1] Modest, M. F., 2013, *Radiative Heat Transfer*, Elsevier.

[2] Howell, J. R., Menguc, M. P., and Siegel, R., 2015, *Thermal Radiation Heat Transfer*, CRC Press.

[3] Simmons, F., 2000, *Rocket Exhaust Plume Phenomenology*, American Institute of Aeronautics and Astronautics, Inc., Washington, DC.

[4] Yung, Y. L., 2003, "An Introduction to Atmospheric Radiation. By K. N. Liou. Academic Press. Second Edition, 2002. Pp. Xiv+583. ISBN 0 12 451451 0," Q. J. R. Meteorol. Soc., 129(590), pp. 1741–1741.

[5] Chen, Q., Yam, J. W., Chua, S. Y., Guo, N., and Wang, X., 2020, "Characterizing the Performance Impacts of Target Surface on Underwater Pulse Laser Ranging System," J. Quant. Spectrosc. Radiat. Transf., 255, p. 107267.

[6] Axelsson, M., Friman, O., Haavardsholm, T. V., and Renhorn, I., 2016, "Target Detection in Hyperspectral Imagery Using Forward Modeling and In-Scene Information," ISPRS J. Photogramm. Remote Sens., 119, pp. 124–134.

[7] Viskanta, R., and Mengüç, M. P., 1987, "Radiation Heat Transfer in Combustion Systems," Prog. Energy Combust. Sci., 13(2), pp. 97–160.

[8] Modest, M. F., and Haworth, D. C., 2016, "Radiative Heat Transfer in High-Pressure Combustion Systems," *SpringerBriefs in Applied Sciences and Technology*, pp. 137–148.

[9] Steffen, W., and Koning, N., 2017, “Hybrid Polygon and Hydrodynamic Nebula Modeling with Multi-Waveband Radiation Transfer in Astrophysics,” Astron. Comput., 20, pp. 87–96.

[10] Steinacker, J., Baes, M., and Gordon, K. D., 2013, “Three-Dimensional Dust Radiative Transfer,” Annu. Rev. Astron. Astrophys., 51, pp. 63–104.

[11] Saratoon, T., Tarvainen, T., Cox, B. T., and Arridge, S. R., 2013, “A Gradient-Based Method for Quantitative Photoacoustic Tomography Using the Radiative Transfer Equation,” Inverse Probl., 29(7), p. 075006.

[12] Charette, A., Boulanger, J., and Kim, H. K., 2008, “An Overview on Recent Radiation Transport Algorithm Development for Optical Tomography Imaging,” J. Quant. Spectrosc. Radiat. Transf., 109(17–18), pp. 2743–2766.

[13] Tarvainen, T., Vauhkonen, M., and Arridge, S. R., 2008, “Gauss–Newton Reconstruction Method for Optical Tomography Using the Finite Element Solution of the Radiative Transfer Equation,” J. Quant. Spectrosc. Radiat. Transf., 109(17–18), pp. 2767–2778.

[14] Hänninen, N., Pulkkinen, A., Leino, A., and Tarvainen, T., 2020, “Application of Diffusion Approximation in Quantitative Photoacoustic Tomography in the Presence of Low-Scattering Regions,” J. Quant. Spectrosc. Radiat. Transf., 250, p. 107065.

[15] He, M. J., Qi, H., Ren, Y. T., Zhao, Y. J., and Antezza, M., 2020, "Magnetoplasmonic Manipulation of Nanoscale Thermal Radiation Using Twisted Graphene Gratings," Int. J. Heat Mass Transf., 150, p. 119305.

[16] Ren, Y., Qi, H., Chen, Q., and Ruan, L., 2017, "Thermal Dosage Investigation for Optimal Temperature Distribution in Gold Nanoparticle Enhanced Photothermal Therapy," Int. J. Heat Mass Transf., 106, pp. 212–221.

[17] Videen, G., Sun, W., and Gong, W., 2017, "Advances in Atmospheric Light Scattering Theory and Remote-Sensing Techniques," J. Quant. Spectrosc. Radiat. Transf., 188, pp. 1–2.

[18] Xu, P., Liu, D., Shen, Y., Chen, Y., Zhang, H., Ye, Z., Jiang, C., Zhou, Y., Liu, Q., and Liu, C., 2020, "Design and Validation of a Shipborne Multiple-Field-of-View Lidar for Upper Ocean Remote Sensing," J. Quant. Spectrosc. Radiat. Transf., 254, p. 107201.

[19] Al-Abbas, A. H., Naser, J., and Dodds, D., 2012, "CFD Modelling of Air-Fired and Oxy-Fuel Combustion in a Large-Scale Furnace at Loy Yang A Brown Coal Power Station," Fuel, 102, pp. 646–665.

[20] Vassiliev, O. N., Wareing, T. A., Davis, I. M., McGhee, J., Barnett, D., Horton, J. L., Gifford, K., Failla, G., Titt, U., and Mourtada, F., 2008, "Feasibility of a Multigroup Deterministic Solution Method for Three-Dimensional Radiotherapy Dose Calculations," Int. J. Radiat. Oncol., 72(1), pp. 220–227.

[21] Ispir, E. B., Sarigul, N., and Yegingil, Z., 2021, "NanoDot^{TM} OSLDs in Verifying

Radiotherapy Dose Calculations in the Presence of Metal Implants: A Monte Carlo Assisted Research," Radiat. Phys. Chem., 187, p. 109577.

[22] Pilon, L., Berberoğlu, H., and Kandilian, R., 2011, "Radiation Transfer in Photobiological Carbon Dioxide Fixation and Fuel Production by Microalgae," J. Quant. Spectrosc. Radiat. Transf., 112(17), pp. 2639–2660.

[23] Duderstadt, J. J., Martin, W. R., and Aronson, R., 2008, "Transport Theory," Phys. Today, 35(4), p. 65.

[24] Akbarzadeh, S., and Valipour, M. S., 2018, "Heat Transfer Enhancement in Parabolic Trough Collectors: A Comprehensive Review," Renew. Sustain. Energy Rev., 92, pp. 198–218.

[25] Ho, C. K., and Iverson, B. D., 2014, "Review of High-Temperature Central Receiver Designs for Concentrating Solar Power," Renew. Sustain. Energy Rev., 29, pp. 835–846.

[26] Wang, K., He, Y., Liu, P., Kan, A., Zheng, Z., Wang, L., Xie, H., and Yu, W., 2020, "Highly-Efficient Nanofluid-Based Direct Absorption Solar Collector Enhanced by Reverse-Irradiation for Medium Temperature Applications," Renew. Energy, 159, pp. 652–662.

[27] Zhao, J. M., and Liu, L. H., 2007, "Second-Order Radiative Transfer Equation and Its Properties of Numerical Solution Using the Finite-Element Method," Numer. Heat Transf. Part B Fundam., 51(4), pp. 391–409.

[28] Kang, S., and Song, T.-H., 2008, “Finite Element Formulation of the First- and Second-Order Discrete Ordinates Equations for Radiative Heat Transfer Calculation in Three-Dimensional Participating Media,” J. Quant. Spectrosc. Radiat. Transf., 109, pp. 2094–2107.

[29] Zhao, J., Tan, J., and Liu, L. H., 2013, “A Second Order Radiative Transfer Equation and Its Solution by Meshless Method with Application to Strongly Inhomogeneous Media,” J. Comput. Phys., 232, pp. 431–455.

[30] Liu, L. H., and Tan, J. Y., 2007, “Least-Squares Collocation Meshless Approach for Radiative Heat Transfer in Absorbing and Scattering Media,” J. Quant. Spectrosc. Radiat. Transf., 103(3), pp. 545–557.

[31] Asllanaj, F., and Fumeron, S., 2010, “Modified Finite Volume Method Applied to Radiative Transfer in 2D Complex Geometries and Graded Index Media,” J. Quant. Spectrosc. Radiat. Transf., 111(2), pp. 274–279.

[32] Wu, C. Y., and Hou, M. F., 2012, “Solution of Integral Equations of Intensity Moments for Radiative Transfer in an Anisotropically Scattering Medium with a Linear Refractive Index,” Int. J. Heat Mass Transf., 55(7–8), pp. 1863–1872.

[33] Wei, L. Y., Qi, H., Niu, Z. T., Ren, Y. T., and Ruan, L. M., 2019, “Reverse Monte Carlo Coupled with Runge-Kutta Ray Tracing Method for Radiative Heat Transfer in Graded-Index Media,” Infrared Phys. Technol., 99, pp. 5–13.

[34] Moghadassian, B., Jafari, M., Hafezisefat, P., Mirhosseini, M., and Rezania, A., 2019, "Numerical Investigation of Radiative Heat Transfer inside a 2-D Irregular Geometry Containing Nano- and Micro-Size Particles," *Energy Procedia*, Elsevier Ltd, pp. 5685–5691.

[35] Moghadassian, B., Jafari, M., Hafezisefat, P., Mirhosseini, M., and Rezania, A., 2019, "Numerical Investigation of Radiative Heat Transfer in a Particulate Medium Using FTN Finite Volume Method," *Energy Procedia*, Elsevier Ltd, pp. 5692–5698.

[36] Favre, F., Antepara, O., Oliet, C., Lehmkuhl, O., and Perez-Segarra, C. D., 2019, "An Immersed Boundary Method to Conjugate Heat Transfer Problems in Complex Geometries. Application to an Automotive Antenna," Appl. Therm. Eng., 148, pp. 907–928.

[37] Thompson, J. F., Warsi, Z. U. A., and Wayne Mastin, C., 1982, "Boundary-Fitted Coordinate Systems for Numerical Solution of Partial Differential Equations-A Review," J. Comput. Phys., 47(1), pp. 1–108.

[38] Thompson, J., Warsi, Z. U. A., and Mastin, C., 1985, "Numerical Grid Generation: Foundations and Applications," undefined.

[39] Ryskin, G., and Leal, L. G., 1983, "Orthogonal Mapping," J. Comput. Phys., 50(1), pp. 71–100.

[40] Allievi, A., and Calisal, S. M., 1992, "Application of Bubnov-Galerkin Formulation to Orthogonal Grid Generation," J. Comput. Phys., 98(1), pp. 163–173.

[41] Tamamidis, P., and Assanis, D. N., 1991, “Generation of Orthogonal Grids with Control of Spacing,” J. Comput. Phys., 94(2), pp. 437–453.

[42] Bourchtein, A., and Bourchtein, L., 2006, “On Generation of Orthogonal Grids,” Appl. Math. Comput., 173(2), pp. 767–781.

[43] Wu, N. J., Tsay, T. K., Yang, T. C., and Chang, H. Y., 2013, “Orthogonal Grid Generation of an Irregular Region Using a Local Polynomial Collocation Method,” J. Comput. Phys., 243, pp. 58–73.

[44] Christiana Honsberg, and and Stuart Bowden, “Absorption Coefficient ,” PV Educ. [Online]. Available: https://www.pveducation.org/pvcdrom/pn-junctions/absorption-coefficient. [Accessed: 30-Oct-2021].

[45] Zhou, H.-C., Chen, D.-L., and Cheng, Q., 2004, “A New Way to Calculate Radiative Intensity and Solve Radiative Transfer Equation through Using the Monte Carlo Method,” J. Quant. Spectrosc. Radiat. Transf., 83(3–4), pp. 459–481.

[46] Li, G. J., Zhong, J. Q., and Wang, X. D., 2020, “An Improved Monte Carlo Method for Radiative Heat Transfer in Participating Media,” J. Quant. Spectrosc. Radiat. Transf., 251, p. 107081.

[47] Torres-Monclard, K., Gicquel, O., and Vicquelin, R., 2021, “A Quasi-Monte Carlo Method to Compute Scattering Effects in Radiative Heat Transfer: Application to a Sooted Jet Flame,” Int. J. Heat Mass Transf., 168, p. 120915.

[48] Cheng, Y., Li, H., Zhang, J., and Huang, Z., 2020, “Solution of Radiative Intensity with High Directional Resolution in Heterogeneous Participating Media and Irregular Geometries by the Null-Collision Reverse Monte Carlo Method,” Int. J. Heat Mass Transf., 152, p. 119475.

[49] Zhou, H., and Cheng, Q., 2004, “THE DRESOR METHOD FOR THE SOLUTION OF THE RADIATIVE TRANSFER EQUATION IN GRAY PLANE-PARALLEL MEDIA,” *Proceeding of the 4th International Symposium on Radiative Transfer*, Begellhouse, New York, pp. 1–10.

[50] Wang, G., Zhou, H., Cheng, Q., Wang, Z., and Huang, Z., 2012, “Equation-Solving DRESOR Method for Radiative Transfer in a Plane-Parallel, Absorbing, Emitting, and Isotropically Scattering Medium with Transparent Boundaries,” Int. J. Heat Mass Transf., 55(13–14), pp. 3454–3457.

[51] Fiveland, W. A., and Jamaluddin, A. S., 1991, “Three-Dimensional Spectral Radiative Heat Transfer Solutions by the Discrete-Ordinates Method,” J. Thermophys. Heat Transf., 5(3), pp. 335–339.

[52] Kumar, S., Majumdar, A., and Tien, C. L., 1990, “The Differential-Discrete-Ordinate Method for Solutions of the Equation of Radiative Transfer,” J. Heat Transfer.

[53] Modest, M. F., 2003, “THE METHOD OF DISCRETE ORDINATES (SN-APPROXIMATION),” *Radiative Heat Transfer*.

[54] Liu, L. H., Ruan, L. M., and Tan, H. P., 2002, “On the Discrete Ordinates Method for Radiative Heat Transfer in Anisotropically Scattering Media,” Int. J. Heat Mass Transf., 45(15), pp. 3259–3262.

[55] Thomson, D. L., Meade, A. J., and Bayazitoglu, Y., 2001, “Solution of the Radiative Transfer Equation in Discrete Ordinate Form by Sequential Function Approximation,” Int. J. Therm. Sci., 40(6), pp. 517–527.

[56] Asllanaj, F., Contassot-Vivier, S., Botella, O., and França, F. H. R., 2021, “Numerical Solutions of Radiative Heat Transfer in Combustion Systems Using a Parallel Modified Discrete Ordinates Method and Several Recent Formulations of WSGG Model,” J. Quant. Spectrosc. Radiat. Transf., 274, p. 107863.

[57] Coelho, P. J., 2020, “Discrete Ordinates Solution of the Radiative Transfer Equation in Media with Strong Forward and Backward Scattering Subjected to Collimated Irradiation,” J. Quant. Spectrosc. Radiat. Transf., 254, p. 107087.

[58] Le Hardy, D., Favennec, Y., Rousseau, B., and Hecht, F., 2017, “Specular Reflection Treatment for the 3D Radiative Transfer Equation Solved with the Discrete Ordinates Method,” J. Comput. Phys., 334, pp. 541–572.

[59] Mengüç, M. P., and Viskanta, R., 1985, “Radiative Transfer in Three-Dimensional Rectangular Enclosures Containing Inhomogeneous, Anisotropically Scattering Media,” J. Quant. Spectrosc. Radiat. Transf., 33, pp. 533–549.

[60] Larsen, E., Thömmes, G., Klar, A., Seaid, M., and Goetz, T., 2002, “Simplified PN Approximations to the Equations of Radiative Heat Transfer and Applications,” J. Comput. Phys., 183, pp. 652–675.

[61] Xu, X., Jiang, S., and Sun, W., 2021, “A Positive and Asymptotic Preserving Filtered PN Method for the Gray Radiative Transfer Equations,” J. Comput. Phys., 444, p. 110546.

[62] Garcia, R. D. M., 2017, “A PN Particular Solution for the Radiative Transfer Equation in Spherical Geometry,” J. Quant. Spectrosc. Radiat. Transf., 196, pp. 155–158.

[63] An, W., Ruan, L. M., Qi, H., and Liu, L. H., 2005, “Finite Element Method for Radiative Heat Transfer in Absorbing and Anisotropic Scattering Media,” J. Quant. Spectrosc. Radiat. Transf.

[64] Salah, M. Ben, Askri, F., Rousse, D., and Ben Nasrallah, S., 2005, “Control Volume Finite Element Method for Radiation,” J. Quant. Spectrosc. Radiat. Transf., 92(1), pp. 9–30.

[65] Fiveland, W. A., and Jessee, J. P., 1994, “Finite Element Formulation of the Discrete-Ordinates Method for Multidimensional Geometries,” J. Thermophys. Heat Transf.

[66] Xu, X., Sun, W., and Jiang, S., 2020, “An Asymptotic Preserving Angular Finite Element Based Unified Gas Kinetic Scheme for Gray Radiative Transfer Equations,” J. Quant. Spectrosc. Radiat. Transf., 243, p. 106808.

[67] Feng, Y. Y., and Wang, C. H., 2021, “Discontinuous Finite Element Method Applied to Transient Pure and Coupled Radiative Heat Transfer,” Int. Commun. Heat Mass Transf., 122, p. 105156.

[68] Liu, L. H., and Liu, L. J., 2007, “Discontinuous Finite Element Approach for Transient Radiative Transfer Equation,” J. Heat Transfer, 129(8), pp. 1069–1074.

[69] Zhao, J. M., and Liu, L. H., 2008, “Discontinuous Spectral Element Approach for Solving Transient Radiative Transfer Equations,” J. Thermophys. Heat Transf.

[70] Kitzmann, D., Bolte, J., and Patzer, A. B. C., 2016, “Discontinuous Galerkin Finite Element Methods for Radiative Transfer in Spherical Symmetry,” Astron. Astrophys., 595, p. A90.

[71] Chui, E. H., Raithby, G. D., and Hughes, P. M. J., 1992, “Prediction of Radiative Transfer in Cylindrical Enclosures with the Finite Volume Method,” J. Thermophys. Heat Transf.

[72] Talukdar, P., Steven, M., Issendorff, F. V., and Trimis, D., 2005, “Finite Volume Method in 3-D Curvilinear Coordinates with Multiblocking Procedure for Radiative Transport Problems,” Int. J. Heat Mass Transf., 48(21–22), pp. 4657–4666.

[73] Huang, Q., Liu, T., Yang, J., Yao, L., and Gao, L., 2011, “Evaluation of Radiative Transfer Using the Finite Volume Method in Cylindrical Photoreactors,” Chem. Eng. Sci., 66(17), pp. 3930–3940.

[74] Wang, C. A., Shen, T. R., Gao, J. P., and Tan, J. Y., 2019, “Development of RTE Solver for Radiative Transfer in Absorbing-Emitting Medium Using Finite Volume Based CFD Library OpenFOAM,” Int. J. Therm. Sci., 140, pp. 36–42.

[75] Moghadassian, B., Jafari, M., Hafezisefat, P., Mirhosseini, M., and Rezania, A., 2019, “Numerical Investigation of Radiative Heat Transfer in a Particulate Medium Using FTn Finite Volume Method,” Energy Procedia, 158, pp. 5692–5698.

[76] Mohammadi, M., and Gandjalikhan Nassab, S. A., 2021, “Solution of Radiative-Convective Heat Transfer in Irregular Geometries Using Hybrid Lattice Boltzmann-Finite Volume and Immersed Boundary Method,” Int. Commun. Heat Mass Transf., 128, p. 105595.

[77] Zhao, J. M., and Liu, L. H., 2006, “Least-Squares Spectral Element Method for Radiative Heat Transfer in Semitransparent Media,” Numer. Heat Transf. Part B Fundam., 50(5), pp. 473–489.

[78] Li, B.-W., Sun, Y., and Yu, Y., 2008, “Iterative and Direct Chebyshev Collocation Spectral Methods for One-Dimensional Radiative Heat Transfer,” Int. J. Heat Mass Transf., 51, pp. 5887–5894.

[79] Maruyama, S., 1993, “Radiation Heat Transfer between Arbitrary Three-Dimensional Bodies with Specular and Diffuse Surfaces,” Numer. Heat Transf. Part A Appl., 24(2), pp. 181–196.

[80] Sadat, H., 2006, “On the Use of a Meshless Method for Solving Radiative Transfer with the Discrete Ordinates Formulations,” J. Quant. Spectrosc. Radiat. Transf., 101(2), pp. 263–268.

[81] Sun, J., Yi, H. L., Xie, M., and Tan, H. P., 2016, “New Implementation of Local RBF Meshless Scheme for Radiative Heat Transfer in Participating Media,” Int. J. Heat Mass Transf., 95, pp. 440–452.

[82] Wang, C. A., Sadat, H., and Dez, V. Le, 2012, “Meshless Method for Solving Multidimensional Radiative Transfer in Graded Index Medium,” Appl. Math. Model., 36(11), pp. 5309–5319.

[83] Liu, H., Zhou, H., Wang, D., and Han, Y., 2020, “Performance Comparison of Two Monte Carlo Ray-Tracing Methods for Calculating Radiative Heat Transfer,” J. Quant. Spectrosc. Radiat. Transf., 256, p. 107305.

[84] Wei, L. Y., Qi, H., Niu, Z. T., Ren, Y. T., and Ruan, L. M., 2019, “Reverse Monte Carlo Coupled with Runge-Kutta Ray Tracing Method for Radiative Heat Transfer in Graded-Index Media,” Infrared Phys. Technol., 99, pp. 5–13.

[85] Asinari, P., Mishra, S. C., and Borchiellini, R., 2010, “A Lattice Boltzmann Formulation for the Analysis of Radiative Heat Transfer Problems in a Participating Medium,” Numer. Heat Transf. Part B Fundam., 57(2), pp. 126–146.

[86] Mishra, S. C., Poonia, H., Vernekar, R. R., and Das, A. K., 2014, “Lattice Boltzmann Method Applied to Radiative Transport Analysis in a Planar Participating Medium,” Heat Transf. Eng., 35(14–15), pp. 1267–1278.

[87] Mishra, S. C., Poonia, H., Das, A. K., Asinari, P., and Borchiellini, R., 2014, "Analysis of Conduction-Radiation Heat Transfer in a 2D Enclosure Using the Lattice Boltzmann Method," Numer. Heat Transf. Part A Appl., 66(6), pp. 669–688.

[88] Chai, J. C., Lee, H. O. S., and Patankar, S. V., 1993, "Ray Effect and False Scattering in the Discrete Ordinates Method," Numer. Heat Transf. Part B Fundam., 24(4), pp. 373–389.

[89] Hunter, B., and Guo, Z., 2015, "Numerical Smearing, Ray Effect, and Angular False Scattering in Radiation Transfer Computation," Int. J. Heat Mass Transf., 81, pp. 63–74.

[90] Chai, J. C., Parthasarathy, G., Lee, H. O. S., and Patankar, S. V., 1995, "Finite Volume Radiative Heat Transfer Procedure for Irregular Geometries," J. Thermophys. Heat Transf., 9(3), pp. 410–415.

[91] Parthasarathy, G., Lee, H. S., Chai, J. C., and Patankar, S. V., 1995, "Monte Carlo Solutions for Radiative Heat Transfer in Irregular Two- Dimensional Geometries," J. Heat Transfer, 117(3), pp. 792–795.

[92] Talukdar, P., 2006, "Radiative Heat Transfer for Irregular Geometries with the Collapsed Dimension Method," Int. J. Therm. Sci., 45(2), pp. 103–109.

[93] Wang, C. A., Sadat, H., Ledez, V., and Lemonnier, D., 2010, "Meshless Method for Solving Radiative Transfer Problems in Complex Two-Dimensional and Three-Dimensional Geometries," Int. J. Therm. Sci., 49(12), pp. 2282–2288.

[94] Amiri, H., Mansouri, S. H., and Safavinejad, A., 2010, “Combined Conductive and Radiative Heat Transfer in an Anisotropic Scattering Participating Medium with Irregular Geometries,” Int. J. Therm. Sci., 49(3), pp. 492–503.

[95] Sun, Y. S., and Li, B. W., 2012, “Prediction of Radiative Heat Transfer in 2D Irregular Geometries Using the Collocation Spectral Method Based on Body-Fitted Coordinates,” J. Quant. Spectrosc. Radiat. Transf., 113(17), pp. 2205–2212.

[96] Zhang, Y., Yi, H. L., and Tan, H. P., 2013, “Natural Element Method for Radiative Heat Transfer in Two-Dimensional Semitransparent Medium,” Int. J. Heat Mass Transf., 56(1–2), pp. 411–423.

[97] Ramamoorthy, B., Cheng, G. C., Koomullil, R. P., and Rahmani, R. K., 2013, “Finite Volume Method for Non-Equilibrium Radiative Heat Transfer,” Int. J. Heat Mass Transf.

[98] Coelho, P. J., 2014, “Advances in the Discrete Ordinates and Finite Volume Methods for the Solution of Radiative Heat Transfer Problems in Participating Media,” J. Quant. Spectrosc. Radiat. Transf., 145, pp. 121–146.

[99] Aghanajafi, C., and Abjadpour, A., 2015, “Discrete Ordinates Method Applied to Radiative Transfer Equation in Complex Geometries Meshed by Structured and Unstructured Grids,” J. Brazilian Soc. Mech. Sci. Eng. 2015 383, 38(3), pp. 1007–1019.

[100] McCulloch, R., and Bindra, H., 2016, “Coupled Radiative and Conjugate Heat Transfer in Participating Media Using Lattice Boltzmann Methods,” Comput. Fluids, 124, pp. 261–269.

[101] Ma, J., Sun, Y., and Li, B., 2017, “Simulation of Combined Conductive, Convective and Radiative Heat Transfer in Moving Irregular Porous Fins by Spectral Element Method,” Int. J. Therm. Sci., 118, pp. 475–487.

[102] Sarvari, S. M. H., 2017, “Variable Discrete Ordinates Method for Radiation Transfer in Plane-Parallel Semi-Transparent Media with Variable Refractive Index,” J. Quant. Spectrosc. Radiat. Transf., 199, pp. 36–44.

[103] Badri, M. A., Jolivet, P., Rousseau, B., Le Corre, S., Digonnet, H., Favennec, Y., Badri, M. A., Jolivet, P., Rousseau, B., Le Corre, S., Digonnet, H., and Favennec, Y., 2018, “Vectorial Finite Elements for Solving the Radiative Transfer Equation,” JQSRT, 212, pp. 59–74.

[104] Hong, Y. Bin, and Wu, C. Y., 2018, “Integral Equation Solutions Using Radial Basis Functions for Radiative Heat Transfer in Higher-Dimensional Refractive Media,” Int. J. Heat Mass Transf., 118, pp. 1180–1189.

[105] Wang, C.-H., and Liu, H.-Y., 2018, “Discontinuous Galerkin Finite Element Method for Radiative Heat Transfer in Two-Dimensional Media with Inner Obstacles,” https://doi.org/10.1080/10407782.2018.1460152, 73(11), pp. 806–822.

[106] Amiri, H., and Lari, K., 2018, “Line by Line Benchmark Solutions for Radiative Heat Transfer in 2D Irregular Enclosures with Non-Gray Media,” Int. J. Therm. Sci., 133, pp. 307–319.

[107] Fan, C., Li, X. L., Xia, X. L., and Sun, C., 2019, “An Unstructured Monte Carlo Ray-Tracing Method for Solving Radiative Heat Transfer in 3D Gray Semitransparent Medium,” J. Quant. Spectrosc. Radiat. Transf., 225, pp. 110–118.

[108] Zhou, R.-R., and Li, B.-W., 2019, “The Modified Discrete Ordinates Method for Radiative Heat Transfer in Two-Dimensional Cylindrical Medium,” Int. J. Heat Mass Transf., 139, pp. 1018–1030.

[109] Zhang, M., Cheng, J., and Qiu, J., 2019, “High Order Positivity-Preserving Discontinuous Galerkin Schemes for Radiative Transfer Equations on Triangular Meshes,” J. Comput. Phys., 397, p. 108811.

[110] Clarke, P., Wang, H., Garrard, J., Abedi, R., Mudaliar, S., Clarke, P., Wang, H., Garrard, J., Abedi, R., and Mudaliar, S., 2019, “Space-Angle Discontinuous Galerkin Method for Plane-Parallel Radiative Transfer Equation,” JQSRT, 233, pp. 87–98.

[111] Gaggioli, E. L., Bruno, O. P., and Mitnik, D. M., 2019, “Light Transport with the Equation of Radiative Transfer: The Fourier Continuation – Discrete Ordinates (FC–DOM) Method,” J. Quant. Spectrosc. Radiat. Transf., 236, p. 106589.

[112] Sun, S., Wang, G., and Chen, H., 2020, “Application of Decentralized Fuzzy Inference Method for the Inverse Geometry Design of Radiative Enclosures,” Infrared Phys. Technol., 107, p. 103287.

[113] Djeumegni, J. S., Lazard, M., Dez, V. Le, and Kamdem, H. T. T., 2020, “Radiative Heat Transfer in a 2D Semi-Transparent Gray Medium with a Centered Inner Square Cavity,” Int. J. Heat Mass Transf., 149, p. 119209.

[114] Djeumegni, J. S., Lazard, M., Dez, V. Le, and Kamdem, H. T. T., 2020, “Radiative Heat Transfer in a 2D Semi-Transparent Gray Medium with a Centered Inner Square Cavity,” Int. J. Heat Mass Transf., 149, p. 119209.

[115] Wang, H., Abedi, R., and Mudaliar, S., 2020, “Space-Angle Discontinuous Galerkin Method for Radiative Transfer between Concentric Cylinders,” J. Quant. Spectrosc. Radiat. Transf., 257, p. 107281.

[116] Shao, W., Sheng, Q., and Wang, C., 2020, “A Cascadic Multigrid Asymptotic-Preserving Discrete Ordinate Discontinuous Streamline Diffusion Method for Radiative Transfer Equations with Diffusive Scalings,” Comput. Math. with Appl., 80(6), pp. 1650–1667.

[117] Doicu, A., Mishchenko, M. I., and Trautmann, T., 2020, “Electromagnetic Scattering by Discrete Random Media Illuminated by a Gaussian Beam II: Solution of the Radiative Transfer Equation,” J. Quant. Spectrosc. Radiat. Transf., 256, p. 107297.

[118] Liu, X., Huang, Y., Wang, C. H., and Zhu, K., 2021, “A Multiple-Relaxation-Time Lattice Boltzmann Model for Radiative Transfer Equation,” J. Comput. Phys., 429, p. 110007.

[119] Zhou, R.-R., Sun, Y.-S., Li, B.-W., and Ma, J., 2021, “The Composite Chebyshev Integration Method for Radiative Integral Transfer Equations in Rectangular Enclosures,” Int. J. Therm. Sci., 170, p. 107141.

[120] Jolivet, P., Badri, M. A., and Favennec, Y., 2021, “Deterministic Radiative Transfer Equation Solver on Unstructured Tetrahedral Meshes: Efficient Assembly and Preconditioning,” J. Comput. Phys., 437, p. 110313.

[121] Howell JR, Siegel R, M. M., 2020, “Thermal Radiation Heat Transfer - 7th Edition - John R. Howell - M. P” [Online]. Available: https://www.routledge.com/Thermal-Radiation-Heat-Transfer/Howell-Menguc-Daun-Siegel/p/book/9780367347079. [Accessed: 03-Apr-2021].

[122] Yilbas, B. S., Mansoor, S. Bin, and Ali, H., 2018, “Phonon Radiative Transfer in Curvilinear Coordinate Systems,” *Heat Transport in Micro- and Nanoscale Thin Films*, Elsevier, pp. 377–399.

[123] Akcelik, V., Jaramaz, B., and Ghattas, O., 2001, “Nearly Orthogonal Two-Dimensional Grid Generation with Aspect Ratio Control,” J. Comput. Phys., 171(2), pp. 805–821.

[124] Eç, L., 1996, “2D Orthogonal Grid Generation with Boundary Point Distribution Control,” J. Comput. Phys., 125, pp. 440–453.

[125] Lee, M., Park, G., Park, C., and Kim, C., 2020, “Improvement of Grid Independence Test for Computational Fluid Dynamics Model of Building Based on Grid Resolution,” Adv. Civ. Eng., 2020.

[126] Koo, H. M., Cheong, K. B., and Song, T. H., 1997, “Schemes and Applications of First and Second-Order Discrete Ordinates Interpolation Methods to Irregular Two-Dimensional Geometries,” J. Heat Transfer, 119(4), pp. 730–737.

Vitae

Name	Md Ershadul Haque
Nationality	Bangladeshi
Date of Birth	February 15, 1991
Email	ershadulhaque09@gmail.com
Address	Holding Number: 238, Jamaljong Etakhola Road, Dashra Dhoyapukur, Khetlal-5920, Joypurhat Division: Rajshahi Country: Bangladesh
Academic Background	Mater of Science in Mechanical Engineering Department of Mechanical Engineering. King Fahd University of Petroleum and Minerals (KFUPM), Dhahran-31261, Saudi Arabia. Graduation date: December 2021
	Bachelor of Science in Mechanical Engineering Department of Mechanical Engineering, Rajshahi University of Engineering and Technology (RUET), Rajshahi-6400, Bangladesh Graduation date: December 2014

Publications

[1] M. E. Haque, S. B. Mansoor, “Solving the Radiative Transfer Equation in Complex Geometries of Orthogonal Curvilinear Coordinate System Using Body-Fitted Coordinate”. (Ready for submission)

[2] M. E. Haque, S. B. Mansoor, B. S. Yilbas, R. Ben-Mansour, “Effect of Geometry Skewness on Radiative Transfer in a Participating Media”. (Ready for submission)